Suspension Plasma Sprayed Alumina-Yttria Stabilized Zirconia Nano-Composite Thermal Barrier Coatings – *Formation and Roles of the Amorphous Phase*

Fariba Tarasi

A Thesis

in

The Department

of

Mechanical and Industrial Engineering

Presented in Partial Fulfilment of the Requirements

For the Degree of Doctor of Philosophy at

Concordia University

Montreal, Quebec, Canada

February 2010

Abstract

Suspension Plasma Sprayed Alumina-Yttria Stabilized Zirconia Nano-Composite Thermal Barrier Coatings-*Formation and Roles of the Amorphous Phase*

Fariba Tarasi, Ph.D.
Concordia University, 2010

Thermal barrier coatings have been used for the last half century to protect parts in high-temperature service from premature damage. Thermal barrier coatings are mostly produced by thermal spray techniques, especially plasma spray processes. They are widely used in the aerospace and automotive industries and in power plants, applications in which there is an ever-increasing demand for further improvement of functionality and durability. In the field of material design, use of composite coatings rather than monolithic material, and nano-structure instead of conventional grain sizes, are among the solutions most often considered. Suspension plasma spray is an innovative process for production of nano-structured thermal barrier coatings.

This research project was directed toward a superior thermal barrier coating using suspension plasma spray deposition of the alumina-yttria stabilized zirconia composite material with nano-crystalline structure. Crystallization of the amorphous phase is introduced as a new route toward nano-crystallinity in ceramics, as was previously applied in the metals and alloys. The suspension plasma spray process was used in production of coatings with comparatively high amorphous content. The work

concentrates on three major aspects of thermal barrier coating improvement. The primary focus of the project is amorphous phase formation and the roles it plays in properties and structure. This phase, which was found beneficial to nano-crystallinity, improves the mechanical properties after heat treatment. The second concentration is the suspension plasma spray process and the versatility of its resulting microstructures, and a comparison of suspension with the conventional plasma spray process. The third aspect is the properties of alumina-YSZ composite material as a choice for thermal barrier coating application. It was found that the material can compete with the present YSZ material in some aspects (e.g. thermal resistivity and hardness), but suffers from some other deficiencies (e.g. brittleness and high erosion rate). This suggests considering some other compositions of the composite, while continuing in microstructural improvement of this material for thermal barrier application.

To my devoted mother and the eternal soul of my father

Acknowledgements

I would like to gratefully thank my supervisors Dr. Mamoun Medraj and Dr. Ali Dolatabadi for their careful supervision and kind and considerate support within the course of this research, Dr. Jorg Oberste-Berghaus for his crucial guidelines and Dr. Christian Moreau for his generous scientific and financial support. I extend my sincere thanks to all the researchers and technicians in the advanced material group of IMI-NRC Canada, every single one of whom has played a role in the advancement of this research project, in addition to Dr. Dmytro Kevorkov for his useful consultation in XRD techniques.

I also appreciate the kind help of the Liburdi Company, especially, Dr.s Doug. Nagy and Tiberius Rusan for free testing of the thermal cyclic samples.

Table of Contents

ABSTRACT ..... **III**

ACKNOWLEDGEMENTS ..... **VI**

TABLE OF CONTENTS ..... **VII**

LIST OF FIGURES ..... **X**

LIST OF TABLES ..... **XVI**

CHAPTER 1 INTRODUCTION AND LITERATURE REVIEW **1**

1.1. TBC Coating Processes **5**
1.1.1. Processes for Nano-Feed Application 6
1.1.2. Suspension Plasma Spray 8

1.2. Particle Interaction with Plasma Jet **11**

1.3. TBC System and Materials **12**

1.4. Failure Mechanisms of TBCs **17**

1.5. Graded and Composite Coatings of Zirconia-Alumina **19**
1.5.1. As Sprayed YSZ, Alumina and Alumina-Zirconia Composite Coatings 23
1.5.2. Amorphous Phase in Alumina-Zirconia Composite Coating 24
1.5.3. Thermal Changes of Alumina-Zirconia Composite Coatings 25

1.6. Objectives **27**

CHAPTER 2 EXPERIMENTAL PROCEDURES **30**

2.1. Spray Systems **30**
2.1.1. Suspension Plasma Spray 30
2.1.2. Atmospheric Plasma Spray 32

2.2. Measurement and Monitoring Systems **33**
2.2.1. Particle Size Measurement 33
2.2.2. Accura-Spray Diagnostic System 33
2.2.3. DPV2000 Particle Diagnostic System 34

2.3. Mechanical Tests **36**
2.3.1. Microhardness 36
2.3.2. Fracture Toughness 36

2.3.3. Erosion Resistance 37

2.4. High Temperature Performance 37
2.4.1. Thermal Conductivity 37
2.4.2. Thermal Cyclic Test 38

2.5. Measurement Techniques 39
2.5.1. Microstructure and Porosity 39
2.5.2. Amorphous Phase Measurement 40
2.5.3. Grain Size Measurement 43
2.5.4. Phase Analysis 44
2.5.5. Lattice Parameter Measurement 45

CHAPTER 3 CRYSTALLINE STRUCTURE AND AMORPHOUS PHASE FORMATION IN ATMOSPHERIC PLASMA SPRAY PROCESS 46

3.1. In-Flight Particle Study 48

3.2. Coating Structure and Amorphous Formation 56

3.3. Phase Analysis and Amorphous Phase Contents 60

3.4. Summary 62

CHAPTER 4 SUSPENSION PLASMA SPRAY COATING MICROSTRUCTURE AND CRYSTALLINE/NON-CRYSTALLINE STRUCTURES AND TRANSFORMATIONS 65

4.1. Controlling the Microstructure of SPS Coatings and Resulting Properties 65
4.1.1. Roles of the Parameters on Microstructure 68
4.1.2. The Effect of Porosity on Coating Hardness 77
4.1.3. The Effect of Porosity on Thermal Diffusivity 78

4.2. Phase Formation and Transformations in SPS Coatings 80
4.2.1. Crystalline/Amorphous Phases in As-Coated Structure 82
4.2.2. Phase Transformation during Thermal Analysis 92
4.2.3. Transformation Verification by Heat Treatment 93
4.2.4. Preferred Phase during Crystallization of the Amorphous Phase 96

4.3. Summary 100

CHAPTER 5 DEVELOPING AMORPHOUS PHASE IN THE COATINGS ... 102

5.1. Role of Parameters on Amorphous phase Formation 105

5.2. Coatings Amorphous Contents and Crystallite Sizes 116

5.3. Sources of Amorphous and Crystalline Phases in SPS Coatings 119
5.3.1. In-Flight Collected Powders 121
5.3.2. Comparison of the Collected Powders in SPS and APS 125
5.3.3. SPS Coatings Using Different Powders 128
5.3.4. Sources of Crystalline Phases and the Nature of Amorphous Phase 131

5.4. Summary 138

CHAPTER 6 THERMAL EVOLUTION AND HIGH-TEMPERATURE PERFORMANCE OF THE MIXED AMORPHOUS/CRYSTALLINE STRUCTURE 139

6.1. Crystallization and Phase Transformation Temperatures versus Amorphous Content 139

6.2. Crystalline Structure Changes after Heat Treatments 140

6.3. Microstructural Changes after Heat Treatments 143

6.4. Grain Sizes after Heat Treatment 145

6.5. Mechanical Properties before and after 1000°C/10 hrs Heat Treatment 149
6.5.1. Hardness 149
6.5.2. Fracture Toughness 150
6.5.3. Erosion 152

6.6. Mechanical Properties before and after 1300°C/24 hrs, 1500°C/5 hrs Heat Treatment 154
6.6.1. Hardness 154
6.6.2. Fracture Toughness 155

6.7. Thermal Conductivity Changes before and after Heat Treatment 156

6.8. Thermal Cyclic Test 158
6.8.1. Thermal Cyclic Life 158
6.8.2. Structural Changes 160
6.8.3. Microstructural Changes 162

6.9. Summary 163

CHAPTER 7 CONCLUSION, MAIN CONTRIBUTIONS AND FUTURE WORKS 165

7.1. Conclusions 165

7.2. Major Contributions 168

7.3. Recommendations for Future Works 169

Appendix 188

List of Figures

Figure 1-1 Typical microstructures of zirconia coated with a) APS [28]; b) EB-PVD over bond coat [29] 6

Figure 1-2 Radial injection of the liquid carrier into the plasma jet showing the jet fluctuations effect on the feed penetration into the plasma core [43] 9

Figure 1-3 Schematic of a typical TBC system 13

Figure 1-4 The general phase diagram for solution stabilizer metal oxides in zirconia [55] 16

Figure 1-5 Binary equilibrium phase diagram of alumina–zirconia system [ACerS-NIST Phase Equilibria Diagram, CD-ROM Database, Version 3.0] [82] 22

Figure 2-1 Mettech axial III plasma torch; (a) front and (b) rear view of the combined injection nozzle and the three plasma torches in axial III system 31

Figure 2-2 Simplified Suspension Plasma Spray (SPS) system with axial injection 32

Figure 2-3 The operating basis of the particle velocity and temperature measurement [88] 34

Figure 2-4 Physical basis for the Accura-Spray ensemble diagnostic system [88] 35

Figure 2-5 Linear regression of the data from XRD and DSC evaluation methods of amorphous content 43

Figure 3-1 Feed powders, a) Tosoh powder at 1kX and b) Tosoh powder at 50kX and back scattered mode; c) Amperite 750 at 1kX and d) Amperite 750 powder at 500X and back scattered mode 48

Figure 3-2 Variation of Amperite 750 particle temperature with the distance from the nozzle exit 49

Figure 3-3 Collected in-flight particles into water after spraying under similar plasma spray conditions, a) Tosoh and b) Amperite 750 50

Figure 3-4 Tosoh collected powder: a) unmolten particle; b) fully molten-resolidified particle and partly molten particle consisting of c) unmolten region indicated by U, molten region M, and enlarged pores designated by P. 51

Figure 3-5 Collected in-flight particles sprayed by conventional plasma spray: a) unmixed; b) partly mixed and fully mixed particles; c) high resolution microscopy of the fully mixed particle at 50kX showing no sign of crystalline grain throughout the particle 52

Figure 3-6 Fully molten and mixed particle with homogenous composition and no sign of crystalline grains 53

Figure 3-7 Structural features in an in-flight particle sprayed, solidified and collected into water: a) a typical particle; b) magnified external part and c) magnified internal part of the particle; and d) interface area of the two phases 55

Figure 3-8 Coating microstructures: a) using Amperite 750, 6/40 alumina/zirconia; and b) Tosoh 60/40 alumina/3YSZ powder 57

Figure 3-9 Intersplat conditions: a) zirconia splat deposited on solidified alumina splat and b) alumina splat on solidified zirconia 59

Figure 3-10 XRD patterns of the coatings: a) YSZ coating with tetragonal structure (TZ), b) Amperite 750 powder coating consisting of tetragonal zirconia (TZ) and alpha alumina (AA), c) Tosoh powder coating showing (TZ) and monoclinic zirconia (MZ) plus alpha (AA) and gamma alumina (GA) 62

Figure 4-1 The averaged effects of the seven variables on particle characteristics and microstructural parameters in suspension plasma spray (SPS) process 69

Figure 4-2 The effect of auxiliary gas, powder size, torch condition and plasma power on particle velocity and temperature 71

Figure 4-3 60/40 wt% alumina/zirconia suspension plasma sprayed coatings: a) resulting coating using hydrogen auxiliary gas; b) resulting coating using helium auxiliary gas at 100X; c) and d) same coatings as a and b, respectively, at 2kX 72

Figure 4-4 Plasma power effect on a) particle velocity and b) particle temperature 74

Figure 4-5 The variation of a) coating porosity vs. particle velocity and b) coating hardness vs. coating porosity 78

Figure 4-6 Thermal diffusivity versus porosity of the coatings 79

Figure 4-7 Typical XRD patterns from SPS deposition of 60 Al_2O_3/40YSZ under various spray conditions showing cubic zirconia (CZ) in a) 8YSZ and all other crystal structures, and b) sample with α-alumina (AA) as the major alumina phase or c) γ-alumina (GA) as the major alumina phase; d) mixture of both GA and AA alumina in addition to cubic zirconia. 83

Figure 4-8 Peak splitting as an indication of tetragonal zirconia phase formation and the planes of each peak 85

Figure 4-9 Alumina component phase formation behaviour within the as-deposited composite versus in-flight particle state 86

Figure 4-10 SEM micrographs of the coatings deposited using a) H_2 gas with high particle velocities and b) Helium auxiliary gas with lower particle velocities resulting in different splat flattening and intersplat contact area (circles show some of the in-flight solidified particles within the coating) 87

Figure 4-11 Entrapped unmolten nano-particles inside the large in-flight solidified particle in the coating 88

Figure 4-12 Correlation between the γ percentage in alumina and the cubic phase percentage in zirconia 90

Figure 4-13 The γ-alumina phase content versus particle velocity in the samples with mixed structure showing the role of particle temperature and feed size range 91

Figure 4-14 Heating and cooling DSC curves of a typical SPS coating showing three different peaks probable in heating process of 60 Al_2O_3/40YSZ SPS coating 92

Figure 4-15 The effect of heat treatment on a) as-sprayed alumina-YSZ coating, b) heat-treated coating at 1000°C/1 hr, c) heat-treated at 1200°C/24 hrs 95

Figure 4-16 γ- to α-alumina transformation peak area vs. crystallization peak area in the coatings with the major crystalline alumina phase of γ, α or mixed structure 97

Figure 5-1 SEM micrographs of aggregates in the dried suspensions of a) micron-powders and b) nano-powders 106

Figure 5-2 Collected in-flight particles sprayed into water: a) micron-powder presenting fully molten round particles and b) nano-powder that contains also semi-molten and resolidified (SR), as well as unmolten (U) particles 107

Figure 5-3 Microstructures resulting from a) micron- and b) nano-powder deposition showing more distinctive color and thicker lamella in nano-particle coating compared with the coating of micron particles with the same spray conditions 108

Figure 5-4 XRD pattern for the two coating samples resulting from different in-flight particle temperatures, showing smaller amorphous hump and higher crystallinity at higher T_p 111

Figure 5-5 Substrate preheat effect on the grain size of as-deposited coating 113

Figure 5-6 Loose interface contact between the coating and substrate, causing lower cooling rate of the upcoming splats 115

Figure 5-7 Grain size of different phases versus amorphous phase (according to the crystallization peak size) in each coating sample deposited under various conditions with SPS process 117

Figure 5-8 Crystallization peak area vs. in-flight particle showing formation of smaller amount of amorphous phase at higher velocities (The in-flight particle temperatures in ºC are shown on the data points)..... 118

Figure 5-9 In-flight particles collected in water after spraying with SPS process at 3000X from a) powder #1 (large agglomerated nano-particulates) using system 1; b) powder #2 (loose nano-particles) sprayed using system 1; c) micron-particles by system 1; d) the same as b, sprayed using system 2; e) the same as c, sprayed using system 2; f) powder #1 sprayed with APS at 1000X 123

Figure 5-10 SPS-sprayed powder #2 (loose nano-powders mixture) showing different stages of melting and mixing in the plasma jet: a) partly melted with crystalline particles retained; b) largely melted with extended mixing (grey color) 125

Figure 5-11 SPS-sprayed nano-particles collected in water: a) fully dendritic growth in unmixed particles; b) dendritic growth in partly mixed particle (arrowed); c) non-crystalline particle 127

Figure 5-12 Unmolten particles collected in-flight from SPS process: a) partial segregation of components started; b) no segregation accomplished 128

Figure 5-13 SPS coatings from: a) powder #1 sprayed with system 1; b) powder #2 sprayed with system 1; c) powder #3 sprayed with system 1; d) same as b, sprayed with system 2; e) same as c, sprayed with system 2; f) 8 wt% YSZ nano-powder coated with system 2 129

Figure 5-14 XRD pattern of as-coated powders: a) typical pattern of the structures sprayed with system 1; b) coating of powder #3 deposited with system 2; c) coating of nano-powder of 8 wt% YSZ, where z represents the cubic (or t’ zirconia), m-z is monoclinic zirconia, G-A shows γ alumina peaks and A-A is α-alumina. 132

Figure 5-15 XRD pattern of the coating of nano-powder 60 alumina-40 (8 wt% YSZ) deposited without atomization showing the location of amorphous hump maximums .. 133

Figure 5-16 Lattice parameters of the crystalline portion of the coatings: a) parameter *a* for cubic zirconia; b) parameter *a* for α-alumina; c) parameter *c* for α-alumina 135

Figure 6-1 Transformation temperatures versus crystallization peak area, showing that neither crystallization temperature nor the γ- to α-alumina transformation temperatures are affected by the amorphous content 140

Figure 6-2 Comparison of crystalline structure of heat-treated coatings with fully crystalline and highly amorphous coating: a) coating with 64% amorphous; b) 64% amorphous coating heat-treated at 1300°C for 24 hrs; c) highly crystalline (11% amorphous) coating not heat-treated; d) same as c after heat treatment at 1300°C for 24 hrs..... 142

Figure 6-3 Microstructure of: a) as-deposited high amorphous coating; b) as-deposited low amorphous coating; c) high amorphous coating heat-treated at 1300°C/24 hrs; d) low amorphous coating heat-treated at 1300°C/24 hrs; e) high amorphous coating after 1500°C/5 hrs; f) low amorphous coating after 1500°C/5 hrs 144

Figure 6-4 The role of amorphous content on grain size changes during crystallization heat treatment for a) α-alumina, b) γ-alumina, and c) zirconia..... 147

Figure 6-5 Hardness measures before and after crystallization heat treatment for different amorphous coatings 149

Figure 6-6 Fracture toughness in coatings with different amorphous content, before and after heat treatment at 1000°C/12 hrs 151

Figure 6-7 Brittle fracture of 55% amorphous coating under indentation..... 151

Figure 6-8 Erosion losses in two different amorphous coatings before and after heat treatment at 1000°C/12 hrs and comparison with YSZ coating with the same process . 152

Figure 6-9 Fracture surface of alumina-YSZ coating deposited by SPS process: a) before; and b) after heat treatment at 1000°C for 10 hours showing annihilation of columns and sintering of the structure 153

Figure 6-10 Comparison of the hardness variation with heat treatment between two samples with low and high amorphous content and their comparison with the 8 wt% YSZ 154

Figure 6-11 The role of amorphous content on fracture toughness before and after heat treatments at 1300°C/24 hrs and 1500°C/5 hrs..... 155

Figure 6-12 Thermal conductivity changes before and after heat treatment at 1000°C/10 hrs for coatings with various amorphous contents..... 158

Figure 6-13 Thermal cyclic test samples after 500 cycles; left sample with 36% amorphous content, middle sample with 52% amorphous and right sample conventional YSZ coating 159

Figure 6-14 Oxide layer in top/bond coat interface of a) the porous composite coating after 20 cycles 160

Figure 6-15 XRD pattern of high amorphous sample (48%): a) before and b) after 500 thermal cycles between room temperature and 1080°C, where C-Z denotes Cubic Zirconia; t-Z, tetragonal zirconia; AA, α-alumina; GA, γ-alumina and DA, δ-alumina 161

Figure 6-16 High amorphous (52 %) coating of alumina-YSZ composite a) as-deposited and b) after 500 thermal cycles up to 1080°C..... 162

Figure A-1 Crystallinity index as a function of either spray condition or composition in alumina-zirconia composite coating 193

List of Tables

Table 3-1 Spray condition for the two types of powders and the resulting particle condition and coating thicknesses 47

Table 4-1 Variables and levels in Taguchi design of experiment 66

Table 4-2 Variables evaluated for the effect on phase formation 81

Table 5-1 Spray conditions for producing the comparison samples and the resulting amorphous measurement results 104

Table 5-2 The importance of each parameter on the amorphous phase formation within the alumina-YSZ composite coating using SPS 105

Table 5-3 Powder feed details 120

Table 5-4 Spray condition and the resulting amorphous contents 122

Table 6-1 Role of amorphous content on grain growth during heat treatment 148

Table A-1 SPS spray conditions for the two compositions of alumina-YSZ composite 192

List of Abbreviations

AHZ Alumina-hardened zirconia

APS Atmospheric plasma spray

CMAS Calcium-magnesium-aluminum-silicon compound

DSC Differential scanning calorimeter

EB-PVD Electron beam-physical vapor deposition

SEM Scanning electron microscope

SPPS Solution precursor plasma spray

SPS Suspension plasma spray

TBC Thermal barrier coating

TGO Thermally grown oxide

XRD X-ray diffraction

YSZ Yttria stabilized zirconia

ZTA Zirconia-toughened alumina

Chapter 1 Introduction and Literature Review

Thermal spray processes for coating deposition include the practice of heating and propelling the molten or heat-softened material toward the substrate at high velocity. The process results in flattening of the individual splats and their adhesion to the substrate, and produces the coating [1]. Plasma spray processes are among the most widely used thermal spray processes in industry. The plasma gun consists of a copper anode and a tungsten cathode. The electrical potential between the anode and cathode results in severe ionization of the flowing plasma gas between the two electrodes. This forms a plasma flame with temperatures of up to 30,000 K, in which the particles of various materials with any melting point can be melted and accelerated toward the substrate. Such a process thus suits the deposition of ceramics with a rather high melting point used in high-temperature applications. Thermal barrier coatings like zirconia, which has a melting point of about 2700°C, are mostly sprayed with this process.

Thermal barrier coatings (TBCs) have been a key in solving the problem of thermal stability in high-temperature parts of engines, following three decades of efforts in improvement of super alloys as the construction material [2]. Thermal stability is especially critical for parts at high-temperature service with cyclic heat under abrasion, erosion and, to some extent, corrosive environments, in addition to harmful deposits from combustion processes. Combustion temperatures in car engines and aerospace gas

turbines are limited by the inability of common metallic structural materials to withstand the high temperatures. The lifetime of blades and vanes, as well as turbine shrouds and combustor cans, is crucial in performance of the gas turbine engine [3]. These parts have to be preserved at temperatures roughly above 1000 ºC for as long as possible [4].

Zirconia has been found to be the material most matched with the required characteristics of a good TBC that include, but are not limited to, high melting point, high thermal, wear and oxidation resistance, as well as high hardness and fracture toughness and relatively low density [3]. However, there is a harmful martensitic phase transformation in this ceramic from tetragonal to monoclinic structure involving about 4% volume expansion that causes cracking and deterioration of the coating [5,6]. Thus, stabilizing additives have been used to prevent this unfavourable transformation, normally by formation of solid solutions [7]. Yttria stabilized zirconia (YSZ) is the most well known solid solution used as a TBC. Details of the solution forming and other methods of stabilization will be further explained in this text.

Although application of solution formers is an effective way to achieve stabilization, they do have some drawbacks. There are two major concerns in this kind of stabilized zirconia coating. First, the required low thermal conductivity can be achieved only at high porosity content [8], which in turn adversely affects the mechanical properties such as hardness [9], erosion [10] or elastic modulus [11]. The second concern is oxygen diffusion. The elements in solution-forming materials (e.g., yttrium in Y_2O_3) normally have lower capacity for oxygen bonding than zirconium, and substitution of these atoms in the zirconium oxide cells leaves some oxygen vacancy within the unit cell. This oxygen vacancy tends to enhance the oxygen transparency of the top coat toward the

substrate where oxidation of the bond coat in the interface with substrate can happen [12]. This deficiency in yttria-doped zirconia is found to be more severe when the coating is nano-structured [12], for the reason of enhanced grain boundaries that in this material are the favoured paths for oxygen diffusion. The oxygen transparency is partly solved by using the protective bond coat to preserve the substrate from severe oxidation. Nevertheless, the bond coat itself has many challenges in dealing with diffused oxygen [13,14] and can result in coating failure due to extensive oxidation of bond coat as will be explained in section 1.4. Another difficulty facing zirconia as a monolithic top coat is the elimination of the microstructural defects due to sintering by increasing the service temperature or heat treatment at high temperature. These processes lead to enhanced thermal conductivity [15] as well as facilitating catastrophic crack propagation in the coating [16].

Zirconia in TBC application is an example of durability over performance, meaning that this material was selected in spite of the existence of other materials with lower thermal conductivity [17]. However these materials are not able to withstand thermal cycling, or do not have the high temperature stability as zirconia. Therefore, although the application of materials such as multiple dopants (solution formers) has succeeded in lowering thermal conductivity [2,18], the effort to find proper substitutes is continuously in progress and the present work is in line with this goal.

Graded and composite structures for TBC are among the most used means of meeting the various needs of a successful TBC system. An important composite under investigation for replacing the present YSZ TBC is its combination with alumina. Alumina is chosen

for a number of reasons that will be detailed later in this thesis. Alumina-YSZ is the material of interest in this research (section1.5).

On the other hand, the benefits of the nano-crystalline structure of materials are now well confirmed [19,20]. Plasma spray processes are among the production practices during which nano-crystallinity is attainable by extremely high cooling rates of the molten particles that impact the substrate at high velocities and flatten into thin lamella. Application of nanometric feed materials is expected to be one of the ways to extend nano-crystallinity. Nevertheless, the agglomeration of nanometric feed particulates into large particles introduces difficulties in the injection process.

In the plasma spray process, the particles can be injected into the plasma jet in the form of either dry powder, or wet condition dissolved or suspended in a liquid carrier. Suspension plasma spray (SPS) is one of the most recent and innovative plasma spray processes designed to circumvent the application complexity of nano-size dry feed stocks. Briefly, it includes application of a carrier suspension liquid for injection of the solid powders into the plasma jet to produce a nano-structured coating.

Amorphous phase formation is an interesting aspect in thermal spray deposition of composite materials, and often accompanies nano-crystallinity. It involves several components that retard each others' crystallization during rapid solidification and results in the creation of non-crystalline structures. Consequently, in plasma spray deposition of the material of concern in this study, i.e., pseudo-eutectic alumina-YSZ composite, considerable amorphous phase formation is highly probable. Many reports support the observation of amorphous phase in alumina-YSZ composite deposition [21-24]. It is now

well known that the deep eutectic composition of eutectic systems, including the present system, is more likely to form amorphous phases than other compositions.

This study was organized mainly to investigate amorphous phase formation and its roles in phase transformations and nano-crystallinity of pseudo-eutectic alumina-YSZ composite coating deposited by plasma spray process, particularly suspension plasma spray process. Furthermore, since the material is thought of as a potential TBC, some of the prominent TBC properties have been investigated and compared with YSZ (the present TBC material), while trying to understand the role of amorphous phase.

1.1. TBC Coating Processes

There are a great number of methods for coating production. Thermal spray includes a versatile group of these processes. Montavon in his taxonomy [25] introduces about twenty different thermal spray methods and techniques. However, for industrial production of TBCs, the processes most often used are physical vapour deposition (mainly using electron beam for evaporation of the material concerned) known as EB-PVD, and thermal spray processes consisting of high velocity oxy-fuel (HVOF) spray and atmospheric plasma spray (APS). Of these, the APS and EB-PVD processes are the most competitive. Typical microstructures of these coatings are shown in Figure 1-1(a) and (b), respectively.

The APS coatings are more thermal resistant than EB-PVD [17], while the unique comb-like microstructure of EB-PVD coatings, as shown in Figure 1-1(b), gives them a better strain tolerance and consequently a longer thermal cyclic life [26]. These coatings, however, are more expensive than APS [27]. APS processes have attracted more attention

and versatile use in the aerospace, automotive and power generation industries, mainly because of their lower cost, ease of application without the need for a vacuum or gas environment (unlike PVD processes) and ability to be applied to large areas in a comparatively short time.

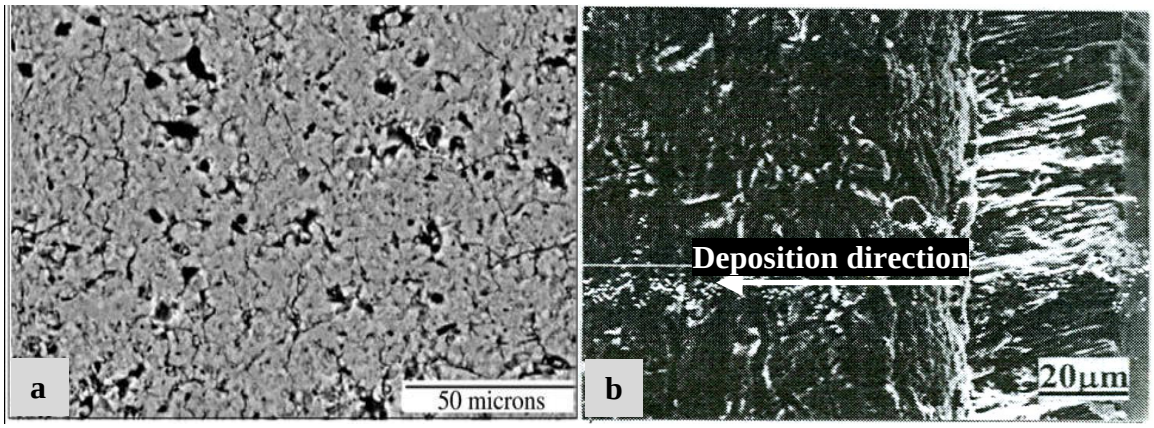

Figure 1-1 Typical microstructures of zirconia coated with a) APS [28]; b) EB-PVD over bond coat [29]

1.1.1. Processes for Nano-Feed Application

The superior mechanical properties of nano-structured coatings [20] have led to the development of many processes to produce such coatings. Some of these processes were summarized by Fazileau et al. [30]; including thermal plasma chemical vapour deposition (TP-CVD), HVOF, thermal plasma spray pyrolysis (TP-SP), thermal plasma flush evaporation (TPFE) and hypersonic plasma particle deposition (HPPD). Most of these processes are recognized as being either economically unfavourable or difficult to apply.

In contrast, since the 1980s, plasma spraying has been recognized as one of the most economic, easy to use and highly efficient processes in the industry. The most recent innovations based on plasma spray technology promote the direct application of the nanometric feed particles in production of nano-structure. These technologies involve the

application of a liquid carrier for transporting the nano – or a few micron – size feed into the plasma jet. Due to technical difficulties in the transport process of such fine powders, especially issues with aggregation and clogging, presently the only way to apply powder feeds of this size range (i.e., <5 μm) is the use of a carrier liquid instead of gas. In response, two technologies have recently been developed: the solution precursor plasma spray (SPPS) and suspension plasma spray (SPS) processes. Although it is possible to apply nano-sized powder accumulated in large agglomerated or spray-dried masses of nano-particulates by conventional APS [31-33], the liquid-carrier-based techniques are preferred for producing denser microstructures [34]. Furthermore, these techniques using extra-small particles can yield thinner lamella with almost no inter-lamellar cracks and lower residual stresses compared with the large-sized lamella produced in gas carrier techniques [25]. The liquid carrier processes have been superior to APS process also in the application of materials prone to decomposition, such as $LaMnO_3$ Perovskite, where the thermal load imposed on the plasma due to liquid evaporation reduces the plasma temperature and prevents overheating of the material [35].

In the SPPS technique [36-39], the liquids are salt solutions of the material; in the case of yttria stabilized zirconia these are zirconium and yttrium salts. In this process, the liquid precursors have normally been injected radially into the plasma flame. The precursor droplets, after atomization during injection or in the plasma jet, undergo acceleration, break-up and rapid liquid evaporation, followed by precipitation, gelation and pyrolysis in the plasma flame [38]. The accelerated particles in the plasma flow impact the substrate and incorporate into the coating.

The liquid carrier processes of SPS and SPPS are quite similar, with the main difference appearing in the decomposition of the liquid; in SPS the liquid composition is fixed until evaporation takes place. Many common features exist in the two processes, including the formation of very dense microstructures as well as the explosion phenomena. The particle explosion happens during deposition of porous powders due to entrapped liquid in the core of the melted particle. It has manifested as shell-like splats in SPPS [20], while the SPS process is reported to end with smaller particle sizes than expected [40]. SPS, as the major process used in this study, is discussed in more detail in the following section.

1.1.2. Suspension Plasma Spray

As mentioned earlier, SPS consists of the injection of a liquid carrier containing the suspended solid powders into the plasma jet. Therefore, particles must be properly dispersed to provide a stable suspension without excessive agglomeration or settlement, or both. This is achieved with the help of appropriate dispersant and using milling processes before and mixing during the injection process to prevent overly enlarged agglomerates and to break them up if formed.

The feed injection may be external by radial injection from a nozzle as shown in Figure 1-2. This method has been used in most of the work on SPS [30,40-42]. Figure 1-2 shows that liquid droplet penetration and fragmentation are strongly linked to the arc fluctuations [43]. In the external injection method, in addition, the angle and the distance of the feed injection nozzle to the torch are crucial parameters and the resulting coating is sensitive to the injection condition. Besides, the particle injection velocity needs to be high enough to allow penetration into the plasma core. This velocity has to be provided

by high injection gas pressure that can disturb the plasma jet; this factor is of major importance [44].

Figure 1-2 Radial injection of the liquid carrier into the plasma jet showing the jet fluctuations effect on the feed penetration into the plasma core [43]

The second injection method consists of axial injection, which is not applicable to the ordinary plasma spray torches. Axial injection can be used with specific designs of torches such as hollow cathode radio frequency plasma in which the hollow core of the torch allows the passage of the liquid injection tube [45]. One of the recent technologies (used in the Industrial Material Institute of the National Research Council of Canada in Boucherville, Quebec) uses a Mettech axial III torch plasma system in which three torches converge at a focal point where the liquid feed is axially emerging at high pressure. This system will be discussed in more detail in Chapter 2, because it is the one used in this study.

The spray distance in SPS process has to be rather short, since the feed particle sizes in SPS are much smaller than those used in APS and can lose their absorbed heat and momentum more rapidly [45]. The optimum spray distance (from the spray nozzle exit to the substrate) was found to be between 40-60 mm for efficient interaction between the

particle and plasma where melting is completed and in-flight solidification does not happen [40]. The interaction between the particle and the plasma flame is also affected by the droplet size that is injected into the plasma flow. Thus the atomization of liquid droplets can be important for the resulting coatings and spray outcomes.

There are two atomization methods during liquid injection into plasma flame. The first is air- (or gas-) assisted atomization that, according to Jordan et al. [46], using an argon flow in the atomizing probe can produce droplets of 20 to 45 μm. This kind of atomization mixes the air or gas with the liquid before the injection nozzle exit and the gas expansion upon emerging from the nozzle results in fragmentation of the liquid droplets into smaller ones. This method tends to require a high gas pressure and introduces some difficulties when used with conventional plasma spray, since the method involves external injection and such high gas pressure can end up with strong perturbation of the plasma jet. Gas-assisted atomization seems more appropriate when the gun design allows the use of axial injection, as does the gun used in this study, Mettech axial III. In this gun, based on the orientation of the three plasma torches that leave a hollow core in the center, axial injection is possible. The geometry of the Mettech axial III gun will be discussed further in Chapter 2.

The second atomization method is direct liquid injection, which is more appropriate for conventional plasma process to avoid disruption of the flame. This injection employs a high back pressure to the liquid container to expel the liquid from the exit point with small droplet size. Using this method, Wittmann et al. [47] could force the water droplets with pressures below 0.8 MPa to form in dimensions of about 200 μm at a distance of 15 mm from the injection nozzle exit. They found a droplet velocity of 15 to 25 m/s

adequate for penetration into the plasma core. In continuation of the same study, using ethanol suspension the droplets were found to be further fragmented (i.e., secondary atomization) into dimensions of a few micrometers because of the effect of the plasma jet. Secondary atomization by plasma jet was also reported by Fauchais et al.[48], where droplets of YSZ suspension with dimensions of a few hundred micrometers were fragmented into droplets 0.5 to 5 μm in diameter. In this work both methods, i.e., direct injection and gas-assisted atomization, were applied and the result of the particle interaction with the plasma jet was scrutinized using the collected sprayed powders and coatings.

1.2. Particle Interaction with Plasma Jet

The interaction between the in-flight particle and the plasma jet has a direct effect on the quality of the resulting coatings. Since the characteristic heat and momentum transfer to the particles are directly linked to the mass of the particles, Fauchais et al. [48] addressed the importance of the particle size on its complete melting. According to them, the small submicron particles are more sensitive than large particles to the plasma arc fluctuations. This causes their irregular treatment (variation in heating and acceleration), and drastically affects the coating quality in this process where small particles are involved.

Delbos et al. [49] also reported that uneven size distribution is an important reason for non-uniform treatment of the particles [49]. Particles in the powders have a wide size range, and accordingly receive different thermal treatment by the plasma. This situation is intensified when dealing with materials of low thermal conductivity such as zirconia or alumina ceramics [50]. Material with low thermal conductivity requires longer time for

complete melting throughout the particle bulk. It may seem that for small particles this should not be an issue. However, it was noticed that even when correctly injected into the plasma core, the small particles can escape from the core and travel in the cold fringes of the flame [40], thus receiving less heat for thorough melting.

In addition, plasma fluctuations are known to be a major reason for broad diversity in particle temperature and velocity. In APS, it is possible that these fluctuations vary the temperature and velocity of alumina particles by 600°C and 200 m/s and of zirconia particles by 400°C and 60 m/s, respectively [51]. Such evaluation for individual in-flight nano-particles currently is not possible by the present diagnostic systems. However, it may be expected that smaller particles and/or low density (porous particles) with low mass or mass density are more severely affected by these fluctuations. The in-flight particle velocity and temperature can also affect the composition distribution of the resulting coatings. It was suggested that longer dwelling time in the plasma flame results in increased alloying in Hydroxiapotaite (Ca_{10} $(PO_4)_6(OH)_2$) and Al-Ni-Mo alloys [52].

1.3. TBC System and Materials

A TBC system as schematically shown in Figure 1-3 consists of three main components. The first two of these are a top coat as the thermal barrier, and a bond coat that reduces the thermal expansion mismatch between the substrate and top coat and has a good adhesion to the substrate. The common materials for bond coat are MCrAlY alloy, in which M is one of the Co or Ni metals, and Pt-aluminide [17]. The bond coat, containing aluminium element, is also the source of material for environmental protective aluminium oxide. The aluminium oxide layer is the main constituent of the third component in a

TBC system [53], and is known as thermally grown oxide (TGO). TGO is preferred to be composed of α-alumina for its low oxygen transparency and superior adherence to the substrate [54].

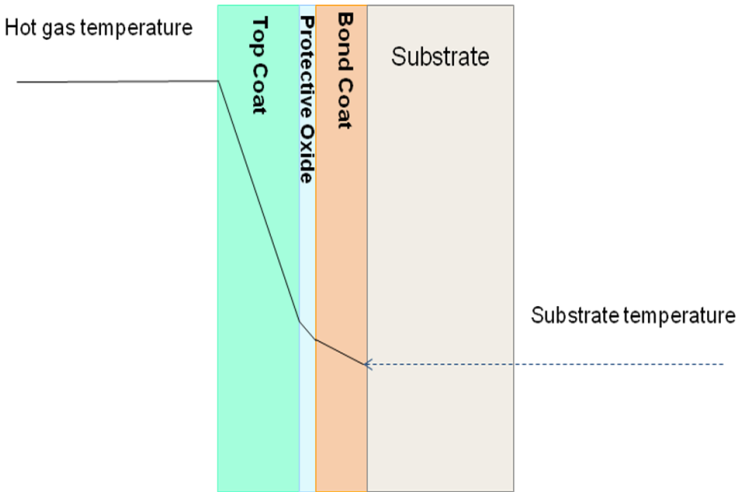

Figure 1-3 Schematic of a typical TBC system

TBC thickness for gas turbine engines is usually 250-375 μm of zirconia. For truck engines, off-road diesel engines or large marine diesel engines this thickness may be much greater, for instance 1.5-6.25 mm [3]. In general, a more porous zirconia layer favours better heat insulation and spallation resistance, whereas the less porous layers give improved erosion resistance. Thermal cyclic life can also be quite sensitive to zirconia density [3].

A thermal barrier coating should not only insulate the substrate metal from high temperature, but also, in some cases, protect the base material against hot corrosion, oxidation and wear damage. Stern et al. [3] have named the fundamental requirements for a successful thermal barrier coating as low thermal conductivity, high melting point, low density, high surface emissivity and high thermal shock resistance. In addition, according

to Stern et al., resistance to oxidation and corrosion, high coefficient of thermal expansion, and resistance to gaseous and particulate erosion are other characteristics for a favourable TBC. Further characteristics of an ideal TBC that can be added to these are being preventive to corrosives and oxygen diffusion, and resistant to the diffusion of fuel combustion and corrosion deposits.

The success of zirconia as a thermal barrier coating is due to its properties being relatively well compromised for the requirements of a TBC. These properties, measured against the requirements mentioned for a favourable TBC, have made zirconia the first choice for TBC coating. However, several other materials have been examined for this application. Ma et al. [39] listed some of them as zirconium phosphate and zirconates with a perovskite structure (such as $SrZrO_3$, $BaZrO_3$) or a fluorite structure ($La_2Zr_2O_7$, $Nd_2Zr_2O_7$), and yttria-alumina garnet based ceramics (such as $Y_3Al_5O_{12}$, $Y_3Fe_5O_{12}$, $Y_3Al_{0.7}Fe_{4.3}O_{12}$). Nonetheless, these have not been as efficient, long lasting or easy to apply as zirconia, although some of them have been used by some manufacturers [39].

As mentioned before, the effective performance of zirconia TBC is strongly affected by its phase transformation from tetragonal to monoclinic. Undoped zirconia goes through the following phase transformations by heating up to temperatures that are not in a complete consistency in different references. Monoclinic zirconia transforms to tetragonal at 1114-1180°C [55-58] and the transformation of tetragonal to cubic happens at around 2370°C, finally melting at 2710°C [58]. Tetragonal to monoclinic phase transformation of zirconia happens during a martensitic transformation with almost 4% volume expansion [3] and causes the deterioration of the coating properties by increasing the residual stresses and crack formation.

Three different forms of tetragonal zirconia (t, t', t") have been discussed by Yashima et al. [58]. These authors have resolved some ambiguities in the changes of the unit cell parameter of tetragonal zirconium oxide, which was previously considered a cubic structure. The tetragonal phases t and t' (t' is called non-transformable tetragonal zirconia) are mostly followed and reported in different works, whereas for the t" tetragonal no report was found to show different characteristics from the two other tetragonal phases. The t" phase is also categorized as cubic structure [59], and in this study this designation is followed. A great number of efforts have focused on prevention of the tetragonal to monoclinic transformation. Solutions to this problem can be categorized in the following three groups:

a) Solid solution stabilization by substituting for some of the Zr atoms the base element of oxides of alkali metal atoms like CaO, MgO or transient metals as in Y_2O_3, Sc_2O_3, Er_2O_3 [58] or rare-earths such as CeO, Yb_2O_3 and or the whole Lanthanides group [17] in the oxide cells. The stabilizing effect and thermal resistance increase with increasing the amount of solution former [7]. Figure 1-4 demonstrates the general equilibrium phase diagram for solution-former oxides in zirconia. It shows that at higher amounts of metal oxides, the high-temperature cubic structure is stabilized at ambient temperature. Zirconia stabilized with various amounts of yttria is the most applied TBC, and hence is known as YSZ.

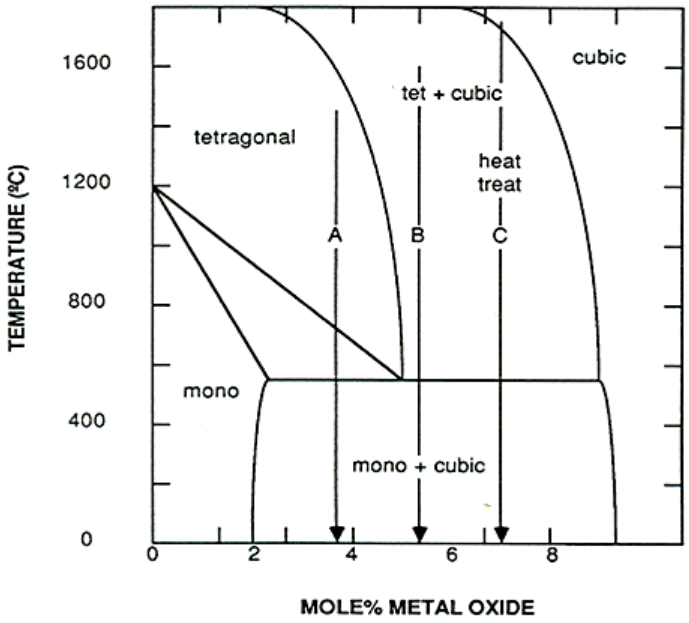

Figure 1-4 The general phase diagram for solution stabilizer metal oxides in zirconia [55]

b) Grain size controlled stabilization may be explained based on the calculations by Garvie [5] and followed by the experimental works reported in [56,60], it was revealed that the prerequisite for tetragonal to monoclinic transformation of zirconia at any specific temperature is a grain growth to a critical size; at smaller grain sizes, the transformation from tetragonal to monoclinic (t-m) is prohibited. Thus, for (t-m) phase transformation control, it is enough to control the grain size. Controlling the dimension to prohibit the (t-m) transformation was used in the graded layer of the alumina/zirconia coating system [57,61]. In this system, the layers of alumina, between the zirconia nano-layers (less than 23 nm), served as the termination surface for the zirconia crystallites and could eliminate the (t-m) transformation [60].

c) Insoluble oxide stabilization with a material like alumina (Al_2O_3) is another solution for preventing the unfavourable transformation of zirconia. Alumina can form a rigid matrix around the ZrO_2 crystals and impose a compressive stress against the expansion

involved in the martensitic transformation of tetragonal to monoclinic, thus preventing the autocatalytic reaction by volume change control [6].

In addition to stabilization for higher quality of the coatings, the study of the failure mechanisms in TBC systems helps selection of more appropriate materials for this application.

1.4. Failure Mechanisms of TBCs

TBCs are used in two major domains: a) power generation plants where there is high temperature but minimum thermal cycles; and b) aero engines where extensive thermal cycling exists [27]. In each of these applications, Evans et al. [27] have extensively discussed the mechanisms of failure. Based on their discussion, excessive TGO growth has a prominent role on the lifetime of TBCs. In addition, Schlichting et al. [62] suggest a simple failure model based on the crack formation and growth in TGO, in which thickening of the TGO layer is known as "the key progressive process responsible for failure." According to Schlichting et al. [62], thermal expansion mismatch and elastic modulus mismatch between the thick TGO and the bond or top coat results in cracking. The cracks at the bond/top coat interface with TGO at undulation crests formed due to out-of-plane tensile stresses that arise from the compressed TGO that continues thickening. Thus top coat materials with more resistance to oxygen diffusion can be beneficial to a longer lasting TBC system.

A second major source of failure of the TBCs is produced during operation. Calcia, magnesia, alumina and silica are combustion products of gas turbine engines where TBCs are applied. When present, at high temperatures these products form a compound referred

to as CMAS. They can form a eutectic of low melting temperature of about 1190°C [63] or 1240°C [64]. Upon formation at high-temperature service conditions, they are amorphous. The CMAS melt infiltrates into the vertical asperities of comb-like EB-PVD microstructure, and after solidification, forms a solid with a large thermal-expansion mismatch with the TBC. This leads to formation of large horizontal cracks in the TBC and delamination of the system during service. Higher concentrations of alumina increase the melting point and, consequently, the higher viscosity of the mixture. The result is a lower infiltration capability of the CMAS melt into the coating, which in turn means a lower depth of penetration. It should be noted that for the CMAS to end up with coating spallation, a minimum depth of penetration is required for the stresses originated from CMAS to result in crack formation and propagation [65].

Efforts in producing dense vertically cracked (DVC) structures in plasma sprayed coatings are currently in progress [64,65]. DVCs in the APS coatings are intended to produce a segmented structure, similar to the comb-like grains in EB-PVD coatings, to increase the strain tolerance of these coatings. It can be concluded that in the same way, CMAS can be a danger for vertical cracks in plasma sprayed coatings. Using alumina in the coating is expected to help overcoming this problem.

Graded layer and composite materials were previously listed among the structures that could lead to superior TBCs with better performance and longer lifetime. However, because of the importance of these coatings in this research, the discussion of these structures was reserved until after the details given above.

1.5. Graded and Composite Coatings of Zirconia-Alumina

The requirements of a TBC material, as listed earlier, are so versatile that it seems quite unlikely to find them all in one single material. Therefore, the idea of multilayer and/or composite coatings became the subject of many investigations [38,66-68]. Alumina for several reasons is widely used as the alternative layer in the graded and/or composite structures with zirconia that are mentioned below.

Graded and composite alumina with yttria-stabilized zirconia (alumina-YSZ) has shown the capability of larger temperature drop in the substrate from the coating surface and superior thermal shock resistance than YSZ [67]. Moreover, composites of alumina with zirconia possess lower residual stress [69], higher hardness, lower porosity and improved adhesion [70]. Other reasons may be summarized as follows.

Alumina acts as the stabilizer for tetragonal zirconia by two mechanisms: grain-size control in nano-structure coatings by virtue of its higher elastic modulus than zirconia; and solid solution formation [56]. By playing the stabilizer role, it allows the use of lower amounts of other stabilizers and thus may reduce their harmful effects, such as oxygen diffusion. Alumina presents higher resistance to oxygen diffusion than does zirconia [70]. Hence, it lowers the transparency of the whole coating, resulting in controlled growth of TGO and other unwanted oxides [14]. It also improves the resistance of the coating against the damaging effects of CMAS [39] according to the above details. In addition, the detrimental effects of sintering of the zirconia at high temperatures (e.g., enhanced thermal conductivity) can be eliminated by nano-laminates of alumina [61,71]. Finally,

alumina can prevent the diffusion of harmful elements like sulfur from the bond coat or substrate into the top coat [14].

Furthermore, alumina-YSZ composite has shown the potential of some degree of amorphous phase formation [33,72,73]. It is expected that upon appropriate heat treatment, crystallization of one phase (e.g., alumina or zirconia) and precipitation of the additionally dissolved proportion of the other component from the amorphous state happens. This means that the amorphous phase transforms into a combined microstructure of alumina matrix with zirconia precipitates (i.e. alumina-hardened zirconia (AHZ)) and zirconia matrix with alumina precipitates (i.e. zirconia-toughened alumina (ZTA)). Hence, one purpose of this work is to produce a combined structure that benefits from the properties of both. Thus, knowledge of the possible phases for each component of the composite that form during heating is beneficial. The structures of zirconia having previously been discussed, here the stable phases of alumina at different temperatures will be reviewed.

Alumina has been found in several crystallographic forms. The major forms are γ, δ, θ and α-alumina [74]. The phases γ, δ and θ-alumina are the metastable phases and are called transient phases before the crystallization of the stable α-alumina phase takes place. γ-alumina has a cubic structure, where the anion oxygen atoms occupy the atomic sites and aluminium cations are distributed in octahedral and tetrahedral interstices. The α-alumina has a hexagonal close-packed (HCP) structure; and the transient phases δ and θ show an orthorhombic and β-Ge_2O_3 structure type, respectively [75]. The θ-phase has also been known as monoclinic structure [76].The sequence of phase transformations starting from γ has been reported as γ to δ at 850°C, δ to θ at 1100°C and finally θ to α at

above 1200°C [74,77]. In thermal spray coatings, the as-deposited structures have been in form of either γ or α phase. In addition, the transformation upon heat treatment beyond the transformation temperature was reported to be directly from γ to α, without intermediate phase formation [44].

To study the phase transformations of the alumina-zirconia system, Figure 1-5 can be used. This figure presents the equilibrium phase diagram of the pseudo-binary system of alumina-zirconia, which contains a eutectic point at 1860°C with a composition of about 58% alumina. The transformation of cubic zirconia solid into tetragonal phase completes at eutectoid temperature of 2260°C and its transformation into monoclinic phase in the presence of alumina happens at 1150°C. In addition to phase transformation temperatures, Figure 1-5 shows that alumina and zirconia have a complete miscibility in liquid state, while the solubility of alumina into solid zirconia is very low (less than 2%) and that of zirconia into solid alumina is nearly zero. The solubility of the zirconia into solid alumina, according to the equilibrium phase diagrams in some other references [121], may extend to about 5%.

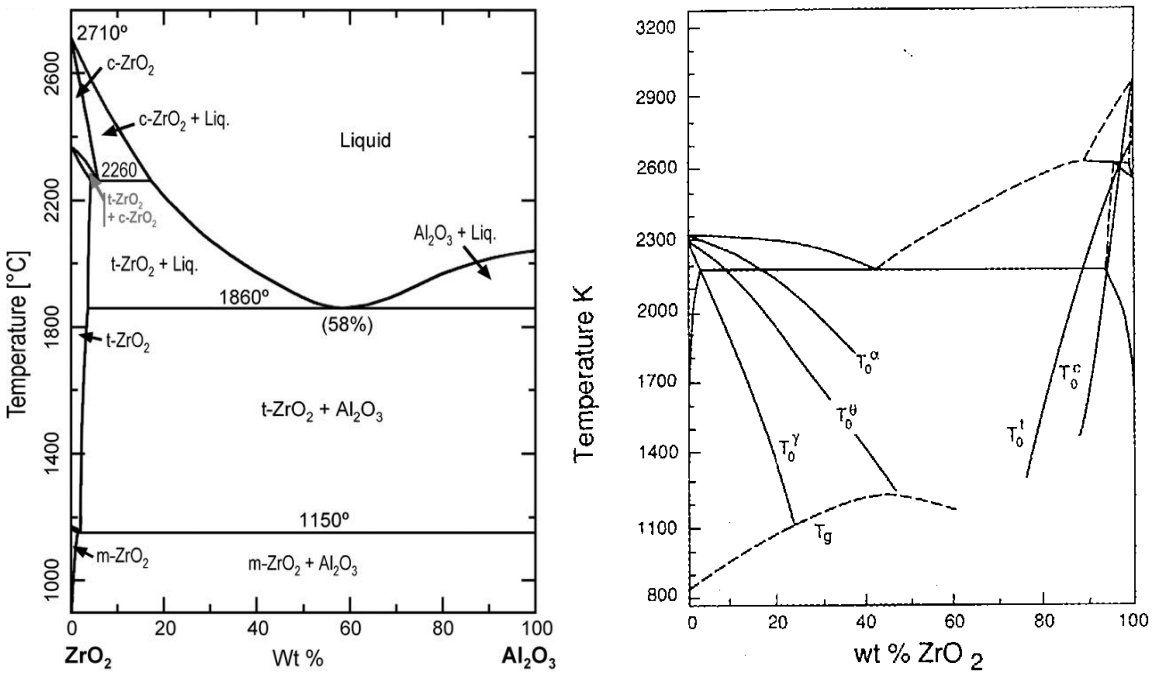

Figure 1-5 a) Binary equilibrium phase diagram of zirconia-alumina system [ACerS-NIST Phase Equilibria Diagram, CD-ROM Database, Version 3.0] [82] b) Critical cooling curves superimposed on binary equilibrium phase diagram of alumina–zirconia system [121]

After knowing the phase transformations in alumina, YSZ and alumina-zirconia binary system, it is important to know the structure of the as-sprayed coatings, since this is the structure that can go through transformation during heating and influence the eventual coating structure. The coatings are not expected to show the same structures which are predicted in the equilibrium phase diagram, because of the rapid solidification and non-equilibrium cooling rates during the spray process. Therefore, some un-expected structures might be observed in as-deposited composite coating. Some of the possible non-equilibrium (metastable) phases in alumina-zirconia system can be found in Figure 1-5(b) such as, γ- and θ-alumina or tetragonal and cubic zirconia. In addition, this figure predicts the formation of glass (/amorphous phases) at higher cooling rates when solidification happens at lower temperatures.

The formation of such phases (such as solid solution of zirconia or alumina with extensive solubility of the other constituent in solid state) is reported in this work.

1.5.1. As Sprayed YSZ, Alumina and Alumina-Zirconia Composite Coatings

According to the literature [44,54,68,78], as-deposited YSZ coating, applied by APS process, shows mainly tetragonal along with some cubic structure. Alumina, on the other hand, presents a cubic γ-crystal structure regardless of the plasma spray technique and powder feed size. Nonetheless, some reports show that application of nano-powder feed can end up with mainly hexagonal α-structure in conventional plasma spray [32].

During the spray process of alumina-YSZ composite coatings, the splats may be found in at least three conditions: splats formed of unmelted or partially melted feed particles; splats consisting of melted particles of either alumina or YSZ without mixing; or blended splats composed of melted and mixed alumina-YSZ. The unmelted particles in the coating may preserve the crystalline structure of the feed materials. Using APS process, the melted particles of unmixed alumina or zirconia in the coatings transform into structures almost the same as those described above, which means that zirconia in the composite coating is reported to change from mainly monoclinic to larger amounts of tetragonal, and the alumina appears as γ or δ-phase (that is, the transient phase before α-alumina forms out of γ) [79]. In addition, in quench-assisted APS coating the zirconia forms tetragonal along with cubic structure, while alumina is not observed in the XRD pattern [80]. Liquid injection processes, on the other hand, have presented mainly

tetragonal plus some cubic crystalline YSZ and γ-alumina [34,70,72,73,81]. The blended splats are strongly prone to amorphous phase formation [81,82].

1.5.2. Amorphous Phase in Alumina-Zirconia Composite Coating

Formation of non-crystalline phases is a notable feature of the as-deposited structure in composite materials such as alumina-zirconia. These phases, as mostly inseparable part of as-sprayed coatings have not been well considered. Amorphous structure is normally formed as a result of rapid solidification. Kim et al. [24], for the splat cooling rate in atmospheric plasma spray process, refer to an about 10^6 K/s, based on heat transfer calculations. On the other hand, the experimental results by Fauchais et al. [83] suggest a cooling rate of (100 to 600)$\times 10^6$ K/s, which is more than two orders of magnitude higher. At such high cooling rates the chances for ordering into crystalline structure during solidification from the melt are greatly reduced. In composite systems with low solubility such as the current system, this effect is more severe, because of a large atomic number (size) difference between Al and Zr, so that there are reports of almost fully amorphous coating during APS deposition of alumina-stabilized zirconia composite powders [24,82].

Kim et al. [24] sprayed alumina-zirconia with 42 wt% ZrO_2 stabilized with 2.3 wt% TiO_2 and 58wt% Al_2O_3 by APS using micron-size powder and obtained a fully amorphous coating. Sodeoka [33] reported the presence of the amorphous phase in 50/50 volume ratio of alumina/3YSZ (zirconia stabilized with 3 mol% yttria) spray dried nano-powders coated using the same process (APS). Alexander et al. [72] stated the same observation in

the SPPS composite coating of alumina-zirconia in either binary composite [73] or ternary with yttria [72], both with 10 and 20 mol% of alumina. They could observe the amorphous phase through transmission electron microscopy studies. Oberste-Berghaus et al. [81] sprayed both nano-powder and some comparatively larger particles (a few micron) of alumina-zirconia (zirconia was stabilized with 8 wt% yttria) using SPS process. They went farther and calculated the amorphous content based on the XRD pattern measurements. SPS coating of the nano-particles presented no amorphous phase, while the amount of this phase for the larger particles was as high as 55 vol%.

These studies revealed some trends for the possible sources of amorphous phase formation in various processes. However, for each specific process the factors leading to amorphous phase formation have to be determined. Therefore, one goal of this study is to investigate the parameters of the feed, system and substrate in SPS process that can effectively vary the amorphous content in the resulting coating.

1.5.3. Thermal Changes of Alumina-Zirconia Composite Coatings

Considering the high-temperature application of the TBC coatings, investigation of the as-deposited coatings characteristics may not be enough for evaluating the coating effectiveness [38]. This is because during the first service operation the as-deposited phases and the microstructural features (porosity, crack, inter-splat bonds, etc.) may undergo many changes. Such changes can severely affect thermal and mechanical properties during the next service operation.

YSZ [78,84], alumina [21,22,44,68] and their composite (alumina-zirconia) [24,70,85,86] have all been extensively investigated for crystalline and microstructural changes upon heat treatment, in addition to thermal cycling [84]. A summary of those results follows. In the experiment done by Sodeoka et al. [33] with 50/50 volume ratio of alumina/3YSZ after heat treatment at 1000°C for only 30 minutes the crystallization of the amorphous phase was completed. However, no further phase transformation from (γ-alumina + t'-zirconia) happened, even after 100 hours at 1500°C. By contrast, Chen et al. [78], in plasma sprayed crystalline γ-alumina, observed the phase transformation into α-alumina after half an hour at 1200°C. Moreover, Damani et al. [48] reported almost the same temperature for this transformation that means a heat treatment at 1180°C, for 12 hours.

Nazeri et al. [86], in fully amorphous alumina/pure zirconia composite deposited by sol-gel process, reported the appearance of crystalline cubic phase of zirconia at 600°C. Nevertheless, up to 1100°C (which was the maximum temperature in this experiment) no crystalline alumina showed up and the transformation from cubic to monoclinic phase started at 900°C (noticing that the zirconia was not stabilized).

In a part of their experiment, Kirsch et al. [87] studied the performance of amorphous alumina shell over zirconia nano-powders. The powders were heated, and while using in-situ X-ray diffraction the structural changes were monitored. When the powder consisted of amorphous zirconia within the amorphous alumina shell, the crystallization of cubic zirconia started at 700°C, transformation to tetragonal seemed to be at 950°C, and the monoclinic phase appeared at 1100°C. Nevertheless, since the maximum temperature in this study was 1100°C, the crystallization of alumina did not happen. On the other hand, starting with the tetragonal crystalline zirconia powder in the same shell of amorphous

alumina phase, the only observed transformation was the γ-alumina crystalline phase formation out of the amorphous shell; no phase change in zirconia was distinguished. In contrast to the above studies, Kim et al. [24], in Al_2O_3 / 2.3 wt% TiO_2-stabilized zirconia, reported the simultaneous crystallization of both alumina and zirconia at 945~946°C.

It can be seen that few of these investigations share the same transformation temperatures. No work was found, to the knowledge of the writer, to explain the possible reasons for these discrepancies in transformation temperatures. However, Kim et al. in 1999 [24] and Kirsch in 2004 [87] predicted that the apparent contradictions in the literature about the crystallization temperature of the amorphous phase in alumina-zirconia are based on the different amounts of this phase within the structure. However, no effort has been since made to investigate the ways that this content (if any) may affect the crystallization temperature and whether this can affect other transformation temperatures and possibly the resulting crystal structures. Therefore, an objective of this study was to find the way(s) in which the amount of the amorphous phase may affect the crystallization, the following phase transformation temperatures and the consequent crystal structures.

1.6. Objectives

Based on the above-mentioned details, the objectives of this project can be summarized as:

1) To enable the control of the coating microstructure by identification of influential parameters on microstructural features of the composite coating using the new technology of suspension plasma spray (SPS) with Mettech axial III torch;

2) To pursue larger amounts of amorphous formation or manipulate the amorphous content through parametric studies of the process as well as investigation of the sources for crystalline and amorphous phase in the composite material;

3) To determine the possible roles of the amorphous phase on the crystallization temperature and consequent transformation temperatures;

4) To investigate the changes in thermal and mechanical properties during heat treatment of the composite coating with focus on the roles of the amorphous phase;

5) To produce a new composite of alumina hardened zirconia (AHZ) and zirconia toughened alumina (ZTA) with nano-grains out of amorphous structure. Such composite structure may present the benefits of both structures.

Accordingly, this thesis started with chapter 1 containing background knowledge and the motivations for this research. In chapter 2 the general experimental procedures for tests, monitoring and measurement techniques are explained. Chapter 3 covers APS deposition of the composite to verify which powder size can produce higher amorphous content and to justify the use of nano-powder feed and involvement of SPS process. Some insights into the main sources of amorphous and crystalline phases in spraying the large and small particles have opened the way for production of larger amounts of amorphous phase.

Chapter 4 considers the suspension plasma sprayed coatings and in-flight particles. It starts with determining the role of different process parameters in the newly developed system of deposition with suspension plasma spray and provides an efficient set of tools (parameters) for managing the coating microstructure. This chapter then presents the study of the crystalline phases formed in the alumina-YSZ composite coating under

various spray conditions in SPS process and determines which crystalline phases are concurrent with larger amorphous content in the coating. It also discusses the transformation temperatures, including the crystallization temperature, within the mixed structure of the composite coating. Chapter 5 introduces methods for enhancement of the amorphous phase content in suspension plasma spray process. This chapter, in its subsequent section, provides a brief comparison between the results obtained by suspension plasma spray and atmospheric plasma spray processes in terms of crystalline or amorphous phase formation.

In chapter 6, the results from the performance of the composite coating deposited by SPS process before and after heat treatment, with consideration of amorphous role, are presented and partially compared with the conventional TBC material (8 wt% YSZ) coated by the same process. Finally, in chapter 7 conclusions are drawn and main contributions achieved in this study are summarized, and the grounds for further studies on the present material (pseudo-eutectic alumina-YSZ) are introduced. Moreover, other compositions of alumina-YSZ composites, surveyed for their ability in producing amorphous structure and nano-crystallinity, are suggested for further investigation.

Chapter 2 Experimental Procedures

This chapter covers the common experimental procedures for sample preparations in terms of systems used, as well as measurement techniques, monitoring systems and thermal/mechanical properties test methods. However, since the samples for different studies were produced by various feed powders and/or suspensions, the feed information and preparation conditions are explained in each corresponding section.

2.1. Spray Systems

Two different plasma spray processes were used in this investigation. The main process that is the focus of this work is the SPS process using liquid (wet) feed. The second, served as a baseline process, is the conventional or APS process using large dry powders. The equipment and systems applied were as follows.

2.1.1. Suspension Plasma Spray

The feed of the SPS process, in the form of liquid suspension, was gas pressurised from its container towards the injection nozzle. This nozzle was incorporated in the center of the Mettech axial III torch (Northwest Mettech, North Vancouver, Canada) that would allow the axial injection of the feed into the plasma jet. The plasma gun consists of three anodes and three cathodes operating on three power supplies (total power ranges from 50 to 150 kW). The Mettech axial III torch is shown in Figure 2-1(a) and (b), from front and back side respectively. In the front image, the outlet of the liquid in the center surrounded by three plasma outlets can be observed. The rear view (Figure 2-1 (b)) illustrates the

inlet of the suspension liquid and atomizing gas in the center, encircled by the three plasma gas inlets.

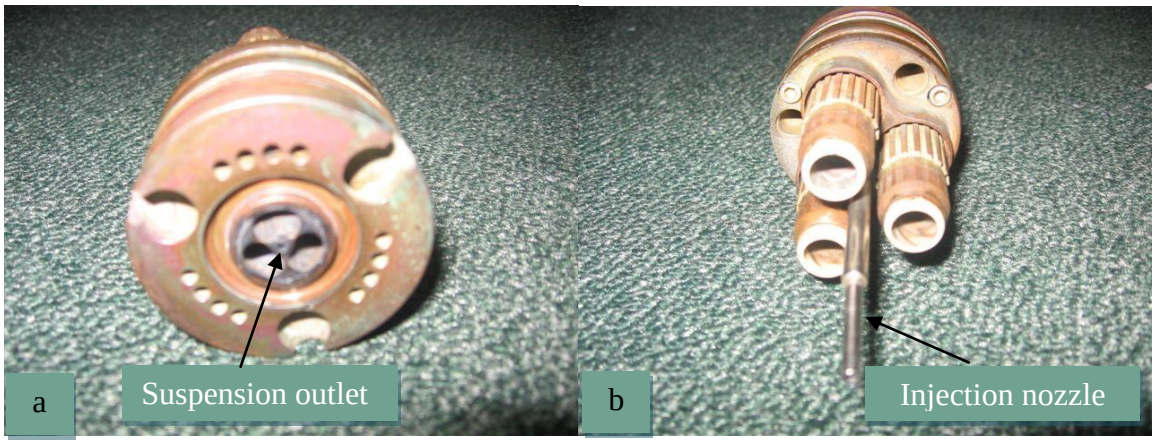

Figure 2-1 Mettech axial III plasma torch; (a) front and (b) rear view of the combined injection nozzle and the three plasma torches in axial III system

The liquid is gas pressurized into the nozzle, where it atomizes by either the plasma outside the liquid injector (in the center of the nozzle) or by an atomizing gas. In the latter case a thinner tube passes in the center of the liquid injector and carries the atomizing gas. The liquid flow rate is controlled by computer, so that the gas pressure automatically varies based on the specified liquid flow rate to keep it constant. A simplified arrangement of the system is shown in Figure **2-2**.

The spray distance was fixed at 50 mm from the nozzle exit in all experiments. Deposition passes had a 3 mm overlap. A cooling procedure was used to prevent overheating the substrate; this was especially necessary because of the short spray distance of the torch. The elements of the cooling process included front air pressure, nitrogen gas pressure from the back of the sample, and inter-pass pauses. The use and the pressure of the cooling gasses as well as the inter-pass pauses were manually varied to keep the substrate temperatures in the favourable range. In almost no case did the

substrate temperature exceed 600°C in the various samples, and for the most part it reached a maximum of 400°C.

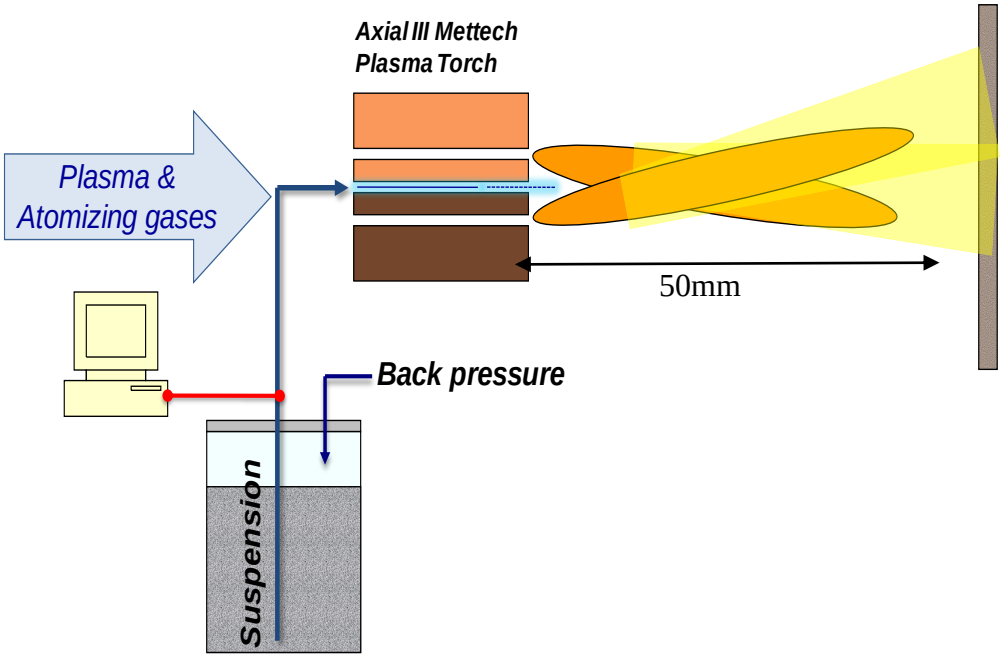

Figure 2-2 Simplified Suspension Plasma Spray (SPS) system with axial injection

2.1.2. Atmospheric Plasma Spray

For atmospheric or conventional plasma spray using dry powders the same Mettech axial III torch was used. The dry powder injection was performed from a 7/16" (11 mm) nozzle size with a feed rate of 21 g/min using an Argon carrier gas flow of 6 slm (standard litre per minute) . The depositions were done with 4 mm overlap and at 0.63 m/s spray robot speed.

2.2. Measurement and Monitoring Systems

2.2.1. Particle Size Measurement

The particle size analyses, for either the feed powders or the sprayed and collected powders, were performed using Laser Diffraction Particle Size Analyzer LS3 320 (Beckman Coulter, Miami, Fl., USA). The functioning of this instrument is based on the laser scattering technique and the fact that the intensity of the light scattered by the particles depends on the dimension of the particle.

2.2.2. Accura-Spray Diagnostic System

During spraying the powder feed, the size of which is nano or a few microns, in the suspension plasma spray process, the in-flight particle temperature and velocity were measured by Accura-Spray G2 (Tecnar Automation, St. Bruno, Canada). This is a diagnostic system based on indications from ensemble particle groups (rather than individual particles) that allows integration of the intensities of a group of small particles with low emitting power. In this way, a detectable intensity beyond the noise and plasma plume emissions can be produced. The precision of the G2 model for particle temperature is ±50°C and for velocity is ±20 m/s. The measurements were taken before deposition at the centerline of the torch at the spray distance where the substrate should be located.

Figure **2-3** represents the physical basis of the equipment. The main features of this monitoring system are the two optical fibres located at a fixed distance apart and aligned with the spray stream, that receive the signals of the particles through a lens. The measurement volume of each fibre is about $(3\times3\times20)$ mm^3 in which the signals from a group of 1 to 10 particles can be detected simultaneously. The number of particles in the

specified volume depends on the particles' size and flow rate. As the distance of the two receiver points is specified, there is a constant time shift for detections. The time-shift cross-correlation yields a precise measurement of the time elapsed between the two signals and the particles' average velocity [88].

The mean temperature is calculated using the two optical filters that allow the two wave lengths λ_1 and λ_2 to pass and be detected by detectors D_1 and D_2. The mean particle temperature is calculated according to the two-color pyrometry and the intensity of the fluctuations in the wave lengths passing through the two fibres.

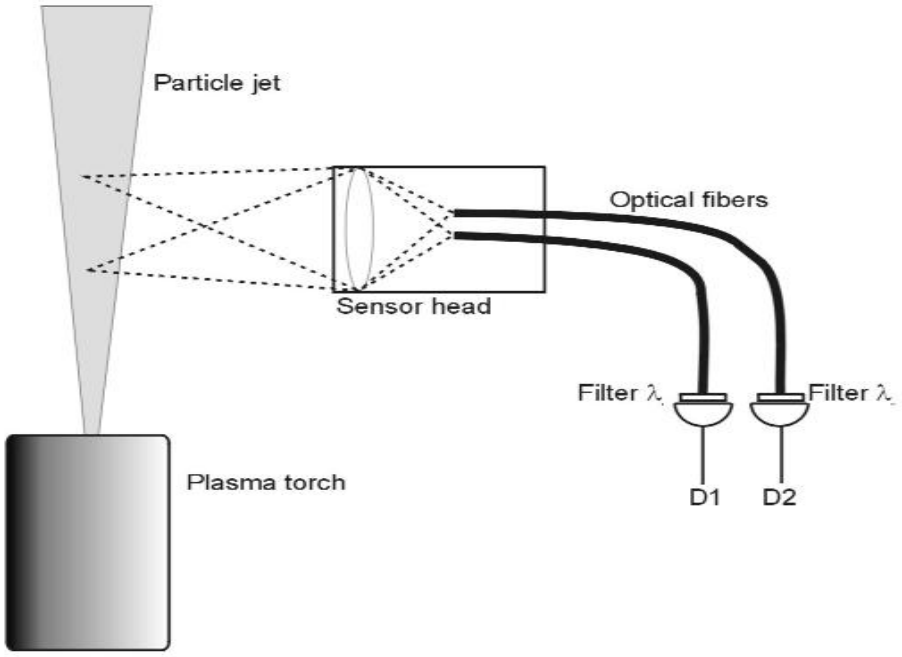

Figure 2-3 The operating basis of the particle velocity and temperature measurement used in Accuraspray sensor [88]

2.2.3. DPV2000 Particle Diagnostic System

For APS process dealing with large particles, the individual particle velocity and temperature were monitored using the DPV-2000 monitoring system (Tecnar

Automation, St. Bruno, Canada) in the center of the torch and at the spray distance from the jet exit where the substrate is to be located.

The main feature of this equipment, as can be observed in Figure **2-4**, is the double slits parallel to each other that detect the passage of the same particle at different times by transmitting the thermal radiation of the particle to the optical fibre through a focusing lens. For calculation of the particle temperature, the ratio of the signals detected from the two wavelengths is used, assuming that the particle is a grey body [88].

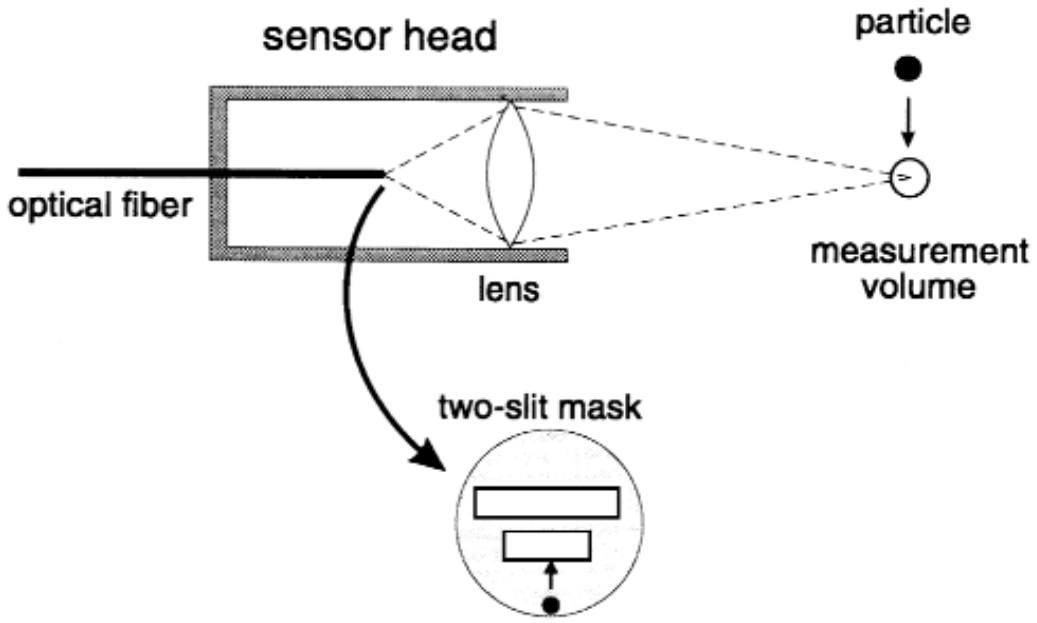

Figure 2-4 Physical basis for the DPV-2000 ensemble diagnostic system [88]

The particle velocity is measured based on time of flight using the two consecutive detections of the particle at the slits at a specific distance apart. According to the supplier [89], the velocity measurement error is 0.5% and the temperature measurement error reaches 3%.

2.3. Mechanical Tests

2.3.1. Microhardness

The microhardness test was performed using the AB-Buehler hardness testing machine (Buehler, Illinois, USA) at 300 grf for 15 seconds at 10 different locations with minimum distance of 3 times the indent diagonal in the cross section of the coatings. The basis for the functioning of the system is the Vickers hardness method with pyramidal indenter. A computer-aided camera provides the micrographs of the indent and electronically transmits them to the computer monitor where the hardness is calculated according to the operator's choice of the indent dimensions, and the result is directly digitalized. The probable errors are considered as the standard deviation calculated from the 10 readings.

2.3.2. Fracture Toughness

Fracture toughness comparisons were done using 10 kgf load based on the formula in Equation 2-1 [70].

$$K_{IC} = 0.016\sqrt{\frac{E}{H}}\frac{P}{C^{\frac{3}{2}}} \qquad \text{Equation 2-1}$$

Where E and H are respectively the Young modulus and the hardness, both in GPa, P represents the applied load and C is the average of half crack lengths from 10 indentations. For H values the measured hardness results in this experiment were applied. For Young modulus, a constant value of 28 GPa for 60/40 wt% alumina/YSZ composite was used based on the rule of mixtures and applying the data for plasma sprayed coatings from [90,91]. The H value for YSZ extracted from [90,91] was equal to 2.5 GPa.

2.3.3. Erosion Resistance

Erosion resistance tests were done for the coatings on Inconel 625 substrates bound coated with NiCrAlY, based on determination of material loss by gas-entrained solid particle impingement, and according to amended ASTM standard test method G76-83 [92]. The standard practice uses a small nozzle that impacts the abrasive-containing gas to the surface of the test specimen. This, results in a comparable measure of erosion in different samples that may be used to rank the materials based on this property. In this experiment the alumina abrasive powder of 100 grits was blasted with air pressure of 10 LPM (litre per minute). The exposure was done at a 30º angle (instead of 90º mentioned in the standard) for 30 seconds (instead of 10 minutes), spraying about 3.7 g/min of erodent powder to the coating surface. The shorter time was used for the sake of thinness of the coatings. Three replicates were used for each evaluation. The results were reported based on the volume loss of the material per unit weight mass of applied erodent solid. The errors bars are calculated from standard deviation of the three measurements.

2.4. High Temperature Performance

2.4.1. Thermal Conductivity

In order to study the thermal conductivity variation, the laser flash thermal diffusivity measurement was employed [93]. In this method, a thermal pulse generated by laser beam is applied on one face of the free-standing coating of 7 mm square (detached from the substrate using boiling hydrochloric acid with 50% concentration) and the temperature history on the opposite side is used for calculations of thermal diffusivity

through the coating thickness, as well as the specific heat capacity. The formula for correlating the thermal diffusivity to the thermal conductivity is given in Equation 2-2.

$$k = \rho \cdot C_p \cdot \alpha \qquad \text{Equation 2-2}$$

Where k is the thermal conductivity, C_p is the specific heat capacity at room temperature and constant pressure, and ρ is the density of the coating calculated based on the formula in Equation 2-3 and α is the thermal diffusivity.

$$\rho = \rho_{\text{theoritical}} \cdot (1 - \text{P}\%) \qquad \text{Equation 2-3}$$

In Equation 2-3, P% is the porosity percentage that was measured by image analysis techniques under the SEM with 500X magnification. In addition, $\rho_{\text{theoritical}}$ was calculated based on the rule of mixtures and according to the individual densities of the components and the proportion of each phase within the initial mixture. The value used for theoretical density of alumina is 3.55 g/cm^3 and for zirconia it is 5.8 g/cm3.

2.4.2. Thermal Cyclic Test

Thermal cyclic tests for coatings, on Inconel 625 substrates bound coated with NiCrAlY, was done for 20, 100, 250 and 500 cycles on sets of 3 samples. The cycles included heating the samples in an induction furnace to 1080 ºC in a 15-minute time period, holding at temperature under air atmosphere for 1 hour to allow homogenous temperature profile through the coatings and then cooling down in 15 minutes to room temperature using air jet cooling. The life time and the resulting structural and microstructural changes were then studied.

2.5. Measurement Techniques

2.5.1. Microstructure and Porosity

Field Emission-Scanning Electron Microscope (FE-SEM; Hitachi S4700) was used to image the coating microstructures in both secondary electron (SE) and back scattered (BS) modes. This microscope, in addition, was used for energy dispersive spectroscopic (EDS) chemical analysis, compositional mapping, and for high-resolution microscopy (HR-SEM).

SEM (Jeols JSM-610) microscope was utilized for image analysis at 500X magnification and the average porosity was determined from measurements in 10 locations. Calibration thresholds were selected between two reference materials, namely aluminium foil and the mounting material. This method is useful for large porosities in the coating. It is, thus, unable to detect porosities with a dimension of less than 0.5 μm at this magnification [28]. All microscopic evaluations and micrographs on the coatings were done on the cross section of the samples.

In addition, the in-flight particles were studied using the same microscopes and microscopic techniques. The in-flight particles were provided by spraying the powder into a large container of water, collecting and eventually air drying the resulting particles. The microscopic investigations were done in two different methods. In the first method, the particles were glued to a polished stainless still substrate using conductive glue and coated with gold, and then the micrographs were taken to view the morphology and a rough estimation of their sizes. The second method of particle studies was done on the sectioned view of the particles. For this purpose, the collected and dried powder particles were mounted in resin and polished, and then gold coated.

2.5.2. Amorphous Phase Measurement

Two distinct methods were used to evaluate the amorphous content that resulted from changing the spraying conditions. The first method uses the XRD patterns, which in this work are provided by Bruker D8-Discovery diffractometer (Bruker AXS, Inc., Madison, WI, USA). The second is based on the differential scanning calorimetric (DSC) graphs produced by the TG96 (SETARAM Inc., Newark, Ca, USA) machine. Description of each method is as follows.

2.5.2.1. Measurement Based on XRD Patterns

In the first method the X-ray patterns from the coating surface using Cu-Kα radiation and acquisition of 0.01°/sec were used. In this method, the area under the humps in the background of the XRD patterns that are characteristic of the non-crystalline structure were measured. The ratio of the hump area to the total area of the XRD pattern, including hump and sharp peak areas, represents the amorphous percentage in the structure. This ratio was measured within the range of 20° to 90°, unlike the usual method used for mainly amorphous materials with comparatively small number of crystalline peaks that are measured in a small range of angles below 40° [94]. For this measurement, the peak-fitting program GRAMS/AI from Galactic package [95] was used. The peak types selected for hump areas (diffused peaks of amorphous phase) were Gaussian and the sharp peaks (crystalline phase) were mixed Gaussian-Loranzian. This selection was based on trial and error for the maximum correlation factor of greater than 99% and chi factor (representing the goodness of the fitting process) mostly less than 0.5 in the overall resulting curve fits. The iterative curve fittings selected to be up to 50 runs were done by

the software. The standard deviation of the calculations based on 5 to 7 readings were considered as the probable error in the results.

2.5.2.2. Measurement Based on DSC Graphs

The second method for comparison of the amorphous contents in this study used the DSC graphs. These curves were also used for determining the transformation temperatures, and they were the basis for selecting the heat treatment temperatures as well.

The heating and cooling rates were selected as 5°C/min, which is the minimum attainable with the present equipment, to allow any unexpected transformation to be detected and the role of superheating and undercooling to be at a minimum. This rate was kept constant throughout the entire work to eliminate its role on transformation temperatures. The tests were undertaken in a range from room temperature up to the maximum temperature of 1500°C to find any possible delayed transformations in metasble phases. This is also the temperature before which the tetragonal to monoclinic zirconia transformation should happen.

The application of DSC curves in amorphous phase measurement was based on [96], where the area under the endothermic peak at the crystallization temperatures, known as the "crystallization peak," is employed in the calculation of the amorphous content. The curves with larger crystallization peak area represent larger amorphous content [24,97]. Likewise, the area under the peak for any other transformation was basically selected as a representative of the amount of the initial phase in that transformation. The fixed error of 8%, suggested by the equipment supplier was considered as the probable error for these measurements.

To measure the absolute value for the amorphous content in this method, a fully amorphous reference sample would be necessary. However, since these measurements of amorphous phase were for comparison purpose, the crystallization peak areas with arbitrary units are used.

2.5.2.3. Data Validation

Study has shown that amorphous phase evaluations based on XRD pattern are more accurate when the amorphous contents are less than about 20 percent, whereas DSC crystallization peak is more reliable for larger proportions of this phase [97]. It is important, also, to note that the results from thermal analysis are mass-based while the XRD results are volume-based data. So the absolute values of the changes in the results from the two methods cannot be directly compared and only the trend of the changes can support the other test results.

A linear regression for a group of randomly selected data from various experiments in this work was used to investigate the correlation between the results from the two methods. Figure 2-5 illustrates a reasonable agreement and close values to the linear relation. Thus, both methods can be applicable for comparison purposes and long DSC analyses are alternatively replaced by XRD pattern calculations.

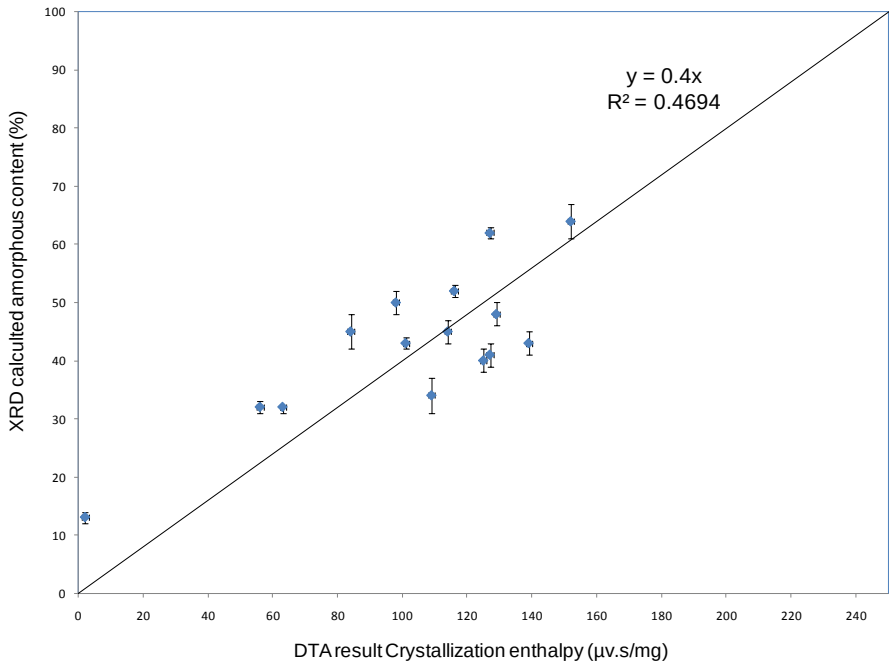

Figure 2-5 Linear regression of the data from XRD and DSC evaluation methods of amorphous content

2.5.3. Grain Size Measurement

Grain size was measured based on the Scherrer's formula in Equation 2-4 [98]. For these calculations, the most reliable peaks (without overlapping or with minimal overlapping) for each phase were selected as follows: Planes (111) for cubic zirconia or (110) for tetragonal zirconia both at 2 θ about 30°, (200) at about 68° for γ-alumina and (300) at about 46° for α-alumina phase.

$$t = \frac{0.9\lambda}{BCos\theta} \qquad \textbf{Equation 2-4}$$

Where t is the diameter of crystal particle, λ the monochromatic X-ray wave length, θ the diffraction angle and B is the broadening of diffraction line measured at its half at maximum intensity (in Radians).

The best curve fitting using the "peak fitting" function of GRAMS software [95] was used for peak measurements (width and angle). Smoothing process for some scans was necessary, when an overly corrugated appearance could cause erroneous peak measurements. The necessary data in terms of peak positions, concerning planes and FWHM (full width at half maximum) for each phase, after corrections with machine broadening data, are then used for grain-size calculation. To eliminate the machine broadening effect, the formula in Equation 2-5 was used.

$$B = \sqrt{b^2 - \beta^2} \qquad \text{Equation 2-5}$$

Where b is the peak width at FWHM and β is the machine broadening effect.

Machine broadenings are determined from the corresponding peaks of the above-mentioned planes in a LaB_6 single crystal. It is expected that the peaks in a perfect single crystal are without broadening by different crystallite orientations. Hence, if instead of an extremely sharp peak (line) a peak with width β appears in the XRD pattern, it can be related to the machine broadening effect.

2.5.4. Phase Analysis

To measure the amount of each crystalline phase within the crystalline portion of the structure, XRD patterns have been used. In this application, the peak intensities have been used for calculation of the phase ratios. However, in this study coatings normally include some amorphous phase, which results in a background hump that can vary the peak intensities at specific locations where the humps are distributed. In addition, the texture (preferred orientation) is another issue in the coatings that results in intensifying some specific peaks related to the planes with larger number of repetitions. As a result,

the XRD patterns need to be refined to eliminate background and texture effects. The Rietveld refinement was applied with the help of the PowderCell program [99]. The Rietveld method, based on full X-ray pattern, applies all factors contributing to the peak intensity and refines the data by a least-square procedure until the difference between the observed and calculated pattern is minimized. For such refinement, the necessary exact structural data for each phase were taken from Pearson's Handbook of Crystallographic Data [100]. In addition, to achieve the best refinement there is a need for manual refinement by the experimenter throughout the process.

2.5.5. Lattice Parameter Measurement

Rietveld analysis was also used to determine the lattice parameters of the different crystalline phases. For this, the same PowderCell program was used.

Chapter 3 Crystalline Structure and Amorphous Phase Formation in Atmospheric Plasma Spray Process

This part of the study investigates the more appropriate feed size (nano or micron) for production of larger amounts of amorphous phase using conventional plasma spray process, and to justify the application of SPS process in this research. In addition, some initial insights into the amorphous phase formation during plasma spray process could be acquired to be eventually compared with the results of SPS process.

For this purpose, two different types of powder, Tosoh TZ3460A composed of 60/40 wt% alumina/3YSZ (Tosoh Inc. Grove City, OH, USA) and Amperite 750 consisting of Al_2O_3-ZrO_2 60/40 fused (nominal size range 5-22 μm) (H.C. Starck, Sarnia, ON, CA) were axially injected into the Mettech axial III plasma torch. The powders were sprayed under the conditions summarized in Table 3-1.

Coatings were deposited on mild steel coupons (2.5 × 2.5 cm^2 with 0.5 cm thickness) bound-coated with NiCrCoAlY. Each coating was produced by 12 deposition passes. After finishing each coating, the torch head was directed to a large water reservoir and for about one minute spraying was done into the water at a 30-50 cm distance from the torch exit. The resulting in-flight particles, cooled down in water, were next collected and air dried. The collected powders went through size distribution analysis. In both the collected powders and the coatings, the amorphous contents were measured using the XRD and DSC techniques.

Table 3-1 Spray condition for the two types of powders and the resulting particle condition and coating thicknesses

Spray Condition / Powder	Total Gas (slm)	Plasma Current (A)	Gas Composition ($Ar/N_2/H_2$)	Spray Distance (mm)	T_p (°C)	V_p (m/s)	Coating Thickness (mm)
Amperite	120	200	10/80/10	100	2455	245	302
Tosoh					2250	222	463

Figure 3-1(a) to (d) presents the morphology of the feed powders and suggests that the approximate size ratio for Tosoh to Amperite powder is 3 and the average size of the Tosoh powder is initially 45 μm.

Figure 3-1(a) shows the Tosoh powder as large agglomerates of nano-particulates with a large number of nano-pores that are clearer in the magnified image in Figure 3-1(b). This figure also suggests a loose connection among the particulates of the agglomerate. Figure 3-1(c) presents the Amperite 750, a powder of comparatively large fused and crushed particles with sharp corners and dense structure. In this powder, no stabilizer was observed, based on XRD pattern assessment. Figure 3-1(b) from Tosoh powder at 100 times higher magnification than in Figure 3-1(d), clearly shows the particulate size differences. The XRD phase analysis of the initial powders showed that the Amperite 750 powder consists of a combination of monoclinic and tetragonal zirconia (with no trace of stabilizing agents, e.g., yttria), and α- and γ-alumina phases. Tosoh powder, on the other hand, shows tetragonal YSZ and γ-alumina.

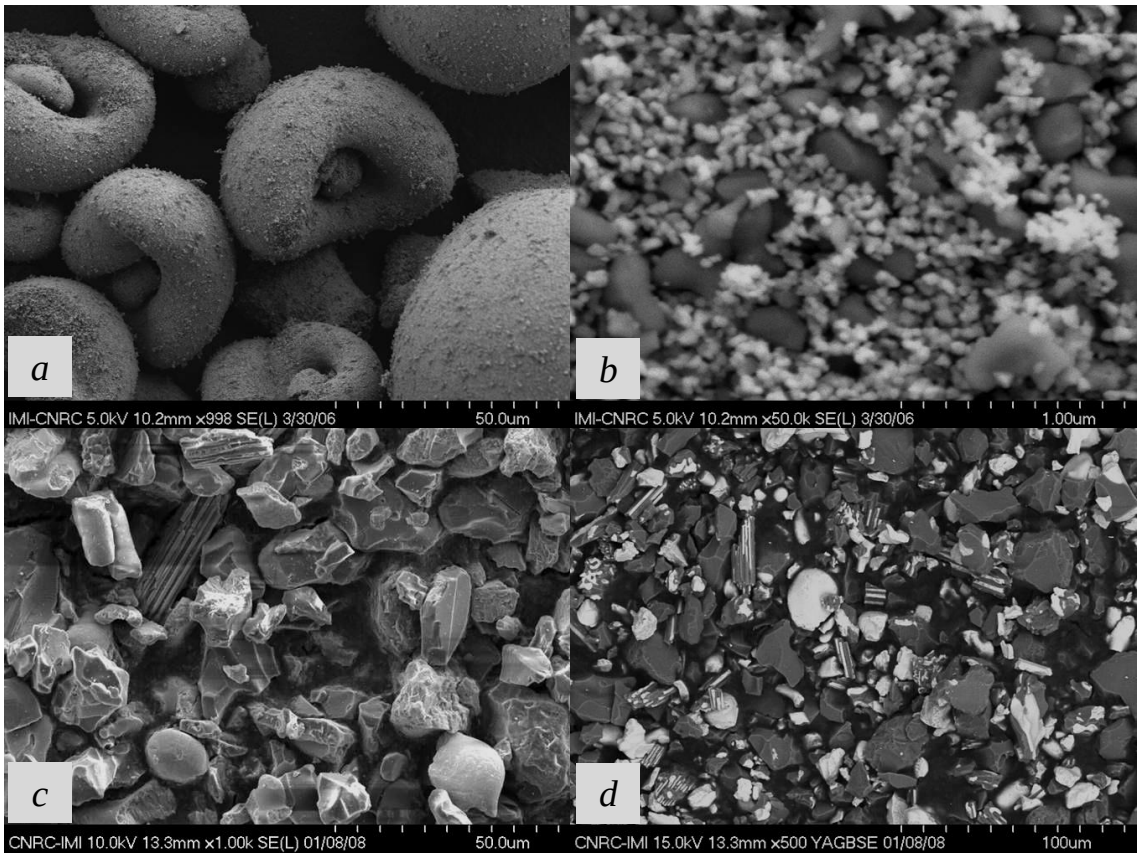

Figure 3-1 Feed powders, a) Tosoh powder at 1kX and b) Tosoh powder at 50kX and back scattered mode; c) Amperite 750 at 1kX and d) Amperite 750 powder at 500X and back scattered mode

3.1. In-Flight Particle Study

The particle size analysis of the collected Tosoh sprayed powders into water shows an average size of 46 µm (14-90 µm), while the Amperite 750 collected particles have an average size of 15 µm (6.7-23 µm range), which is practically the same as the initial feed size. This indicates that no fragmentation, either before or after melting in plasma, has happened.

Figure 3-2 illustrates an assessment of the particle temperature of the Amperite 750 at different distances from the nozzle exit using DPV2000. This figure shows the relation between particle temperatures and spray distance in which the particle temperature decreases with increasing the distance. Based on this figure, assuming an almost linear

relation, it is expected that at the distance of the water surface from the spray nozzle exit (30-50 cm), particle temperature to be below the melting point of both components of the composite (alumina, which has the lower melting point, melts at 2050°C), so that they could have solidified in-flight before entering the water.

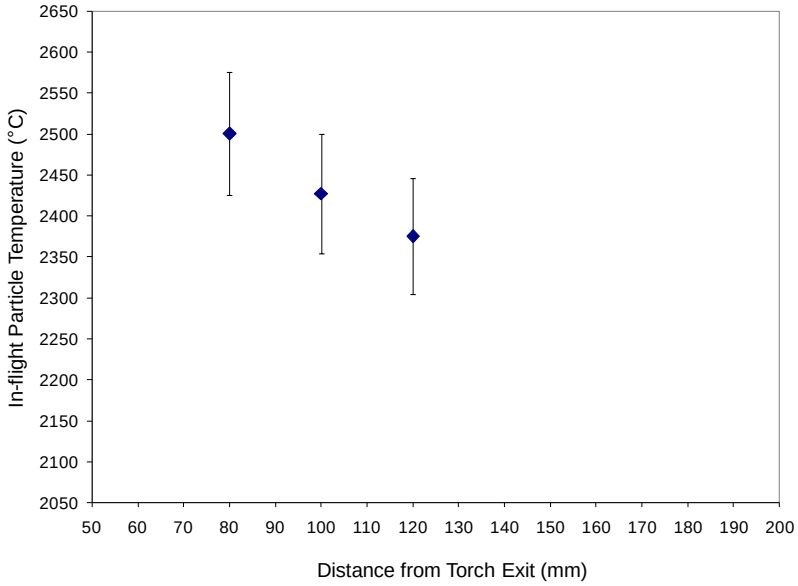

Figure 3-2 Variation of Amperite 750 particle temperature with the distance from the nozzle exit

The microstructure of the resulting collected particles from the two types of powders can be compared in Figure 3-3. Tosoh powders, according to the initially well-mixed particulates of the two components (alumina and YSZ), generally end with appropriate mixing-in as sprayed particles. The collected particles from this powder in Figure 3-3(a) contain large and small pores. These particles can be categorized as unmolten, partly molten and fully molten particles, which are shown in Figure 3-4. The unmolten particles, as in Figure 3-4(a), are still porous but with larger particulates than the initial powder, because of sintering during flight in the plasma jet. Fully molten and solidified particles shown by the arrow in Figure 3-4(b) are dense with mostly large pores in the center. Figure 3-4(c) is an enlarged view of a partly molten particle that suggests how this

transition from porous into hollow sphere is happening. When the melting starts from the surface, the melt front progression sweeps the submicron pores away and makes them coalesce with each other while moving toward the center. Thus, they leave several large pores or merge into single pore in the center, and a shell-like molten particle forms.

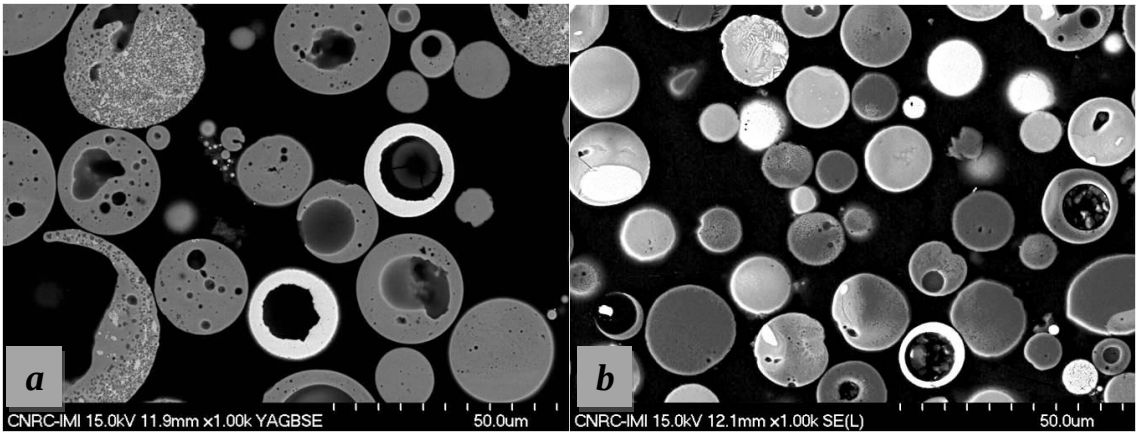

Figure 3-3 Sectioned view of the collected in-flight particles into water after spraying under similar plasma spray conditions, a) Tosoh and b) Amperite 750

This phenomenon of shell formation by Tosoh particles can justify the constant particle size observed between the initial and collected powders. However, while the majority of the nano- or submicron-size pores are annihilated into larger pores, plenty of them are still dispersed within the particle. The porosity of the feed particle plays an interesting role in the resulting phase analysis of the solidified particles, as will be discussed later in this section.

Figure 3-5 illustrates the collected particles of micron-size fused and crushed Amperite 750 powders. According to their spherical shape, these particles have been almost completely molten, but with a variety of mixing behaviour. They can be categorized as fully unmixed single component, partly mixed and fully mixed particles. The unmixed components can be seen as white YSZ particles and dark alumina particles in Figure 3-5(a), with dendritic solidification. In the partly mixed particles of Figure 3-5(b), grains

of unmixed portion are dendritic, and no grain can be seen in the mixed area at the left side or in the fully mixed particles (indicated by arrows in the same figure). Ultra-high magnification at 50kX by SEM in Figure 3-5(c) of the fully mixed particle presents no sign of the crystalline grains that would suggest the structure to be amorphous.

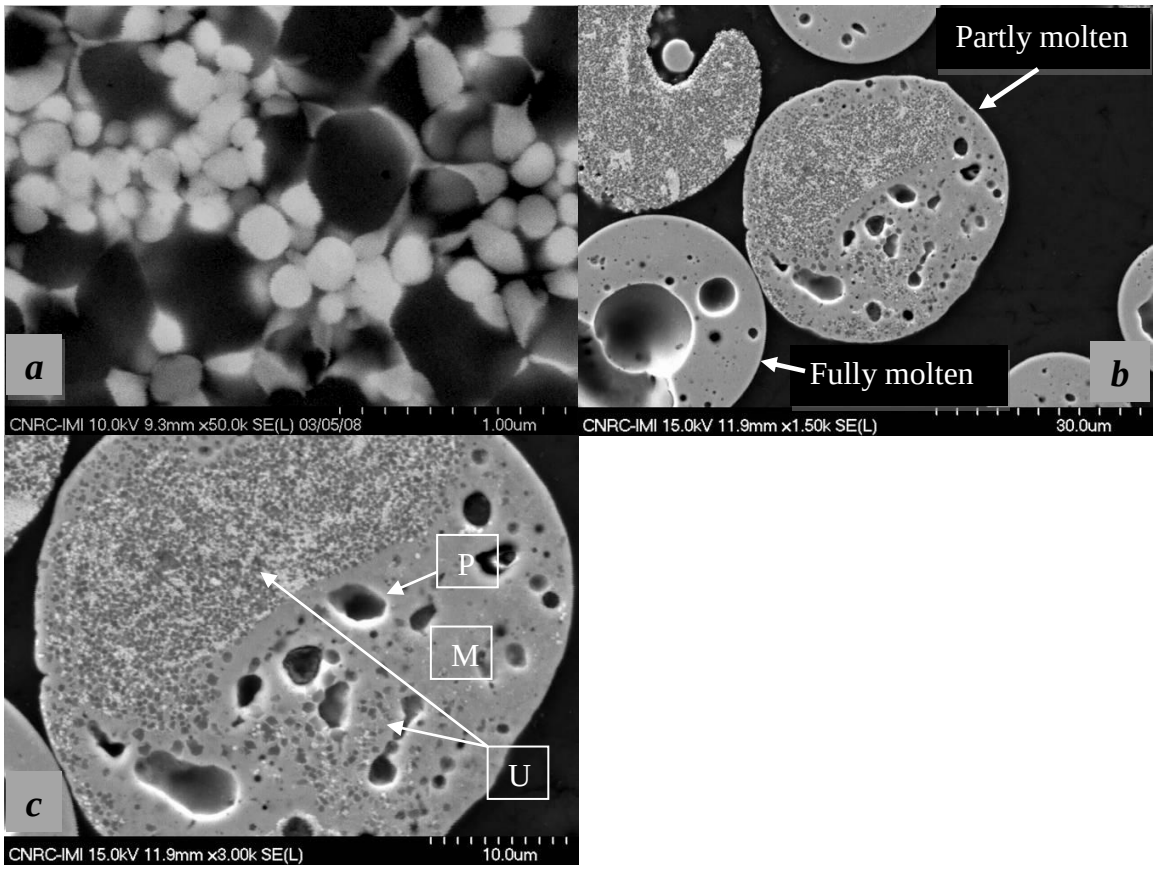

Figure 3-4 Sectioned view of Tosoh collected powder: a) unmolten particle; b) fully molten-resolidified particle and partly molten particle consisting of c) unmolten region indicated by U, molten region M, and enlarged pores designated by P.

Particles with complete melting and mixing were the common category between the two types of powders. Figure 3-6 is an SEM micrograph with EDS (Energy Dispersive Spectroscopy) elemental mapping of the same particle observed in Figure 3-5(c). It shows almost complete homogeneity in the composition and uniform distribution for both aluminium and zirconium atoms resulted from full mixing of the two components. Since

alumina and zirconia have very low mutual solid solubility, this could have only happened after complete melting.

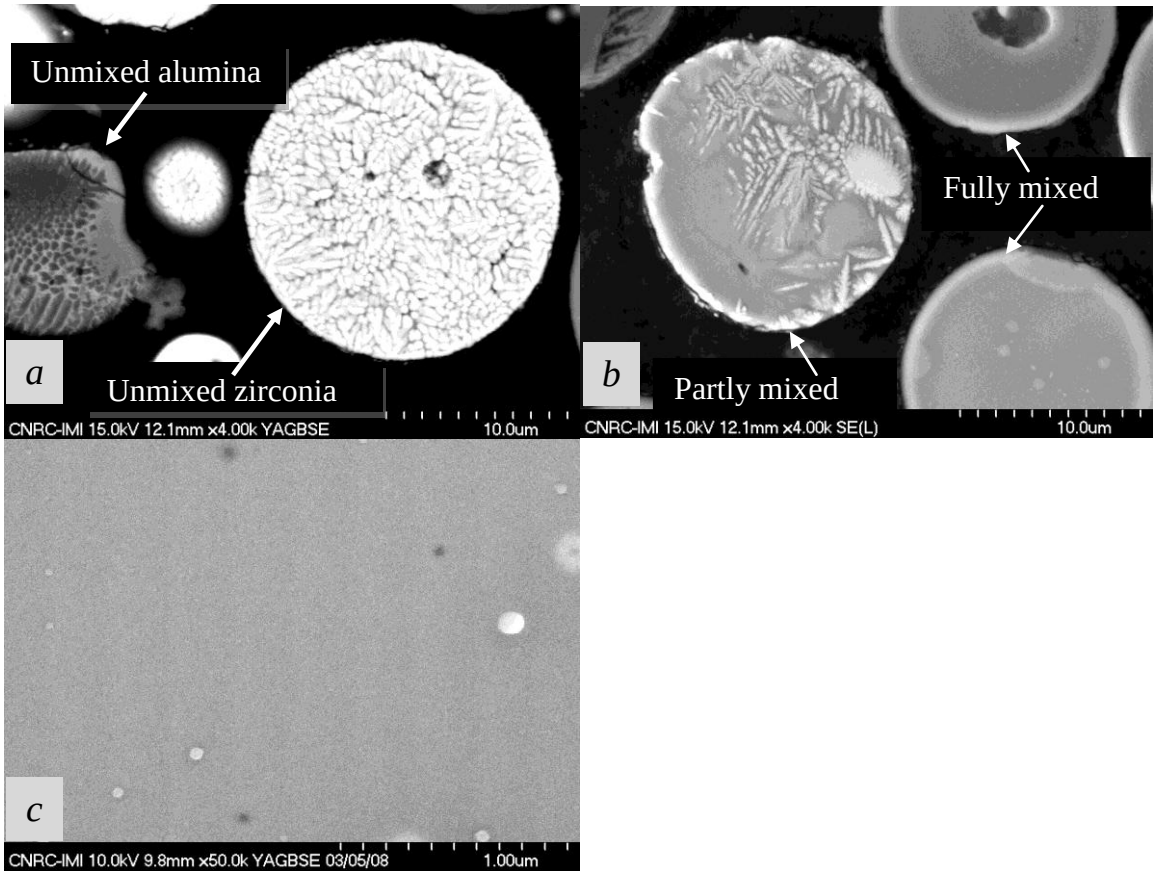

Figure 3-5 Sectioned view of collected in-flight particles from Amperite powder sprayed by conventional plasma spray: a) unmixed; b) partly mixed and fully mixed particles; c) high resolution microscopy of the fully mixed particle at 50kX showing no sign of crystalline grain throughout the particle

The EDS evaluation of some of these particles, however, shows off-eutectic compositions typically 36/11 or 29/41 for the atomic ratio of aluminium/zirconium (eutectic atomic ratio is 1/1). This indicates that also the particles with non-eutectic compositions show a good potential for amorphous phase formation. The reason for this is the high immiscibility in solid state of alumina and zirconia that according to Ando et al. [101] makes the formation of the amorphous phase more probable even at compositions far from eutectic. This fact impairs, to some extent, the importance of initial composition of

the composite on amorphous phase formation in plasma spray coatings. This means a highly amorphous structure can be obtained also in off-eutectic compositions during plasma spray process; and a deep eutectic composition is not essential.

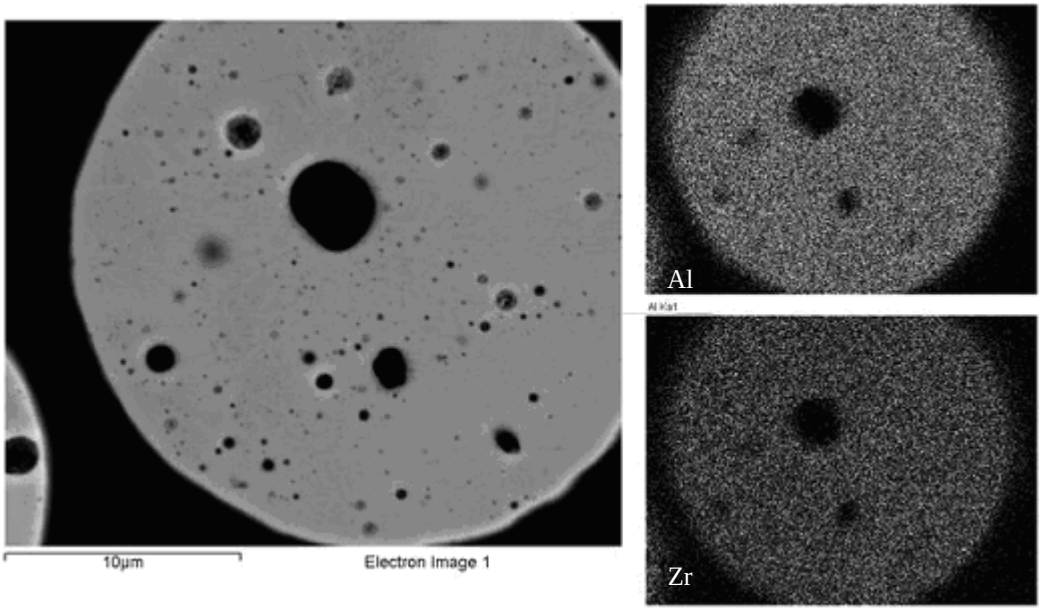

Figure 3-6 Sectioned view of fully molten and mixed particle with no sign of crystalline grains (left) and its EDS elemental mapping (right) showing homogenous distribution of aluminum and zirconium atoms

On the other hand, among the same group of fully mixed particles some behave differently during solidification, as depicted in Figure 3-7. The details within the particle of Figure 3-7(a) are shown in Figure 3-7(b), (c) and (d), retaining the same letters as in Figure 3-7 (a). Figure 3-7(b) shows the exterior part of the particle that has formed a nano-eutectic structure with about 10 nm alumina and 20 nm YSZ lamella; the interior part with the crystalline structure appears in Figure 3-7(c), which presents equiaxed cellular grains of less than 1 µm size centered by the pores. Moreno et al. [102], in rapid solidification of the alumina-zirconia melt droplets on copper surface, found a laminate size of 50 nm for zirconia and 100 nm for alumina at cooling rates of about 10^3 K/s. Comparing the laminate sizes in the present structures with the results of Moreno et al.

and assuming a linear interpolation, the cooling rate for these particles can be roughly estimated as about 5×10^3 K/s. This cooling rate, of course, depends on many factors including the particle size. This comparison proposes a much lower cooling rate for the in-flight solidified particles than the cooling rate for the actual coating splat, which can be more than 10^6 K/s [48].

In a close look at the interface between the two types of structure in Figure 3-7(d), it can be seen that the thickness of the eutectic lamella in the interface is not changed and it has the same thinness as in the outermost part of the solidifying particle. This indicates that the reason for the formation of the cellular grains is not the slowing down of the cooling rate from the outer to inner parts and nucleation on the solidified eutectic phase; rather the solidification has originated from the pores as nucleation sites and at comparatively higher temperatures inside the particle. According to Figure 3-7, it is assumed in this supposition that the entire bulk of the molten particle is at temperatures below melting point. However, points farther from the particle surface (closer to the center) are at less undercoolings due to low thermal conductivity of the material for homogenizing the temperature and elimination of the temperature gradient from surface to the center of the particle. The solidification front originated on the pores has next faced the solidification front started from outside at very high cooling rates and the two solidification fronts have come to rest in the interface.

The homogeneity of the particle suggests that the cellular grains inside are supersaturated solid solutions. The EDS evaluation under SEM, on the particles with entirely cellular grain structure, confirmed the happening of supersaturation and formation of 36/13 atomic ratio of aluminum/zirconium (or 0.36 atomic ratio compared with less than 0.01

atomic ratio of aluminum/zirconium in saturation limit of alumina with zirconia and 1/1 ratio for eutectic composition). Such supersaturation is against what was expected in a low solidification rate at high temperature, where the solute atoms beyond the predicted saturation limit (by equilibrium phase diagram) can diffuse out to the remaining liquid phase. The occurrence of supersaturated solid solution in the coating may be investigated, as will follow.

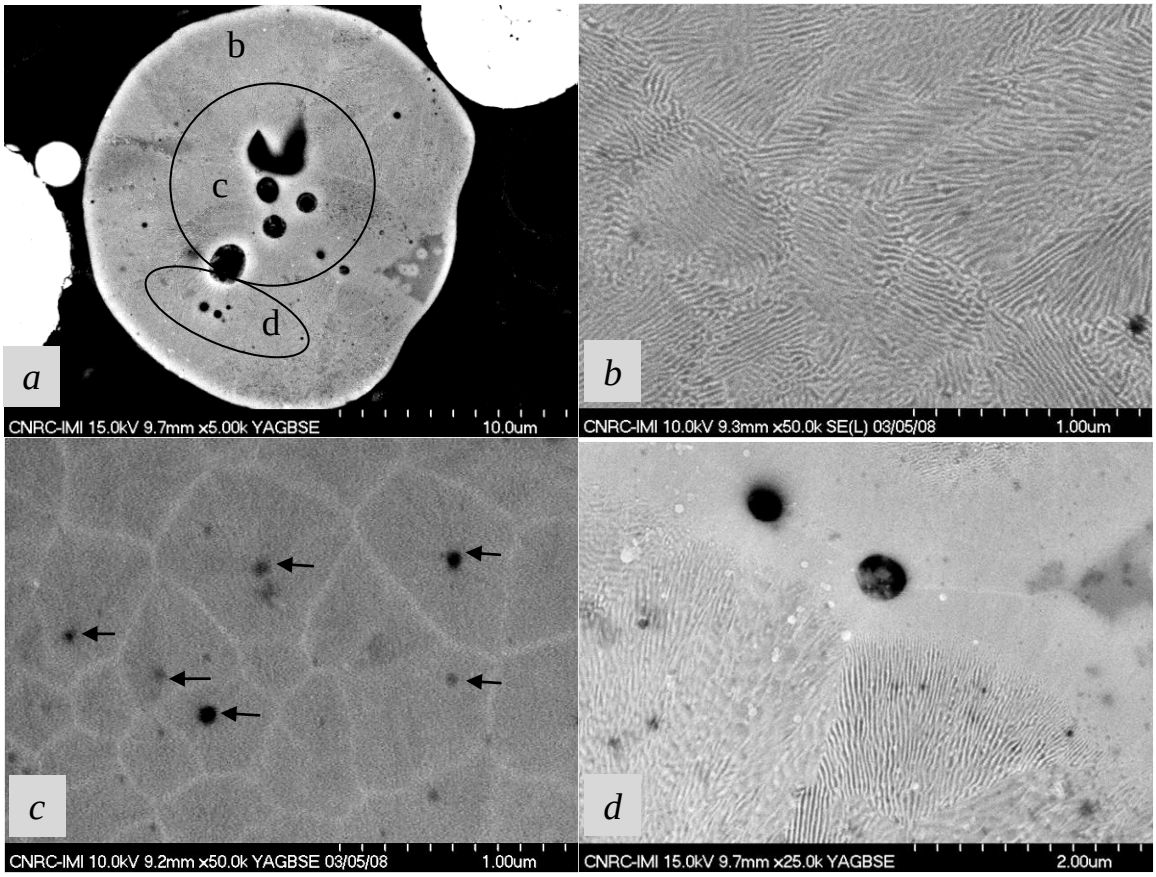

Figure 3-7 Structural features in an in-flight particle sprayed, solidified and collected into water: a) a typical particle; b) magnified external part and c) magnified internal part of the particle; and d) interface area of the two phases

Enhanced solubility in the solids can be seen in XRD patterns by shifts in the characteristic peaks of the parent material as a result of changes in lattice parameter [98]. Substitution of some zirconium or yttrium atoms by smaller aluminium can shrink the

unit cell of the YSZ structure. The other possibility for this dissolution is the allocation of much smaller aluminium atoms in the interstitial positions of the YSZ structure (either cubic or tetragonal), which can result in expansion of the unit cell. The former case can bring a positive shift to specific peaks and the latter results in a negative peak shift toward smaller angles. Thus the peak shifts are decided based on YSZ crystal structure and the position that the aluminum atom can take within the unit cell. In this, study such structural investigation is done based on the Rietveld analysis using PowderCell software.

3.2. Coating Structure and Amorphous Formation

The resulting coatings from the two different powders can be compared in Figure **3-8**(a) and (b), that show the coatings from Amperite 750 and Tosoh powders, respectively. There is a considerable difference in the coating microstructures, including clearly higher porosity and surface roughness in the coating from Tosoh powder. The reason can be related to the formation of a large number of shell-like particles with large core porosities. In such particles (forming hollow droplets) bursting upon impact can cause splashing that results in both more porosity and a rough surface.

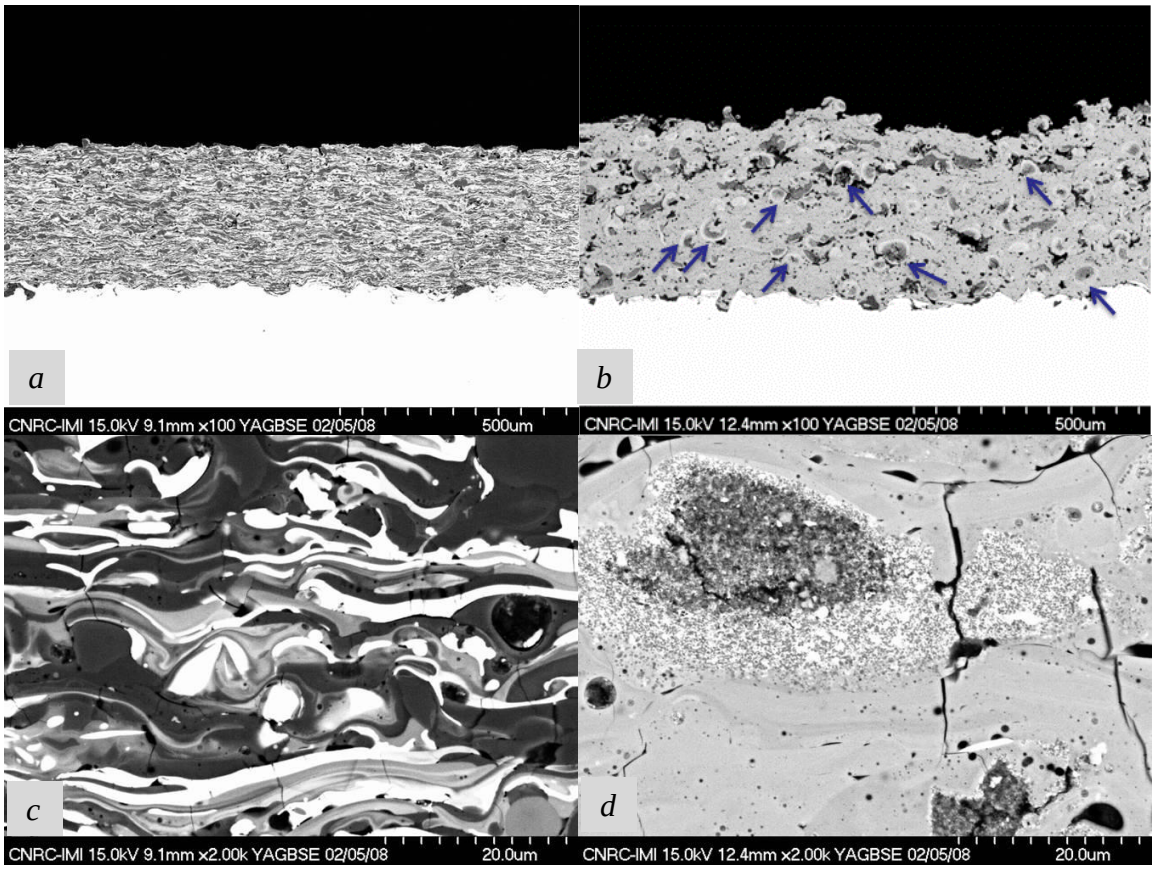

Figure 3-8 Coating microstructures: a,c) using Amperite 750, 60/40 alumina/zirconia; and b,d) Tosoh 60/40 alumina/3YSZ powder

At higher magnification as in Figure **3-8**(c) and (d), the comparison of the splat cross sections is possible. The Amperite 750 powder coating shows a structure consisting of distinct dark alumina and bright zirconia splats, in addition to some grey mixed splats. Tosoh powder coating, in contrast, shows a uniform structure of grey well-mixed alumina and stabilized zirconia. This uniformity is due to the intimate contact of the particulates that helps their easy mixing (upon melting) within the plasma jet.

Another notable finding in this experiment with Tosoh powder is shown in Figure **3-8**(d). This figure shows an unmolten particle in the coating that presents segregation of zirconia particulates toward the exterior of the particle and concentration of the dark alumina particulates inside. According to SEM assessment of the initial powders, the particles of

this composite powder were formed of uniformly distributed alumina and zirconia nano-particulates. Therefore, this segregation has to have happened during the plasma spray process. The reoccurrence of the segregated particles in the coating is shown by arrows in Figure **3-8**(b). This segregation of zirconia toward exterior regions was previously reported in the collected powders after melting and re-solidification, as well as in the coatings of this composite [81]. This phenomenon in both solid and liquid state may be attributed to the higher electrical polarity (stronger dipole) of zirconia molecules that causes a higher tendency of zirconia to expose itself to the ionic environment of plasma at the exterior parts of the particle. According to basic chemistry [103], molecules with covalent bonding between dissimilar atoms form electrical dipoles. These dipoles are the result of the higher density of the shared electrons around the ions of atoms with smaller size (atomic number) and/or higher electronegativity. The larger the difference between the atomic number and the electronegativity of the atoms involved in the bond, the higher the polarity of the dipole [103], so that in extreme conditions the bonding turns to ionic type. Thus the degree of polarity of the dipole translates to the degree of ionic character of the bond or molecule. In the bond with oxygen (atomic number 8 and electronegativity 3.44), Zr (atomic number 40 and electronegativity 1.33) shows a higher ionic characteristic compared with Al (atomic number 13 and electronegativity 1.61). On the other hand, the materials can best dissolve in electrolytes of similar polarity (i.e., molecules with higher ionic character can more readily dissolve in ionic electrolytes). Therefore, a higher affinity from zirconium oxide toward the plasma (as an ionic electrolyte) can be expected, which causes a stronger attraction toward the surface of the particle and/or melt.

It is, however, clear that when such a particle receives heat during long enough period of time for complete melting, full mixing provides an ideal condition for amorphous phase formation by intimate contact between dissimilar particles. Thus, the structure resulting from well melted particles shows a good uniformity. On the other hand, in the distinct lamella of the Amperite 750 powder coating, the chances for in-flight mixing seem to be lower than those of nano-particulates such as in the Tosoh powder.

However, Figure 3-9 suggests a second possibility for mixing and amorphous formation that can happen in the intersplat regions of the coatings upon impact. Figure 3-9(a) shows the SEM micrograph of the interface area of a solidified alumina splat (dark layer) coated by zirconia (light-color splat). It can be seen that there is a region of alumina mixed with zirconia (shown by arrows in this figure) beside the interface. This has happened due to re-melting of the alumina by the large heat input of the upcoming molten zirconia particles with temperatures higher than the melting point of alumina (T_m for alumina is 2050°C and for zirconia is 2700°C).

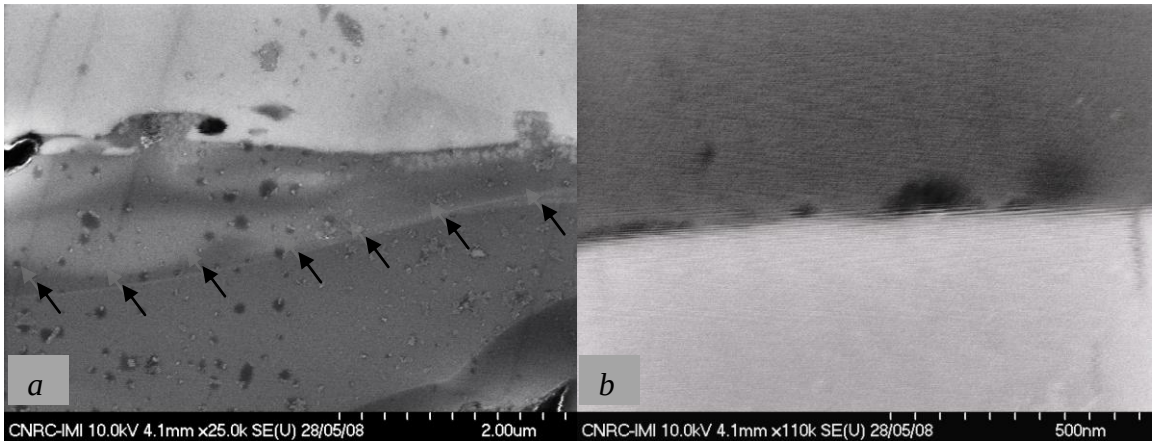

Figure 3-9 Intersplat conditions in cross section of the coating: a) zirconia splat deposited on solidified alumina splat and b) alumina splat on solidified zirconia

In contrast, Figure 3-9(b) shows the interface when an alumina splat is deposited over the solidified zirconia splat. The distinct separating line between the two splats shows that in

this case such a mixed region has not formed. Amorphous phase formation at the interface area of the zirconia splat on the solid NiCoCrAlY surface was previously reported by Bartuli et al. [104]. They explained this as the result of re-melting and intermixing of aluminium and other bound coat elements into the upcoming zirconia splat. These observations, however, do not override the possibility of in-flight mixing in this kind of particle.

In mixing and amorphous phase formation upon impact, it should be considered that the total area of the interfaces (involved in the interface mixing) compared with the entire bulk of the splats (involved in the in-flight mixing) is limited. In addition, in this kind of mixing, it is mainly the splat with higher melting point that causes the intermixing upon impact. Thus, the chances for amorphous formation in this way are considerably lower than in the case of in-flight mixing.

3.3. Phase Analysis and Amorphous Phase Contents

The measurement of the crystallization peak area in DSC graphs from the two powders shows an amount of 109 units for Tosoh powder coating, against 49 units for Amperite 750 powder coating. This indicates a considerably higher amorphous content within the coating by Tosoh powder, which is simply due to the enhanced mixing resulting from the intimate contact between dissimilar nanometric size particulates.

According to the linear relation introduced in section 2.5.2.3 for the estimation of the amorphous content, a line slope of 0.4 can be used to convert the DSC results into XRD data. Based on this, the estimated amorphous phase for coating of Tosoh powder is less than 44 vol%. An approximation of the unmolten portion of the structure for Tosoh

coatings was possible using image analysis technique (assuming the area percentage to be equal to volume percent), which shows less than 25 vol% for unmolten part. The balance, equal to 31 vol% of the structure, which is neither amorphous nor unmolten solid, has to be in the form of solid solution formed according to the mechanism described above. This will be further investigated using lattice parameter measurements.

Figure 3-10 shows XRD patterns of the coatings from both powders, and the observed structures of the coatings are compared with the 7YSZ coating deposited by the same spray conditions. In the patterns of Figure 3-10(a) and (b), stabilized zirconia, either with alumina or without it, presents tetragonal structure as previously observed in APS process [19,105]. In the graph for Tosoh powder coating shown in Figure 3-10(b), although the 3 mol% yttria is just enough for partial stabilization, the stabilizing role of alumina dissolution in this structure has completely prevented any formation of monoclinic zirconia. By contrast, the XRD pattern of the Amperite 750 coating in Figure 3-10(c) shows a considerable amount of monoclinic phase. This is due to unmolten feed powders, the absence of yttria stabilizing agent, and the lack of extended dissolution of alumina in zirconia splats as seen in the micrograph in Figure **3-8**(c).

Quantitative evaluation of unit cell parameters using the PowderCell program [99] allows comparison of the lattice parameters *a* and *c* for 8 wt% YSZ-60 wt% alumina with those of 8 wt% YSZ without the addition of alumina. It was found that parameter *a* decreases from 3.6345 to 3.6306 and parameter *c* from 5.1196 to 5.0928. This suggests that the dissolution of alumina into tetragonal zirconia has to be substitutional so that the smaller radius of alumina has resulted in reduced parameters. The observed shifting in Tosoh powder coating with tetragonal structure has some deviation from the report of

supersaturation of cubic zirconia. In this report, by increasing the solubility limit from 4 to 40 mol% alumina, the unit cell of the cubic zirconia increases from 0.5095 to 0.5129 nm [106]. However, this report supports the possibility of supersaturation of the alumina into zirconia as observed in this experiment.

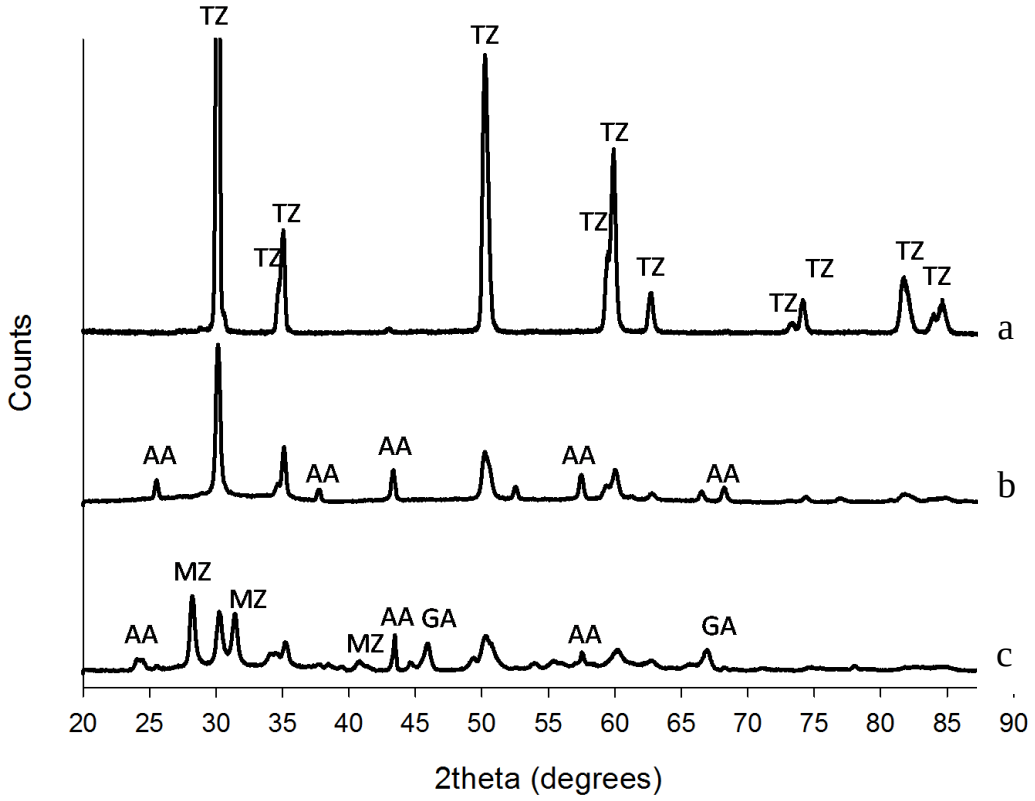

Figure 3-10 XRD patterns of the coatings: a) YSZ coating with tetragonal structure (TZ), b) Amperite 750 powder coating consisting of tetragonal zirconia (TZ) and alpha alumina (AA), c) Tosoh powder coating showing (TZ) and monoclinic zirconia (MZ) plus alpha (AA) and gamma alumina (GA)

3.4. Summary

In this study of the in-flight collected particles and coatings of pseudo-eutectic alumina-YSZ sprayed by APS process, several new facts concerning the crystalline and amorphous phase formation have been revealed.

Since the sizes of feed particles and of particles collected after spraying were constant, it can be proposed that in dry deposition of the powders by APS process, no considerable fragmentation of the particles in the plasma jet has happened.

The formation of supersaturated solid solution of alumina-YSZ was observed in the collected particles. The cellular grains nucleated on the pores, and solidification at slow rates started from inside the melted particle, but these grains were stopped at the border of the eutectic solidification front without releasing their excessive solute atoms, which in this case would have to diffuse into the solid rather than melt. Unit cell parameter measurements based on XRD patterns supported the formation of such a crystalline phase in the coating. This can be proposed as a new source of crystallinity in the sprayed coatings. Moreover, it suggests that in addition to amorphous phase, some of the alumina, which is absent in some XRD patterns, can be dissolved in crystalline zirconia phase with surprisingly high ratios (as high as eutectic composition).

Two major sources of amorphous phase were introduced. They include the in-flight melting and mixing of dissimilar materials, in addition to upon-impact mixing when there is a considerable difference between the melting points of the two components.

Segregation of zirconia from alumina in unmolten Tosoh particles and its migration toward the exterior regions of the particle, which was previously reported in melted particles, was also found in solid state. The reason is suggested to be the higher polarity of the zirconia molecules in the electric field of the ionic plasma environment.

Agglomerates of nano-particulates yielded higher amounts of amorphous phase. Thus for the sake of amorphous studies and enhancement of this phase in the coatings, application

of nano-powders using the suspension plasma spray process was selected to be used for the remaining parts of the work.

Chapter 4 Suspension Plasma Spray Coating Microstructure and Crystalline/Non-Crystalline Structures and Transformations

4.1. Controlling the Microstructure of SPS Coatings and Resulting Properties

Since SPS is a newly developed process, there is not enough information on the optimum condition for production of sound coatings. Therefore, the main goal of this part of the study was to identify the major parameters in the SPS process that can be used in manipulating the microstructure and help production of coatings with favourable integrity and reproducibility. To this end, Taguchi statistical method [107] has been used in design of experiment (DOE) to evaluate the importance of seven selected variables in microstructural characteristics of the coatings. The variables included feed, plasma torch and substrate-related parameters. The need to investigate a wide range of variables with the minimum number of experimental runs suggested the application of this DOE [107].

The variables and their two selected levels are listed in Table **4-1**. Among the variables in this table, the levels for solid content, torch condition and feed rate were selected based on the initial data suggested by the torch supplier, followed by preliminary trial and error to establish favourable working conditions. Additionally, the substrate roughness was in the range of what is used in the industry, and the robot speed was changed from medium to the maximum obtainable. The microstructural features and in-flight particle characteristics on which the effects of variables are studied include:

- Particle temperature, T_p, at substrate distance from the nozzle exit (°C)
- Particle velocity, V_p, at substrate distance from the nozzle exit (m/s)
- Vertical cracks average spacing (µm)
- Horizontal cracks average spacing (µm)
- Porosity content in the crack-free area (%)
- Thickness per pass of deposition or deposition rate (µm /pass)

The vertical and horizontal cracks in the coatings were individually assessed and counted per unit length or width of the coating. Five measurements were averaged per sample. The nature of the cracks can have significant influence on the properties of the coating. For example, it was observed that planar defects parallel to the substrate are more influential on mechanical properties [108] and thermal diffusivity [108,109] than is the total porosity. Porosity measurements using image analysis technique were done based on section 2.5.1.

Table 4-1 Variables and levels in Taguchi design of experiment

Variable		**Low & high levels**
A	Solid content in suspension	10 & 30 wt%
B	Auxiliary gas	H_2 & He
C	Torch condition (total plasma gas flow, gas composition, torch current)	(245 slm, 75 Ar/10 N_2/15 H_2 or He, 200 A) & (275 slm, 65 Ar/15 N_2/20 H_2 or He, 240 A)
D	Injected feed rate	1.3 & 1.8 kg/hr
E	Powder type	Nano & Micron
F	Substrate roughness	#24 & #60 (mesh size of alumina grit blasting)
G	Spraying robot travel speed	0.6 & 2 m/s

Following the parametric study of the process and the resulting microstructures, the role of microstructure on the mechanical properties (hardness) and thermal conductivity of the composite coating was investigated. Vickers micro hardness test according to section 2.3.1 was evaluated for selected samples. Thermal conductivity was evaluated by laser flash method [93] according to section 2.4.1.

To produce the feed material for SPS coating, first the nano-size powders were proportionally mixed to produce 5 mol% YSZ (equal to 8 wt% YSZ), which is the common TBC material in gas turbines and diesel engines. The powders used in this mixture included 3 mol% YSZ nano-power (Nano-Composite Powder, Inframat Advanced Materials, Farmington, USA; nominal size 30-60 nm) and 8 mol% YSZ (Nano-Composite Powder, Inframat Advanced Materials, Farmington, USA; size 30-60 nm). The resulting doped zirconia powders were then mixed with two different sizes of alumina powders. The alumina component was either nano-size (Nanostructured & amorphous Materials Inc. USA; nominal size 27-43 nm) or micron-size (Malakoff, Texas, USA; size 1.4 μm). The terms "Nano" and "Micron," respectively, will be used here for these mixtures. The mixtures with the larger size powders were ball milled in a concentrated suspension of 60 wt% solid for 24 hours before dilution to the final solid concentration. This procedure ensured homogeneous mixing and stabilization of the suspension. The nano-mixture was only milled for the same period for enhanced stability of the suspension. A weight ratio of 60/40 for the alumina/8 wt% YSZ was prepared and suspended in ethanol at 10 and 30 wt% concentrations. This resulted in four suspensions with different powder size ranges and solid contents. Suspension dispersion was done

using 9 cc Poly-ethylene-eimine (MW 25000, Alfa Aesar, Ward Hill, MA) and 4.5 cc Nitric acid (both with 10% concentration) for every 150 g of solids.

The wet analyses of the agglomerate size in different suspensions diluted in ethanol showed that the size ranges were closely comparable regardless of the initial particle size or solid concentration, and were all in the range of 10 μm. Specifically, the measurements showed 0.2~3 μm in 30%wt solid of micron-sized particle suspension, 0.2~9 μm in 10 wt% solid of the same powder and 0.2~5 μm in nano-size powder in 10 wt% solid suspension.

4.1.1. Roles of the Parameters on Microstructure

The summary of the evaluation results is shown in bar chart diagrams in Figure 4-1. The first column for every variable shows the effect of its variation from the low level to high level (as defined in Table **4-1**) on the corresponding parameter shown in this figure. The second column for each variable is the standard error to help compare the significance of the effects with the error. In this figure, the increasing or decreasing effects are specified as follows. When changing the variable (e.g., solid weight%) from low to high level has caused an increase in the specific structural parameter (e.g., vertical crack spacing) in the coating, the corresponding column is shown on the positive side of the Y-axis, and the decreasing effects of variables on the measured parameter are shown on the negative side of this axis.

By relating the particle temperature and velocity to the spray conditions, some general trends can be observed and will be discussed in the following sections.

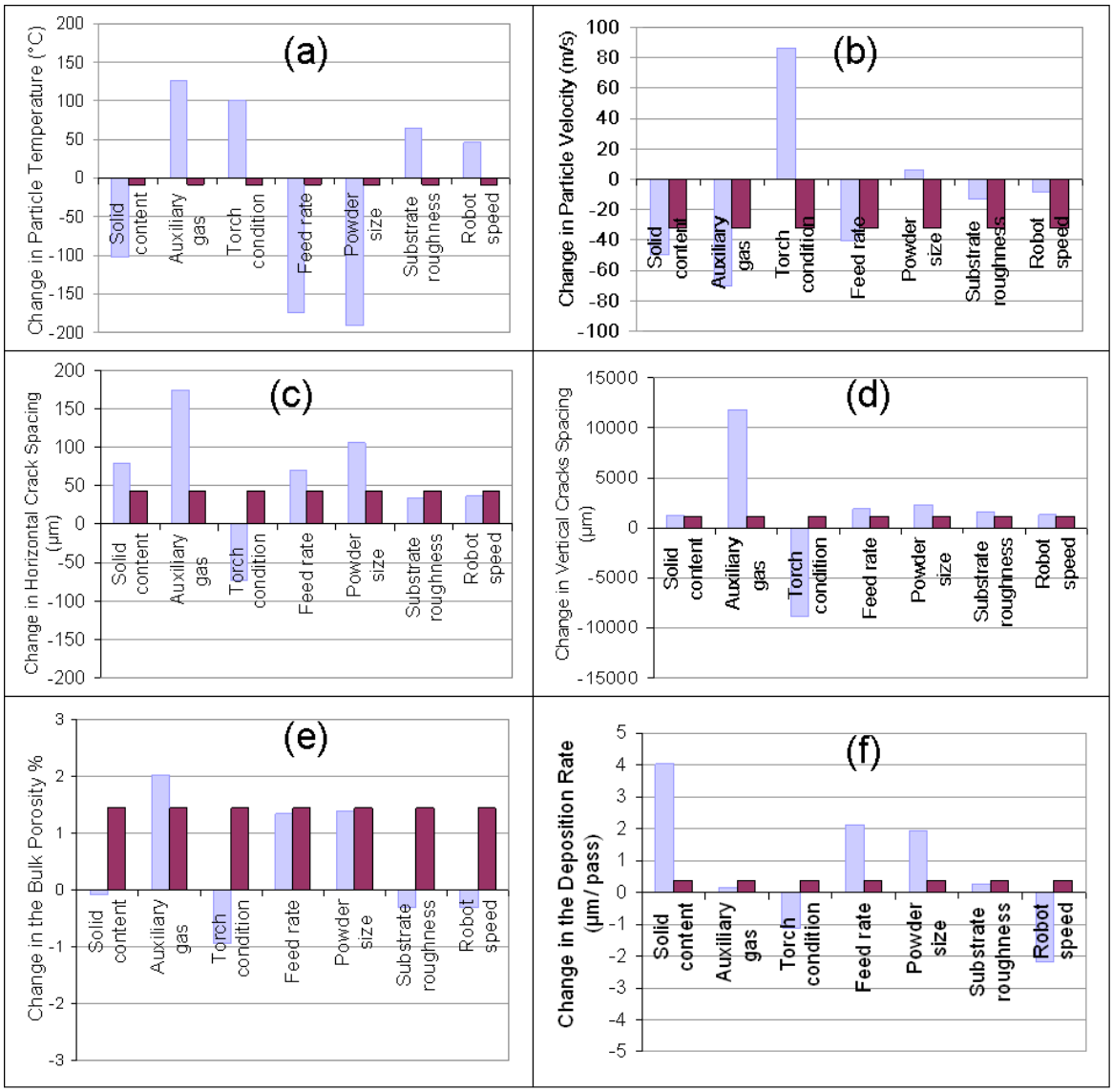

Figure 4-1 The averaged effects of the seven variables on particle characteristics and microstructural parameters in suspension plasma spray (SPS) process. X-axes showing the 7 variables and Y-axes presenting the change in the corresponding property due to change in the variables (bright columns), as well as the standard deviation (dark columns)

A. Solid Concentration

Increasing the solid content from 10 to 30 wt% in the suspension liquid, as observed in Figure 4-1(a) and (b), has decreased both particle temperature and velocity. The coatings from this lower temperature and velocity have shown no considerable change in vertical crack density, but the spacing of horizontal cracks through the thickness increased

slightly, as presented in the diagrams of Figure 4-1(c) and (d). Within the range of porosity detectable by the method used in these experiments (as explained in section 2.5.1), the porosity content of the coatings was not affected by the solid concentration. However, the solid concentration is found to be the most effective factor on deposition rate, as shown in Figure 4-1(e) and (f). The higher solid content in the liquid feed has produced thicker layers per pass, which can be translated to a higher rate of material deposition.

B. Plasma Auxiliary Gas

The plasma auxiliary gas was changed from the commonly used hydrogen to helium, to induce more porous microstructures suitable for applications like thermal barrier coatings. Helium is known to increase the plasma stability with its high viscosity at high temperature [5]. It also has a higher conductivity than hydrogen and generally produces a wider hot core area that promotes entrapment of a larger number of small particles, which could otherwise escape from the particle jet without deposition. The observed effects of replacing hydrogen with helium are summarized in Figure 4-1(a) to (f).

Interestingly, changing from hydrogen to helium auxiliary gas has shown the most drastic effect on almost all of the measured parameters in this work. By replacing H_2 with He gas, the average particle temperature increases and the average velocity decreases. One by one comparison, however, provides additional information, which may be extracted from Figure 4-2. This figure shows that at the same plasma torch conditions (in terms of total gas flow rate, plasma gases ratio and arc current) using He has dropped the resulting plasma power by 20 to 40 kW. This can be observed in the two different plasma

conditions of “245 slm total gas flow rate, 75Ar/10N_2/15 auxiliary gas, 200 A current” and “275 slm total gas flow rate, 65Ar/15N_2/20 auxiliary gas, 240 A current”.

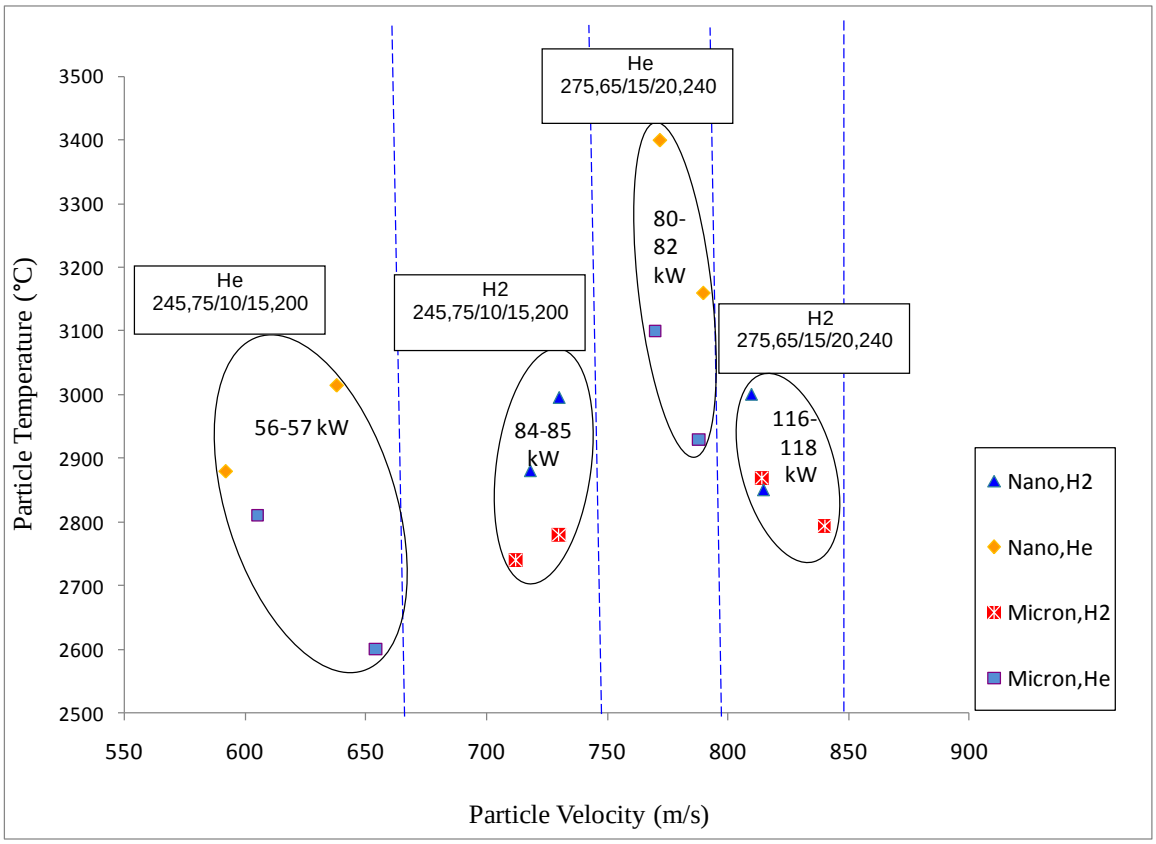

Figure 4-2 The effect of auxiliary gas, powder size, torch condition and plasma power on particle velocity and temperature

On the other hand, comparison between the two sets of experiments in Figure 4-2 clearly shows that using He auxiliary gas resulted in both higher velocity and higher temperature of the in-flight particles. This was the case even though only small differences of plasma power (around 80-82 and 84-85 kW) were recorded. This temperature increase, in spite of shorter heat exposure time at higher velocity, is a result of higher thermal conductivity by helium gas.

The SPS coatings produced within the range of variables in this experiment show a very dense microstructure. The porosity in crack-free areas ranges from a minimum of almost

zero, produced with hydrogen auxiliary gas, to a maximum of 8% in the case of helium. The two extreme microstructures of alumina-YSZ coatings are shown in the micrographs of Figure 4-3(a) and (b). It is clear that the high density of the coating in Figure 4-3(c) causes the vertical microcracks to develop within the structure, whereas the porous structure, especially in the case of distributed porosities as in Figure 4-3(d), eliminates the microcracks. A comparison of the particle temperatures and velocities indicated on the micrographs as (T_p, V_p) shows that for high densities a high particle velocity is necessary.

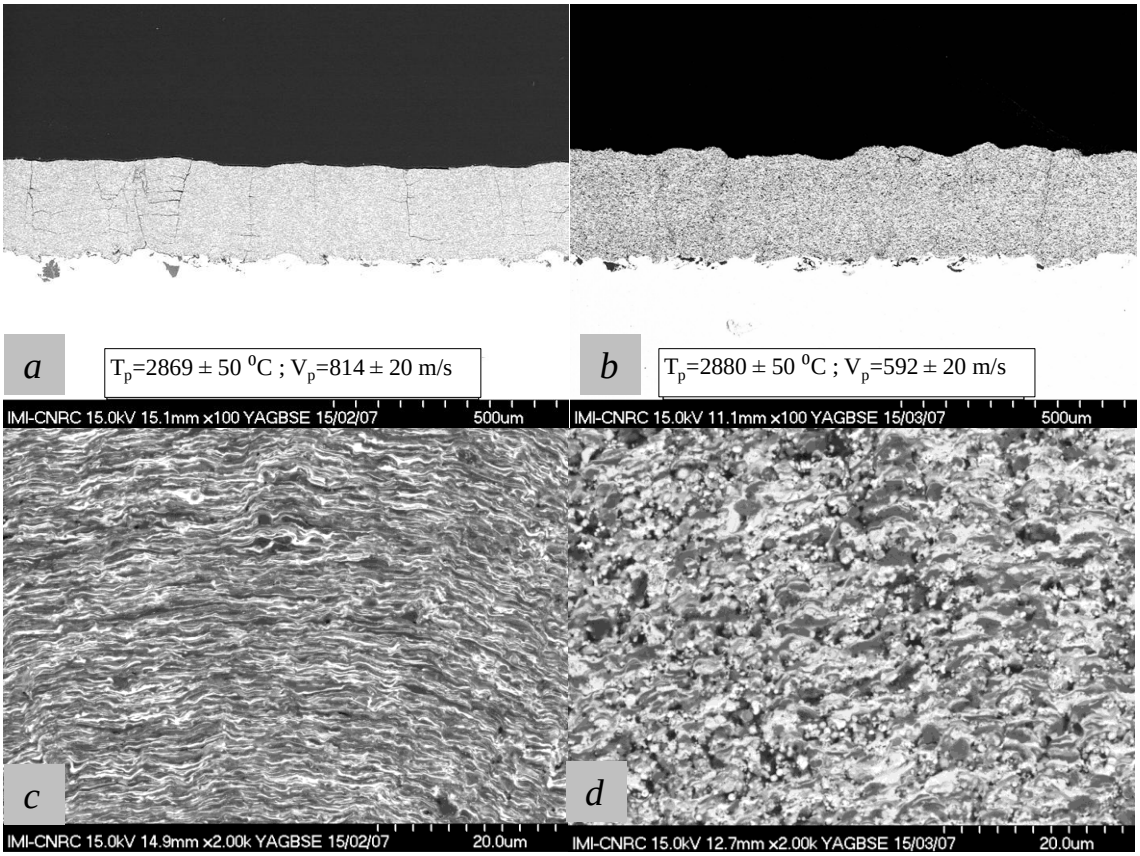

Figure 4-3 60/40 wt% alumina/zirconia suspension plasma sprayed coatings: a) resulting coating using hydrogen auxiliary gas; b) resulting coating using helium auxiliary gas at 100X; c) and d) same coatings as a and b, respectively, at 2kX

C. Plasma Torch Condition

Changing the plasma condition from low to high level, as described in Table **4-1** and based on the results in Figure 4-1(a) and (b), raised the particle temperature and, to a

greater degree, increased the particle velocity. At higher particle temperature and velocity, the density of both vertical and horizontal cracks increases. This may originate from formation of thinner splats that can more readily form vertical cracks during the cooling process. The horizontal cracks branch from the vertical cracks. In this way, the similar behaviour from both types of cracks may also be justified. The porosity remains invariant and the deposition rate decreases slightly.

A direct comparison, however, is difficult since the parameters of spray torch condition and auxiliary gas are not independent. To gain further insight into the effect, deposition runs can be grouped into four ranges of plasma power of 56-57, 80-82, 84-85 and 116-118 kW. Accordingly, the effect of plasma power on the particle characteristics is summarized in Figure 4-4. In this figure and its following discussion, the roles of other parameters are not considered. However, other parameters could have played their role in variation of the outcomes among the grouped samples (inside the ellipses in Figure 4-4). It can be seen that an increase in plasma power generally increases the particle velocity. At similar plasma power (81-84 kW), particle velocity in helium exceeds that in hydrogen, as shown in Figure 4-4(a). Nonetheless, the highest particle velocities are obtained with hydrogen. The temperature of the particles, however, does not follow a definitive trend, as seen in Figure 4-4(b). Generally, it was observed that the feed parameters are better tools for controlling the particle temperature than are the torch operating parameters.

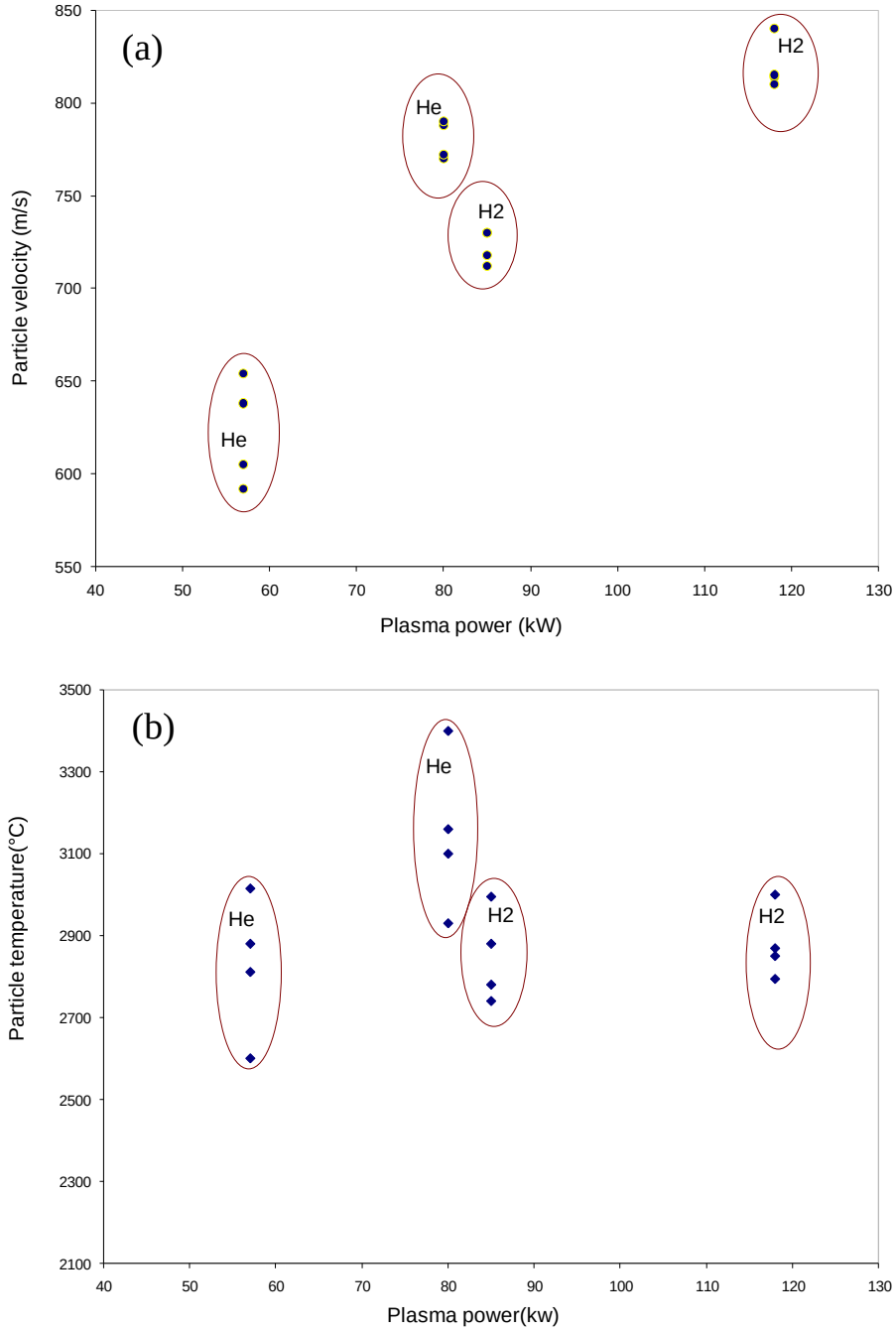

Figure 4-4 Plasma power effect on a) particle velocity and b) particle temperature

D. Feed Rate

Based on Figure 4-1(a) and (b), Taguchi analysis shows that increasing the feed rate decreases, both particle temperature and, to a lesser extent, particle velocity. As a result, Figure 4-1(c) and (d) shows that the microcrack densities do not show any considerable

variation. The porosity also was not affected by this change, as represented in Figure 4-1(e). This characteristic of the process that can tolerate the increase of the feed rate and deposition rate without introducing more structural defects in the coating is promising for higher production rates. It is noteworthy that the feed rate and the solid content have shown similar effects and may be interchangeably used in controlling the coating microstructure in the SPS process.

E. Powder Size Distribution

The effect of the initial particle size range on the coating microstructure was studied by changing nano- to micron-size alumina powders mixed with nano-size 8 wt% YSZ. This variation showed a recurring drop in particle temperature (T_p), in spite of the similar agglomerate size in the suspension that can be seen in Figure 4-2 and resulting average particle temperature shown in Figure 4-1(a). However, Figure 4-1(b) shows no significant velocity drop due to feed particle size change. The lower temperature from larger particle feed stock may be explained by the formation of dense particles within the plasma plume in comparison with the hollow particles that can result from nano-size suspension feed stock [110]. A second reason for higher T_p can be that the nano-particles which form loose aggregates are of considerably higher surface area, thus showing lower energy barrier for melting than solid micron-size particles in the aggregates. Experiencing the same velocity and spray distance, the nano-aggregates, more rapidly melted, will have more possibility to rise to higher temperatures.

In the resulting coating microstructure, while the density of vertical microcracks remained almost constant (Figure 4-1(d)), the horizontal microcrack spacing increased remarkably (Figure 4-1(c)). The lower microcrack densities observed with larger particles

can also be justified by the lower T_p, as the high particle temperatures can cause higher thermal stresses. The porosity content looks indifferent to the powder size variation (Figure 4-1(e)), which is somewhat unexpected. Considering the large standard error, a possible underlying effect may not be captured. The limited sensitivity of the porosity measurement method, also, has restricted the observation of the smaller pores (nano-pores) that might have affected the results.

F. Substrate Roughness

Keeping in mind that the substrate roughness has no effect on in-flight particle characteristics, this experiment shows that its variation is one of the least effective parameters on the microstructural features, as seen in Figure 4-1. Neither the porosity (Figure 4-1(e)) nor the deposition rate (Figure 4-1(f)) has changed, and even the microcrack densities (vertical/ horizontal; Figure 4-1(c/d)) have not been considerably altered by changing the substrate roughness.

Additionally, the averages of coating roughness on the substrates blasted with #60 alumina grit (Ra=3 to 4 μm) and #24 grit (Ra=6 to 7 μm) are almost the same, namely Ra=5.5 and 6 μm, respectively. The absence of strict correlation between the initial substrate roughness and the resulting coatings roughness is attributed to the small aggregate sizes comparable with the size of substrate roughness. The small particles at high velocity diffuse into the roughness asperities and after the first few runs of deposition the role of the substrate roughness diminishes significantly. This independency of the roughness between the substrate and coating suggests that the coating roughness can be controlled by spray condition for various substrate roughnesses. On the other hand, changing the initial particle size from nano- to micron-size powders

causes a slightly more considerable effect on coating roughness, namely, from Ra=5.1 to 6.3 μm.

G. Robot Travel Speed

The robot travel speed has changed neither the porosity (Figure 4-1(e)) nor the vertical/horizontal microcrack density (Figure 4-1(d/c)). A drop in deposition rate (Figure 4-1(f)) is simply related to less mass deposition time at higher robot travel speed.

The importance of the microstructural characteristics can be revealed when their effect on mechanical and/or thermal properties is investigated. Therefore, the role of porosity changes (due to variation of particle velocity) on hardness, as well as thermal diffusivity of the coatings was studied and summarized as follows.

4.1.2. The Effect of Porosity on Coating Hardness

Figure 4-5(a) presents the effect of particle velocity on the coating density, showing that coating density increases as a result of higher particle velocity. High particle velocity provides higher momentum for the splat flattening and results in enhanced intersplat bonding that has clearly improved the hardness of the resulting coating as illustrated in Figure 4-5 (b). This figure shows that with even less than 5% porosity the coating hardness drops to less than one third of the highly dense structure.

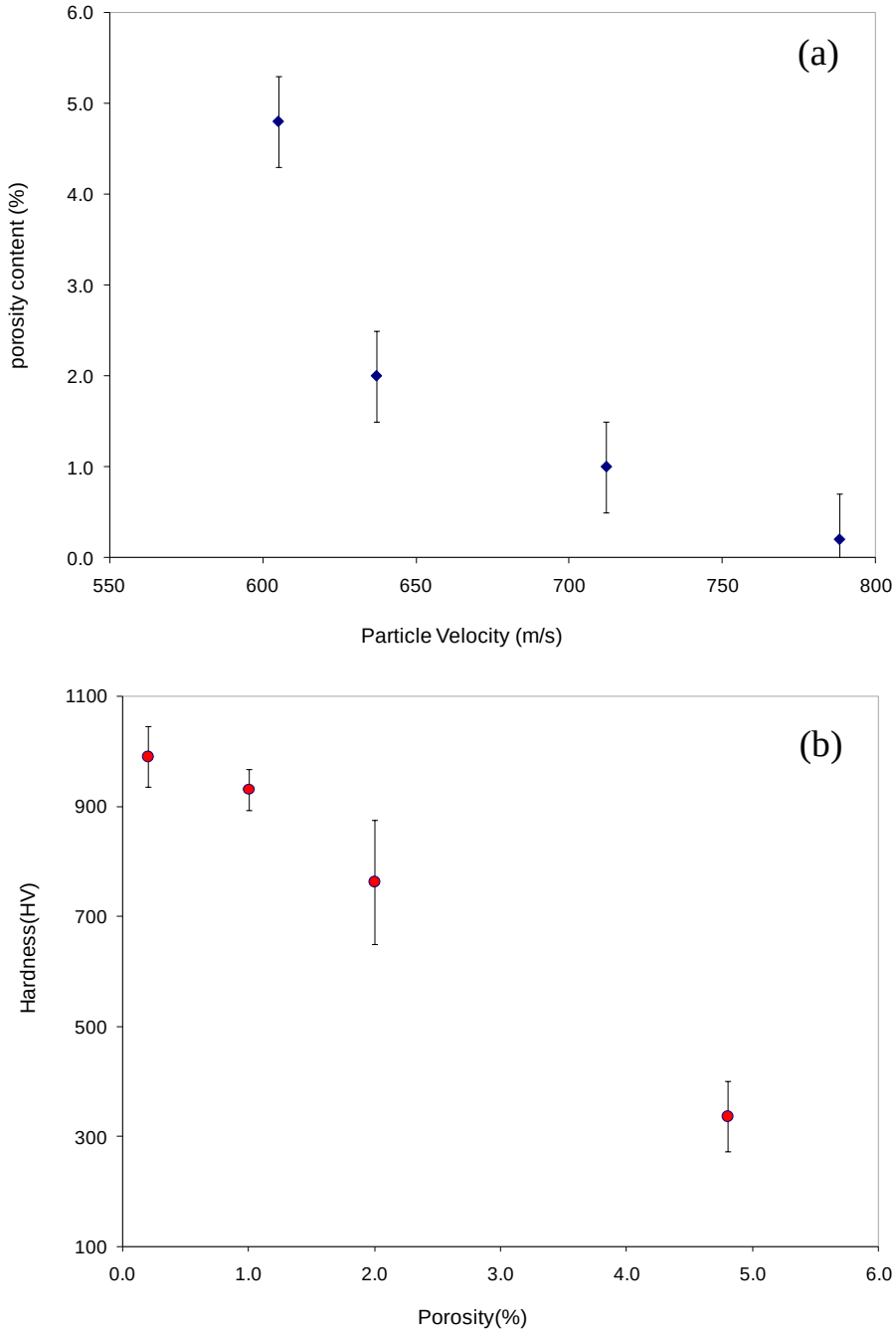

Figure 4-5 The variation of a) coating porosity vs. particle velocity and b) coating hardness vs. coating porosity

4.1.3. The Effect of Porosity on Thermal Diffusivity

Thermal diffusivities for a group of samples with different porosities were evaluated and the results are summarized in Figure **4-6**. A surface porosity of 0 to 8% in the crack-free

area, obtained in this experiment, has not altered the thermal diffusivity of the coating. The measured thermal diffusivities of the composite alumina-YSZ coatings are, however, comparable with those of the stabilized zirconia sprayed with the same process, which is 4.09E-7±1.5E-9 m^2/s. It is noteworthy that the thermal conductivity of the 8 wt% YSZ formed by this process with 2% porosity was measured as 1.04 W/m°C. This value is in turn comparable with the values reported in the literature [2] for air plasma sprayed YSZ (0.9~1 W/m°C) and YSZ deposited by EB-PVD (electron beam physical vapour deposition), which is in the order of 1.8~2 W/m°C [2].

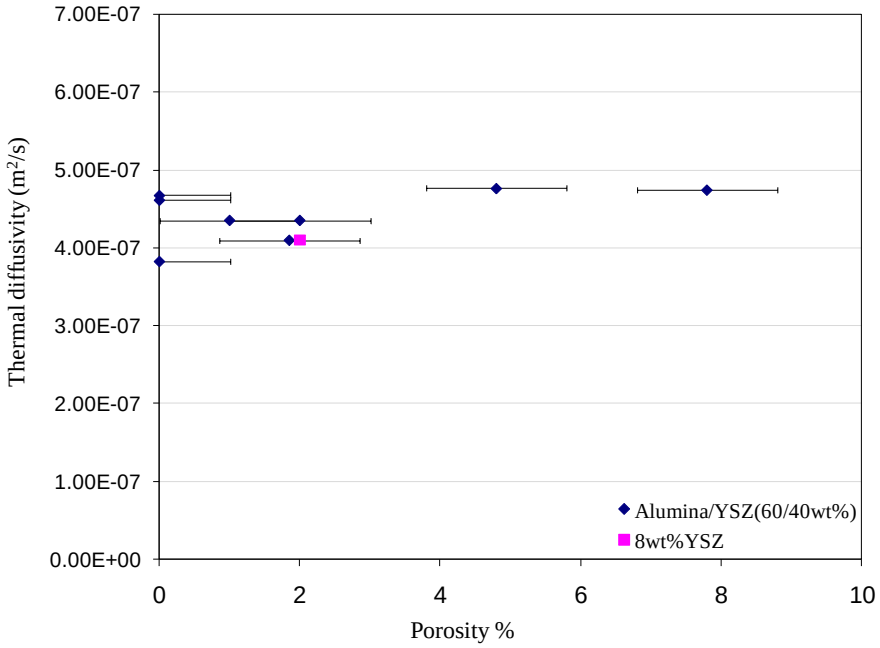

Figure 4-6 Thermal diffusivity versus porosity of the coatings

These results suggest that porosity may not be a very significant factor for thermal barrier application. Hence, implementation of a dense composite coating may be preferred to achieve better mechanical properties. It should be considered, in the thermal diffusivity versus porosity results, that the smaller pores of submicron sizes could not be detected in the image analysis method with 500X magnification. However, it is proven that the roles

of size, shape and densities of the intersplat pores on thermal diffusivity are more important than the total porosity content [111].

In conclusion, in this part of the study, the importance of key variables in suspension plasma spraying of multi-component alumina-YSZ coatings was evaluated. It was observed that the variables that directly affect the particle velocity and temperature were the most influential on the microstructure. Considering the greater significance of particle velocity in this regard, variables with more prominent effect on this parameter were of prime importance. On the other hand, the substrate roughness and robot speed do not play any role on neither T_p nor V_p, and consequently do not affect the coating microstructure.

It was experienced that for variations in particle velocity, the plasma torch parameters, e.g., total gas flow rate and plasma gas composition, were most important. On the other hand, particle temperature is more readily manipulated by feed parameters like solid content, particle size and feed rate.

Helium auxiliary gas was successfully used as a tool to achieve a wider microstructural variety in the SPS coatings. It especially helped to introduce higher porosity content in the coating. The porosity, however, increases at the expense of reducing the coating hardness. Thermal diffusivity in SPS coating for a multi-component system of 60 alumina / 40 YSZ is reasonably low and it does not change with up to 8% porosity.

4.2. Phase Formation and Transformations in SPS Coatings

This part of the study is to investigate how as-deposited coating structure, either crystalline or non-crystalline, can vary according to the spray conditions. For this purpose, the samples provided in section 4.1 were used. The initial powders as well as the

coating samples went through XRD and the coatings underwent DSC evaluations according to sections 2.5.2.1 and 2.5.2.2 for amorphous phase and crystalline phase analysis respectively.

Investigation of the XRD patterns from the powders used in this experiment shows that the zirconia powder consists of cubic structure and the alumina nano-powder contains both rhombohedral (i.e., α) and cubic (i.e., γ) structure. The ratio of α/γ, according to the supplier, is equal to 95/5 wt%, while the micron-size alumina powder shows only α structure. The loose nano- and/or micron-size powders were mixed and suspended in ethanol for injection into the plasma jet. The 13 wt% YSZ nano-powder was also deposited separately using the same process as a reference point and to investigate the preferred crystalline structure of the material in SPS process without the alumina addition. The sample preparation conditions are summarized in Table 4-2. In this table, also, the resulting plasma power and in-flight particle velocity and temperature are listed.

Table 4-2 Variables evaluated for the effect on phase formation

Sample number	Auxiliary gas	Solid content	Feed rate (kg/h)	Powder type	Power (kW)	V_p±20 (m/s)	T_p±50 (°C)
1	He	30%	1.8	Nano	57	592	2880
2	He	30%	1.8	Micron	57	605	2811
3	He	10%	1.8	Micron	57	654	2600
4	He	30%	1.3	Nano	56	638	3015
5	He	10%	1.3	Nano	82	650	3030
6	H_2	30%	1.3	Micron	84	730	2780
7	He	30%	1.3	Micron	81	788	2930
8	H_2	30%	1.3	Nano	118	810	3000
9	H_2	10%	1.3	Micron	117	814	2869
10	H_2	30%	1.8	Nano	118	815	2850
11	H_2	10%	1.8	Micron	116	840	2794
12	He	10%	1.3	Micron	80	770	3100
13	H_2	10%	1.3	Nano	85	730	2995
14	H_2	30%	1.8	Micron	85	712	2740
15	He	10%	1.8	Nano	82	790	3160
16	H_2	10%	1.8	Nano	85	718	2880

4.2.1. Crystalline/Amorphous Phases in As-Coated Structure

The as-deposited coatings present various structures as shown in Figure 4-7. Figure 4-7(a) represents the XRD pattern of the unmixed 13 wt% YSZ powder coating without alumina that shows a fully face centered cubic (FCC) structure. The investigation of the XRD patterns for composite coatings, as appearing in Figure 4-7(b) through (d), shows that stabilized zirconia has basically formed as FCC structure. The observed cubic zirconia structures best match with the pattern of ICSD database number 82-1246 with formula $Zr_{0.8}Y_{0.2}$ $O_{1.9}$. The symmetry system for this structure is (225) equivalent to Fm-3m (indicated as t" structure by the data base). A second pattern compatible with this XRD result was number 30-1468 with formula $Y_{0.15}Zr_{0.85}O_{1.93}$ and the same symmetry. This structure appears in both stabilized zirconia without alumina and in its composite with alumina.

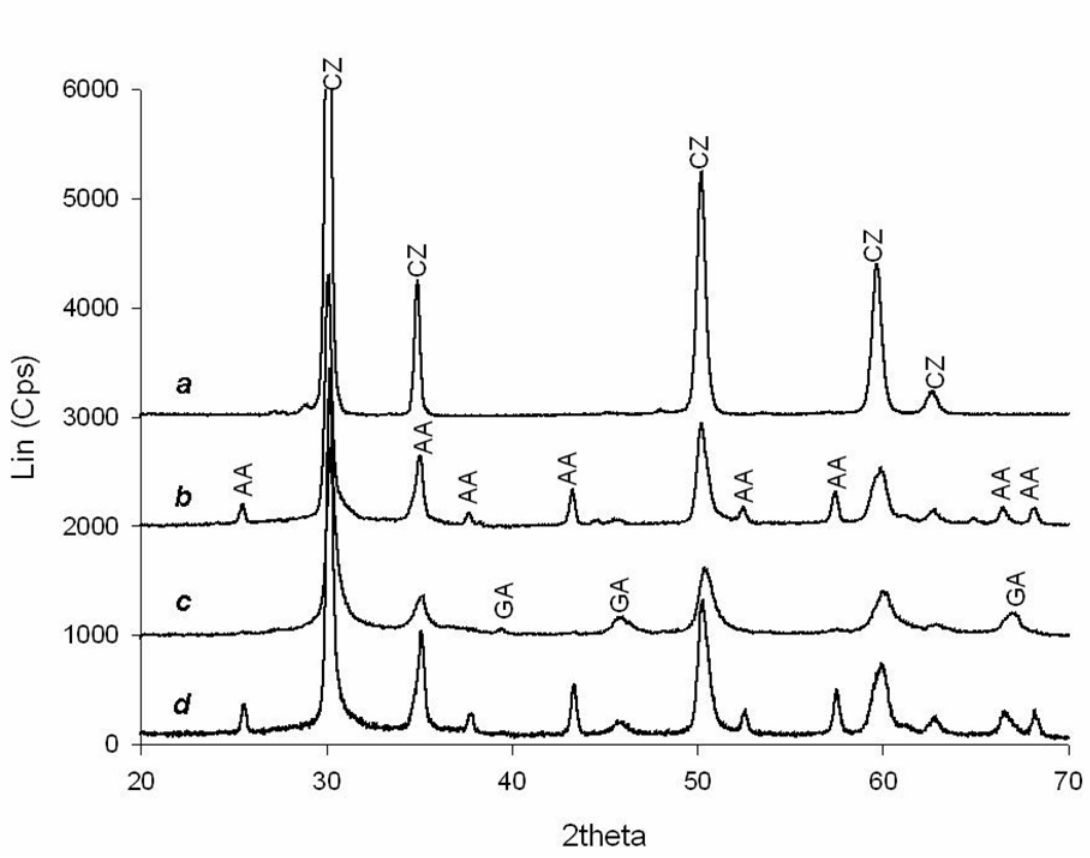

Figure 4-7 Typical XRD patterns from SPS deposition under various spray conditions showing cubic zirconia (CZ) in a) 8YSZ; b) in 60 Al_2O_3/40YSZ presenting cubic zirconia (CZ) and α-alumina (AA) as the major alumina phase; c) in 60 Al_2O_3/40YSZ showing cubic zirconia (CZ) and γ-alumina (GA) as the major alumina phase, and d) in 60 Al_2O_3/40YSZ showing mixture of both GA and AA alumina in addition to cubic zirconia.

The difference between the cubic and t" zirconia is in the oxygen anion displacements within the structure [1]. Thus, in t" structure there is a slight displacement from tetrahedral interstitial positions for oxygen atoms as compared with the so-called "cubic structure". In a group of the samples, however, slight splitting of the peaks at about 59-60° that are related to the planes (103) and (211) of tetragonal structure, as in Figure 4-8, proves the presence of some tetragonal YSZ phase. This structure is compatible with ICSD database number 82-1242 with formula $Zr_{0.88}Y_{0.12}O_{1.94}$. In general, the dominant structure for zirconia in this experiment is mainly cubic (or t") structure.

Since differentiation between the cubic and tetragonal zirconia is more difficult than differentiation between the phases of alumina, the resulting coating structures were categorized based on the alumina phases. Figure 4-7(b), (c) and (d) represents the typical structures of the coatings in which the alumina appears in mainly cubic γ, mainly hexagonal α or mixed (γ+α) structures, respectively.

It was noticed that the samples with mainly α-alumina structure (samples number 1 to 5 in Table 4-2) and XRD pattern similar to Figure 4-7(b) were normally deposited using helium auxiliary gas. The α-alumina with rhombohedral (hexagonal) structure is known as corundum. This structure is identified in the database by ICSD number 71-1123, formula Al_2O_3 and symmetry system (167) equivalent to R-3c. According to Table 4-2, this group of samples is produced at low plasma powers of about 56-57 kW.

On the other hand, Figure 4-7(c) represents the second group of crystal structures, consisting of cubic YSZ and γ-alumina. It can be seen that in most cases (samples 6 and 8 to 12 in Table 4-2); application of hydrogen auxiliary gas ensures the formation of γ-alumina phase with FCC structure. This structure matches with ICSD database number 75-0921, formula $(Al_2O_3)_{1.33}$ and symmetry system (225) equivalent to Fm-3m. It can also be noticed, based on Table 4-2, that the majority of these samples are produced at high plasma powers (116-118 kW).

As a result, among the variables in this experiment, plasma auxiliary gas seems to be of major influence on the phase formation in as-deposited coatings. It is worth recalling that plasma auxiliary gas was recognized as the most important variable on the particle velocity as found in section 4.1. In that section the dependency of the velocity on the

plasma power was also proven. Therefore, these results suggest the study of the coating's crystalline phases in relation with the particle state.

The relationship between the particle temperature and velocity with the resulting crystalline phases is illustrated in Figure 4-9. In this figure, the coatings with mainly γ-alumina are shown as round symbols and the square points are representative of the coatings with mainly α-alumina. It is evident that at lower particle velocities (i.e., below 650 m/s), α-alumina was formed, while at higher velocities (i.e., above 730 m/s) the dominant phase is γ-alumina. As a guide for the eye, two lines are drawn in Figure 4-9 to show the trend of the structural changes according to the velocity. To explain this observation, the microstructures resulting from these two particle velocity ranges have been compared and will be discussed here.

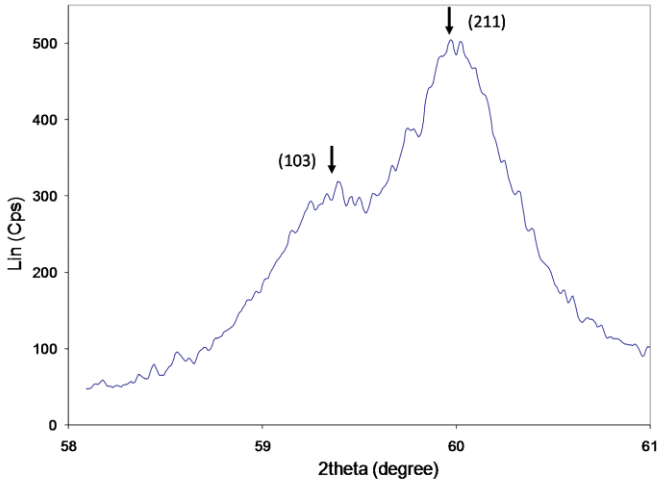

Figure 4-8 Peak splitting as an indication of tetragonal zirconia phase formation and the planes of each peak

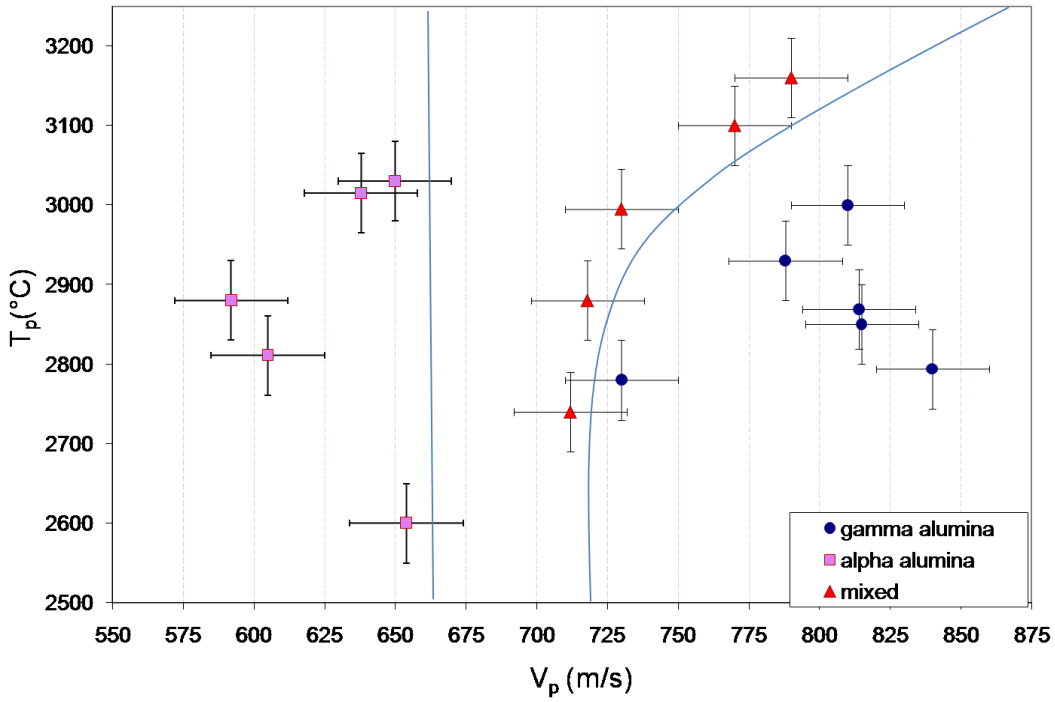

Figure 4-9 Alumina component phase formation behaviour within the as-deposited composite versus in-flight particle state

Typical SEM microstructures of the coatings at high and low particle velocities are shown in Figure 4-10. It is apparent in Figure 4-10(a) that higher velocities (about 810 m/s) have caused wider splat spreading than the particles with lower velocity (about 600 m/s) shown in Figure 4-10(b). This is expected because the particles with higher velocities flatten faster [112], therefore the flattening process happens before the start of solidification [113] and the crystalline phase formation. Thin splats with large effective contact area in the intersplat and substrate interfaces are of great importance on phase formation within the coating. It has been reported that the thermal contact resistance and splat thickness strongly affect the cooling rate [83]. A thin splat with large contact area can provide rapid heat dissipation and large cooling rates. Larger cooling rates are shown to be in favour of formation of metastable phases like γ-alumina [75,83]. This explanation for alumina can be generalized to zirconia splats. This means that a more stable tetragonal

phase can appear in the coatings due to lower particle velocities (lower cooling rates), while the cubic phase can form at higher velocities (larger cooling rates) [105].

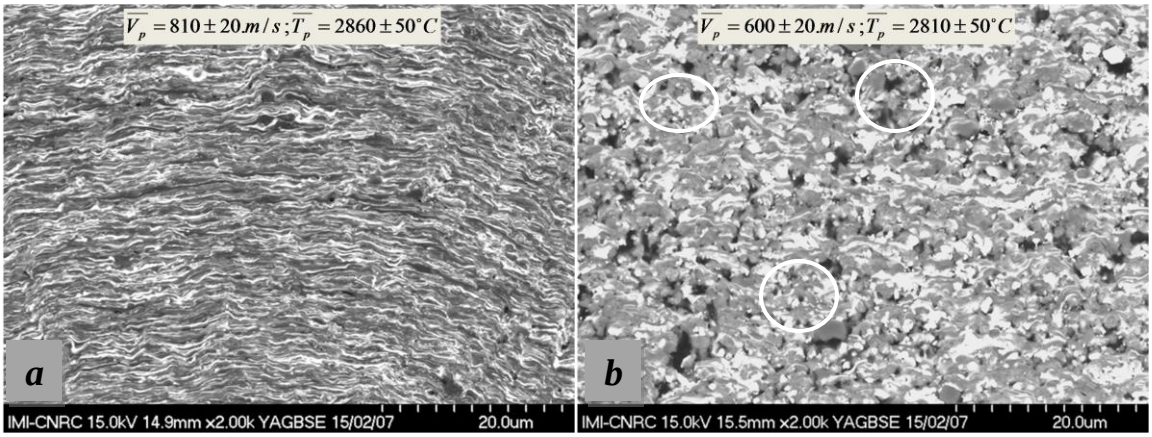

Figure 4-10 SEM micrographs of the coatings deposited using a) H_2 gas with high particle velocities and b) Helium auxiliary gas with lower particle velocities resulting in different splat flattening and intersplat contact area (circles show some of the in-flight solidified particles within the coating)

Additionally, the role of unmolten or semi-molten nano-particles entrapped in the molten particles should not be ignored. Some of the areas containing such particles are circled in Figure 4-10(b) in the coating of the low-velocity particles. Figure 4-11 presents a large in-flight solidified particle within the coating illustrating such entrapment. The clearly round edges of the particle show that it has encountered melting and in-flight solidification. However, the internal particles indicated by the arrow in this figure have remained unmolten. These particles at low velocities, when the in-flight solidification happens, can play a pronounced role on the resulting crystalline structure. They act as the nucleation sites for the solidifying melt, so that the resultant follows the structure of these solid particles. The in-flight solidification in low-velocity particles can happen due to their inability to penetrate into the stagnating gas adjacent to the substrate. This resistance from the stagnating gas makes these particles deflect toward an off-normal path and delay their deposition, as well as preventing their effective impact on the surface [114].

Therefore in a microstructure with a high number of in-flight solidified particles, as in Figure 4-10(b), there are more chances for the formation of the initial crystalline structure of the feed powder (i.e., in this case α-alumina). This fact causes more complications in prediction of the deposited coating according to the previously discussed in-flight particle state and spray condition.

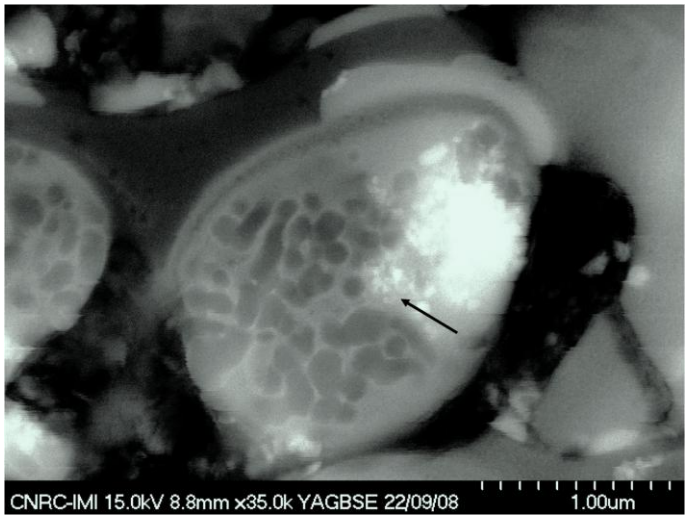

Figure 4-11 Entrapped unmolten nano-particles inside the large in-flight solidified particle in the coating

Intermediate velocities, shown by triangles in Figure 4-9, present a mixed structure of (γ + α)-alumina in addition to cubic zirconia along with different amounts of tetragonal zirconia. This kind of structure can be seen in the XRD pattern of Figure 4-7(d). Figure 4-12 indicates the relationship between the content of γ-alumina compared with the cubic zirconia in the coating. This figure suggests a dependency between the present phases in the coating, indicating that the percentage of the cubic zirconia increases with increasing the γ-alumina content. This predicts that "metastable" γ-alumina coincides with "metastable" cubic zirconia formation. Thus the favourable conditions discussed for the

alumina phases may be extended to the zirconia, as well. This means that the metastable cubic phases are expected at higher particle velocity (i.e., larger cooling rate).

To investigate the importance of other variables, it should be noted that the particle temperature is mainly dependent on feed parameters such as feed rate and solid content. Therefore, these parameters can affect the structure through changing the particle temperature. Considering the small size associated with the particles in the SPS process, a comparatively uniform temperature throughout the particle is expected. The in-flight particle temperatures (Figure 4-9) are high enough for complete melting of both components (usually more than 2730°C) and do not seem to play any major role in phase formation within the coating. The exception is that for very high particle temperatures (i.e., beyond 3000°C, as in the last two points of the mixed structures in Figure 4-9); this appears to result in formation of some α-alumina phase at high velocities where domination of γ-phase is expected. The reason can be the impingement of overheated particles on the substrate that contributes to excessive heating of the coating and consequently the formation of α-alumina phase due to deposition on hot substrate [75]. In addition, reheating the coating by the following deposition passes of the hot particles could have caused more phase transformation of metastable γ to α –alumina due to heating to this transformation temperature.

Although changing other variables such as particle temperature and powder size do not seem to change the type of the phases present in the coating, they may change the relative amounts of these phases. The role of these parameters can be investigated by focusing on the coatings with mixed (γ+α)-alumina structure and the relative amount of the metastable or stable phases.

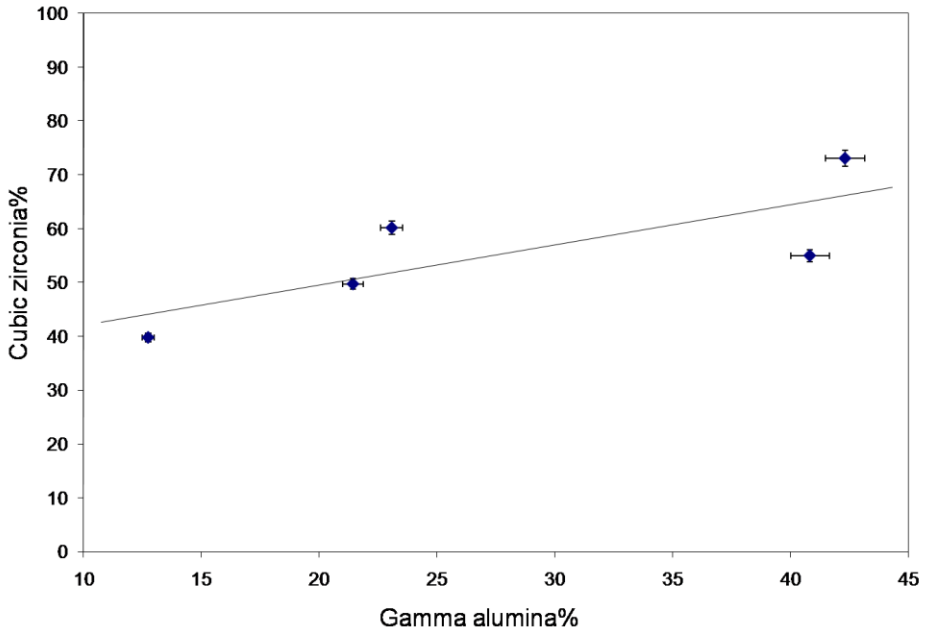

Figure 4-12 Correlation between the γ percentage in alumina and the cubic phase percentage in zirconia

Figure 4-13 shows the relationship between the amount of γ-alumina and the particle velocity in the samples with mixed structure. In this figure, the points are indicated by the sample numbers, which correspond with those in Table 4-2. To facilitate the comparison, the particle temperature and the feed size range are included. Comparing samples 13, 14 and 16 (left side) with samples 12 and 15 (right side) in Figure 4-13, verifies the effect of high temperature on phase formation. This comparison shows that very high particle temperatures in samples 12 and 15, in spite of high particle velocities, have resulted in almost equal or smaller amounts of γ-phase compared with the coatings formed by lower velocity particles. This is against what was expected that is higher particle velocities should result in larger amounts of metastable γ-alumina. This observation confirms the previously stated role of very high particle temperatures in enhancement of more stable phases like α-alumina.

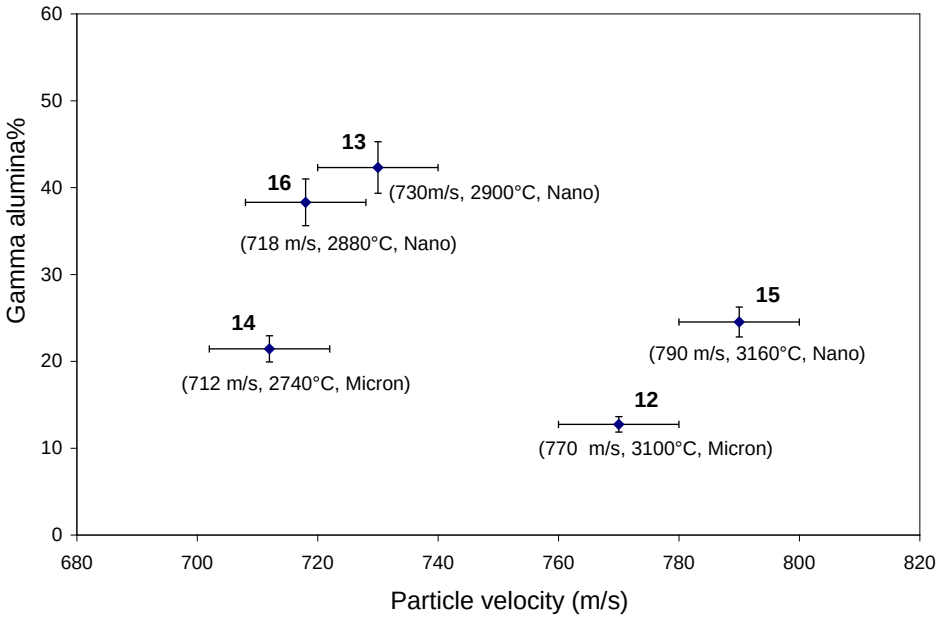

Figure 4-13 The γ-alumina phase content versus particle velocity in the samples with mixed structure showing the role of particle temperature and feed size range

On the other hand, the minimum amounts of γ-alumina phase are observed in samples 12 and 14, the coatings from the micron-size powders. In addition, larger amounts of γ-alumina have been observed in samples 13, 15 and 16, which are produced by the nano-powder feed material. The larger particle size forms thicker splats that decrease the cooling rate and facilitate the formation of more stable phases like α-alumina.

Investigation of phase changes during heating was done on a group of samples provided for this purpose. These samples, produced under various conditions, contained a range of amounts of amorphous phase and a variety of crystalline structures.

Another noticeable feature observed in the XRD patterns of the coatings is the presence of some background humps indicative of the formation of amorphous phase. They appear along with wide crystalline peaks that show the very small or nano-crystalline grains. The

presence of the amorphous phases was also confirmed by DSC test results, as will be discussed in the next section.

4.2.2. Phase Transformation during Thermal Analysis

Typical DSC curves of the alumina-YSZ coatings, as shown in Figure 4-14, basically consist of three major peaks. The wide peak between 200 to 800°C may be considered as the relaxation area that is characteristic of the structures containing an amorphous phase [115]. This relaxation involves changes in some physical properties by reduction of vacancy concentration to the equilibrium value that during rapid solidification was not possible. This reaction is irreversible when a glass is annealed to its glass transition temperature. Thus the cooling curve in Figure 4-14 does not show the peak of the reverse process.

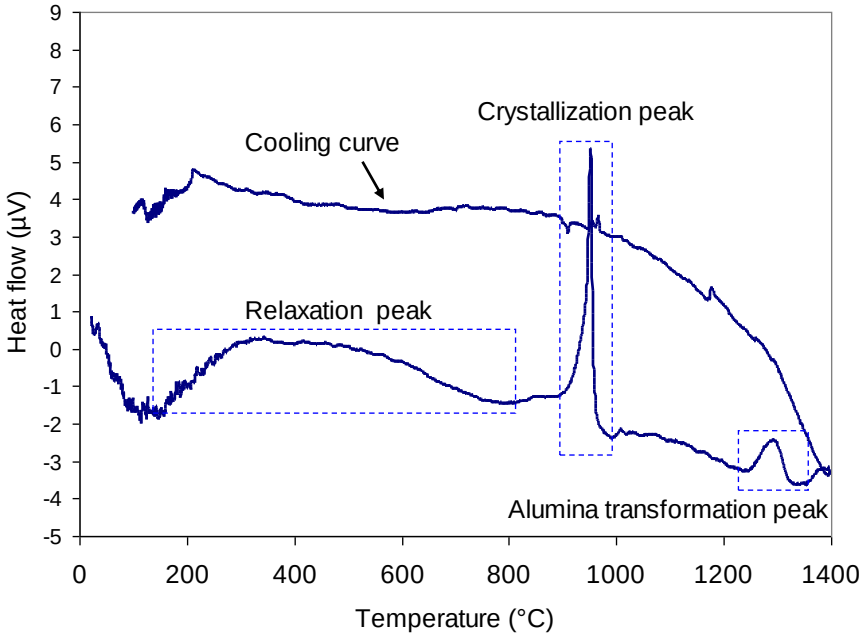

Figure 4-14 Heating and cooling DSC curves of a typical SPS coating showing three different peaks probable in heating process of 60 Al_2O_3/40YSZ SPS coating

However, since these peaks were sometimes observed in almost fully crystalline samples, it is expected that some additional effects are contributing to this phenomenon. For instance, there may have been some relieving of thermal residual stresses and/or reorientation of the crystalline planes to eliminate the texture.

The second peak is sharp and related to crystallization phenomenon that is expected to happen simultaneously from amorphous into alumina and zirconia crystals at about 950°C [24]. The third peak is anticipated to represent γ- to α-alumina phase transformation, which takes place at around 1200°C [44]. The peak identifications can be verified by studying the heat-treated samples at 700, 1000 and 1200°C, as will be explained further in this work.

4.2.3. Transformation Verification by Heat Treatment

Heat-treated samples at 700°C for 12 hours show the same XRD patterns as the initial coating. Besides, the pattern does not show any peak shift or change in grain size, according to XRD evaluation. This suggests that for such samples the relaxation phenomenon in the DSC curve of Figure 4-14 does not involve any crystallographic phase transformation or thermal residual stress relief.

It was noticed that for most of the heat-treated coatings, even at higher temperatures, peak shifting did not happen. This suggests the low level of the residual stresses in these samples. This stress in the coatings with the microstructure as in Figure 4-10(a) should have been released by extensive cracking [72]. On the other hand, the microstructures such as that in Figure 4-10(b), with comparatively loose and small splats, do not

accumulate any considerable residual stresses. Therefore, these SPS coatings which are formed of smaller in-flight particles than the conventional plasma spray process (as will be explained in section 5.3) do not involve any large accumulated residual stresses.

Heat treatment at 1000°C for 1 hour has been carried out to investigate the crystallization phenomenon noticed in the DSC spectra. The XRD pattern of the heat-treated sample was similar to that in Figure 4-15(a), consisting of cubic zirconia and γ-alumina. In addition, background humps of some amorphous phases were observed. Following the heat treatment at 1000°C for 1 hour, the amorphous humps were largely reduced; meanwhile the coating showed wider peaks that were more obvious in the peaks of γ-alumina phase as shown in Figure 4-15(b). Since the primary alumina structure formed from the amorphous phase is expected to be γ-alumina [116], wider peaks indicate smaller average grain size as a result of crystallization of amorphous phase into nano-crystalline structure. The quantitative investigation of the grain sizes according to the amorphous phase content will be presented in section 6.4.

Heat treatment at 1200°C for 24 hours (on the detached samples from the substrate) results in the appearance of α-alumina at the expense of diminishing the γ-alumina peaks. This observation supports the proposed identity for the related peak that takes place within the range of 1200 to 1400 ºC in the DSC spectrum of Figure 4-14. In contrast, in the coatings with mainly α-alumina in the as-deposited condition, this heat treatment did not result in any changes in the crystalline phases.

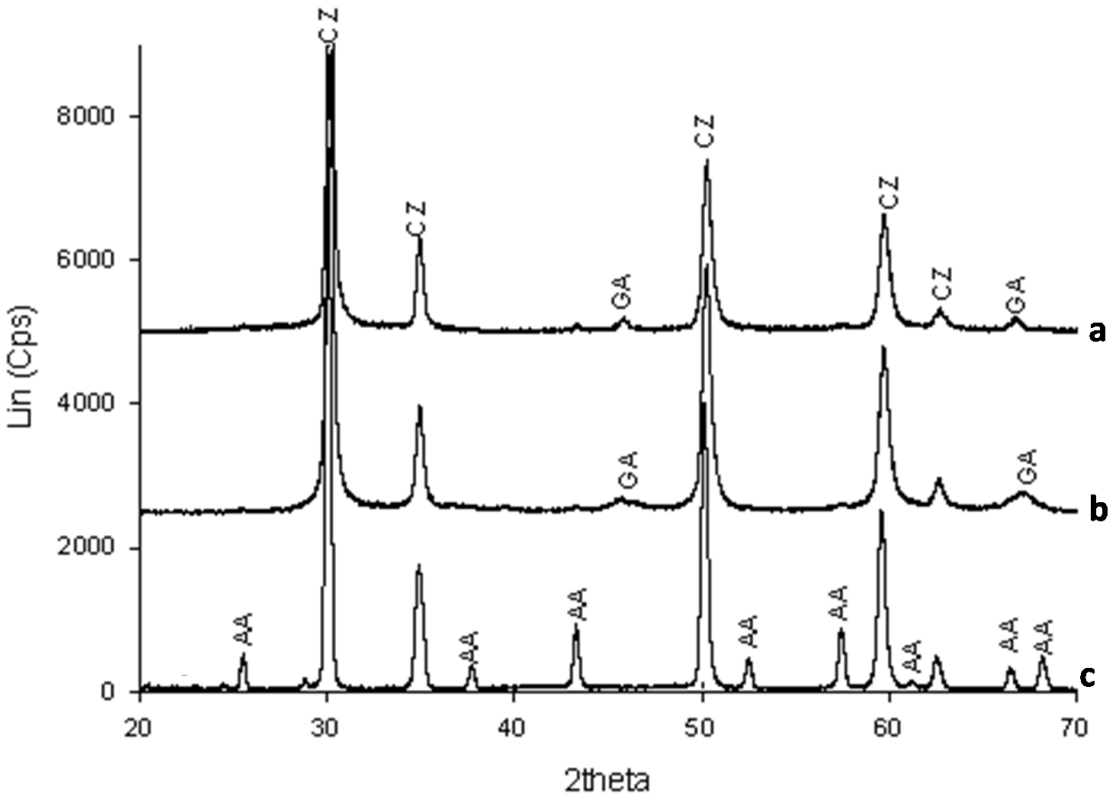

Figure 4-15 The effect of heat treatment on a) as-sprayed alumina-YSZ coating, b) heat-treated coating at 1000°C/1 hr, c) heat-treated at 1200°C/24 hrs

The structures of different samples after 1500°C heat treatment for 5 hours are similar and consist of α-alumina and cubic zirconia. Although, sometimes the tetragonal zirconia phase is found in the samples, when pre-existing tetragonal phase was present before heat treatment, cubic zirconia phase was mostly retained and no traces of monoclinic zirconia could be found in any of the heat-treated samples. Conversely, based on the reports in ZrO_2-8 wt%Y_2O_3 coating, at 1000°C the depletion of zirconia unit cells from yttria started and at 1400°C after 24 hours about 35% monoclinic zirconia was formed [117]. This indicates the considerable stability of this composite compared with the conventional YSZ and its ability to prevent the transformation to monoclinic zirconia which is a major concern in TBCs performance.

4.2.4. Preferred Phase during Crystallization of the Amorphous Phase

To investigate the preferred structure during crystallization of the amorphous phases upon heating, the transformation peak areas in DSC curves were used. This helped to obtain the relative amount of each specific phase undergoing the transformation. A larger peak area indicates a higher amount of the phase undergoing the corresponding transformation. Therefore, the larger crystallization peak area stands for higher amorphous content and the larger γ- to α-alumina phase transformation peak represents the larger amount of the γ-phase. The γ-phase can form during the deposition process and/or as a result of crystallization of alumina out of amorphous phase during heating the DSC sample.

Figure 4-16 is a summary of the relation between transformation peak for γ- to α-alumina and the crystallization peak that represents the amorphous content in the coating. In these coatings, the alumina in as-deposited condition has either γ- or α-structure, or a mixture of both phases. This figure shows that when the as-sprayed structure contains mainly γ-alumina, there is a steep linear relationship between the crystallization peak (the amorphous content) and the γ to α transformation peak (that represents the amount of γ alumina after crystallization process). This clearly indicates that increasing the amorphous content increases the amount of transformable γ- to α-phase.

Conversely, when the as-deposited alumina is of mainly α-structure, even at larger amorphous contents, the transformation peak from γ to α is not increasing. To the contrary, it is normally almost equal to that of the crystalline samples with no amorphous phase (indicated as point A in Figure 4-16 where the crystallization peak area is almost

zero). This shows that in such coatings the alumina in the amorphous phase has a lower tendency for crystallization into γ-phase; it prefers to nucleate on the pre-existing α-phase, so that the amount of γ-phase and consequently the γ to α transformation peak does not change with the amorphous content. In these coatings, the tendency for crystallization on pre-existing α-structure can sometimes prohibit any transformation into the γ-phase, as can be seen in the sample indicated by point B in Figure 4-16. Point B represents a coating with very large crystallization peak (amorphous content) in which the α-phase is the predominant structure for the alumina. In this sample, the γ to α transformation peak is zero; this means that during crystallization of the amorphous phase, no γ-alumina could have formed.

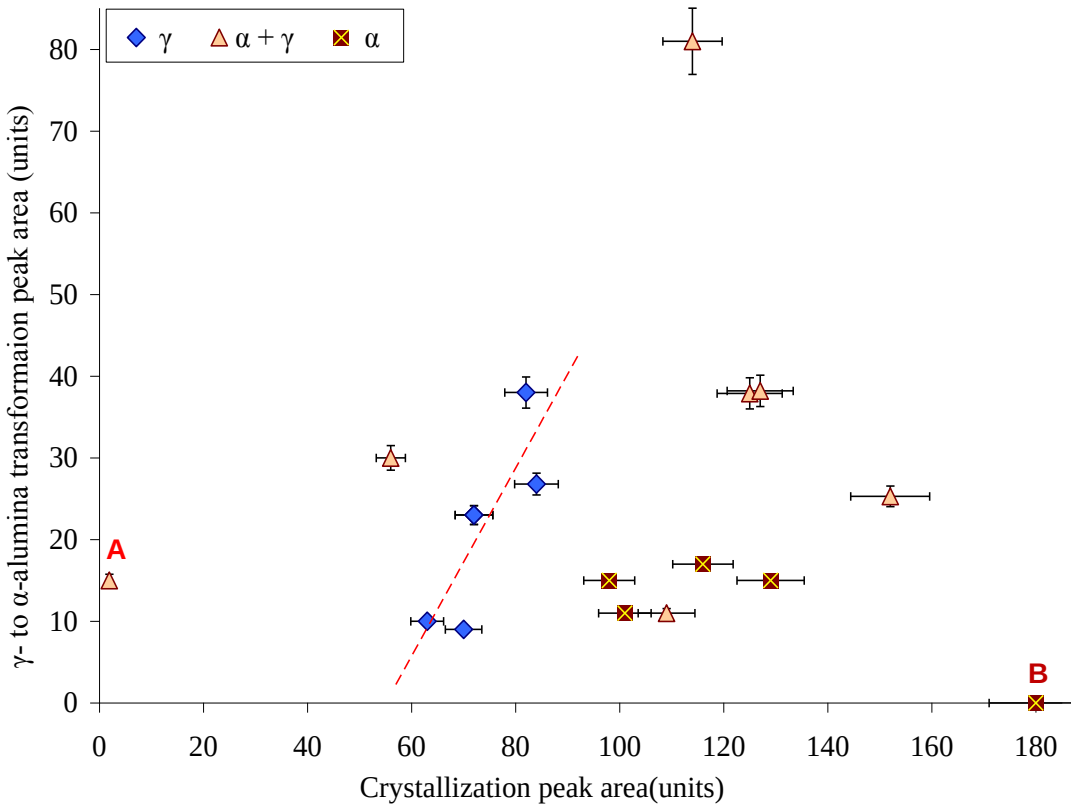

Figure 4-16 γ- to α-alumina transformation peak area vs. crystallization peak area in the coatings with the major crystalline alumina phase of γ, α or mixed structure

These observations suggest that the preferred phase during crystallization of the amorphous phase is dependent on the initial crystalline structure, which acts as the nucleation site. Thus, in the coatings with mixed structure a compromise between the amounts of the two structures (α- and γ-alumina) in the as-deposited coating is expected to determine the proportion of the resulting phases after the crystallization process.

The stabilized zirconia after crystallization did not go through any phase transformation. Thus, this sort of evaluation for the zirconia component was not possible. However, the XRD pattern of the heat-treated sample, as will be discussed later, shows that the resulting structure after crystallization is not different from the crystalline YSZ initially present in the as-deposited coating.

Another noticeable observation in Figure 4-16 is that the coatings with mainly α-alumina structure show a high amount of amorphous phase. The reason for this concurrence must be due to the lower particle velocity that was found here to favour the formation of α-alumina. The lower particle velocity results in longer dwelling time at high temperature, which in turn could provide the possibility for better mixing. The amorphous formation in a multi-component system is influenced by the ratio of dissolution of the components. On the other hand, alumina and YSZ are almost immiscible in solid state and can mix only after melting. As a result, the lower particle velocity that causes a longer time at high temperature leads to the ideal conditions for melting and mixing of the components simultaneously. This issue will be investigated further in sections Chapter 5.

Briefly, it was explained in this section that the particle velocity is a crucial parameter which can dictate the crystalline structure of the resulting coatings. Particle velocity can be controlled by plasma parameters such as plasma gas type and plasma condition that in turn determine the plasma power. However, particle temperature, as long as it is high enough for complete melting of the particles, does not play an explicit role in the type of phases present. It, however, can affect the phase ratios, when raised far beyond the melting points of the components. Feed size also can affect the phase ratios, so that the larger particles result in formation of more stable phases in the coating. Other feed parameters including feed rate and solid content influence the results through variation of the particle temperature. The presence of unmolten nano particles increases the intricacy of phase prediction in the as-deposited coating.

In addition, it was found that thermal evolution of the combined crystalline/amorphous structure results in crystallization of the amorphous phases, as dictated by the pre-existing crystalline phases in the as-deposited coatings. Thus the in-flight particle velocity can also play a significant role on the final coating structure after crystallization, as it determines the initial phases in the as-deposited state.

Heat treatment at the alumina transformation temperature (1200°C for 24 hours) leads to a coating composed of mainly α-alumina in addition to the cubic zirconia. Upon heat treatment at about crystallization temperature, the amorphous structure seems to form smaller crystalline nano-grains than what could be produced during plasma spray deposition. This is investigated more in section 6.4.

A somewhat surprising observation in this section was that samples with mainly α-alumina phase (that form at lower cooling rates) are coincident with higher amorphous phase (which is the preferred state at high cooling rates). To explain this, a more detailed investigation of amorphous phase formation seemed necessary, and will follow in Chapter 5.

4.3. Summary

Microstructural studies of the SPS coatings showed that the spray parameters can be related to the resulting microstructures, mainly through their effect on in-flight particle characteristics (T_p, V_p). The more prominent parameter is V_p, whereas T_p does not play a very significant role. Therefore, spray parameters ruling V_p are the ones that are most suitable for microstructural control. Some of these parameters are plasma gas composition, total plasma gas pressure and/or plasma power.

In addition, while working with alumina-YSZ composite, it was observed that porosity, as a major microstructural characteristic, may affect the mechanical properties (e.g., increasing hardness in the coating with decreasing porosity). Nonetheless, its role on thermal diffusivity (up to 8% porosity) is not significant. The material also showed about the same thermal diffusivity as YSZ at all porosity contents. Thus this composite may be used even at very high density as a TBC without concern for reduced thermal resistance. In addition, SPS process has the ability to produce extremely high-density coatings with near-zero porosity, as well as porous structures if required.

Investigation of phase analysis in the as-deposited SPS coatings revealed that particle velocity plays a crucial role on the type of the resulting crystalline phases, as it did on the microstructure. Higher particle velocity increased the formation of metastable phases

(such as γ-alumina and cubic zirconia). In contrast, particle temperature only affected the phase ratios and not their type. Very high particle temperatures caused the formation of less metastable phases. Upon heating to crystallization temperature, the amorphous portion of the coating transforms into crystalline phases that are dictated by pre-existing crystals in the as-deposited coating. This means that the main part of the amorphous phase will crystallize into structures which were already present in the crystalline state.

Chapter 5 Developing Amorphous Phase in the Coatings

This part of the study aims at finding the ways that the amount of the amorphous phase can be varied within the alumina-YSZ composite coatings using SPS process. For this purpose, a group of most probably effective variables were selected. These variables are the in-flight particle velocity and temperature, feed powder size, substrate preheating, travel speed of the spray robot, and bond coat (presence and absence). These parameters seemed to be influential on the amorphous content, based on the process nature and the pre-assessment of the variables. In this work, the samples from three sets of experiments were used. The coatings were deposited on small mild steel coupon substrates of (2.5×2.5 cm^2 with 0.05 cm thickness). Details of the material and sample preparation in the three sets of samples are summarized in Table **5-1**.

Set1

This set of samples was to compare the different feed particle sizes and to find the role of the spray robot speed on the amount of amorphous phase in the coating. In addition, the coatings prepared for evaluation of the role of particle velocity were mostly selected from this group, as will be explained later.

Powders used in this part were a mixture of micron-size powders, 13 wt% YSZ (Unitec Ceramics, Stanford, England) nominal size 1 μm, combined with the proportional amount of 5 wt% YSZ (Tosoh TZ-3YS, Tokyo, Japan) to produce 8 wt% YSZ and mixed with alumina powder (Malakoff, TX, USA) nominal size 1.4 μm in a weight ratio of 60

alumina / 40 YSZ. The resulting mixed powder size range was about 1 to 2 μm. This mixture was next suspended in ethanol with a solid weight of 30%. Another suspension with the same solid content was prepared using the nano-size powders, 13 wt% YSZ (Inframat, Farmington, CT, USA) with proportional weight of 5 wt% YSZ to produce 8 wt% YSZ and alumina nano-powder (Nanostructured & Amorphous Materials, Houston, TX, USA) with the same alumina-to-YSZ ratio. The nano-powder mixture size was 20-60 nm. As the dispersing material, polyethylen-eimine (PEI) (MW 25,000 Alfa Aesar, Ward Hill, MA, USA) and Nitric acid both with 10% concentration were used. Suspensions were lightly ball milled for more than 24 hours at 120 rpm roll to avoid large aggregate sizes.

The amorphous contents were measured alternatively with XRD and DSC evaluations for the coatings from the two types of suspension, "Nano" and "Micron." In addition, the in-flight particles were collected after spraying under similar conditions into a large water pot. The powders were next air dried and their micrographic pictures were provided using high-resolution FE-SEM technique. Sample preparation conditions for this group are listed in Table **5-1** with numbers 1 to 6.

Set2

The second set of samples with production conditions listed in Table **5-1** as numbers 7 to 10 was to evaluate the role of preheating and of particle temperature on amorphous content. The samples were in couples, where one was preheated with laser flash to an initial temperature of 350°C and the other was at room temperature when deposition started. Three different spray conditions were used to produce different particle temperatures.

Table 5-1 Spray conditions for producing the comparison samples and the resulting amorphous measurement results

Sample #	Total gas (slm), $Ar/N_2/H_2$(slm), current (A)	Robot speed (m/s)	Particle size range	T_p±50 (°C)	V_p±20 (m/s)	Preheat (°C)	Coating thickness (µm) / passes	DSC crystallization peak area ± 5% (arbitrary unit)	XRD ± 2% vol%
1	275, 65/15/20, 200	1	Nano	2783	748	-	540/70	**125**	**40%**
2	275, 65/15/20, 200	1	Micron	2831	750	-	760/70	**132**	**45%**
3	275, 65/15/20, 200	2	Nano	2755	758	-	410/70	**127**	**41%**
4	275, 65/15/20, 200	2	Micron	2783	748	-	520/70	**152**	**64%**
5	245, 75/10/15, 240	1	Micron	2810	702	-	620/70	**139**	**43%**
6	245, 75/10/15, 240	2	Micron	2822	670	-	350/70	**127**	**62%**
7	275, 65/15/20, 200	2	Nano	3064	684	350	340/50	**129**	**44%**
8	275, 65/15/20, 200	2	Nano	3064	684	No	330/50	**101**	**41%**
9	180, 45/45/10, 190	2	Nano	2830	525	350	320/50	**-**	**57%**
10	180, 45/45/10, 190	2	Nano	2830	525	No	320/50	**-**	**48%**
11	245, 75/10/15, 200	2	Nano	3430	558	350	300/50	**-**	**39%**
12	245, 75/10/15, 200	2	Nano	3430	558	No	340/50	**-**	**32%**
13	275, 65/15/20, 200	2	Micron	2750	751	-	350/150	**116**	**45%**
14	275, 65/15/20, 200	2	Micron	2733	748	-	220/100	**138**	**55%**
15	275, 65/15/20, 200	2	Micron	2730	754	-	90/50	**98**	**40%**

Set3

A third set of coatings that include the rest of the samples in Table **5-1** (samples number 11 to 15) were deposited to study the role of coating thickness with a larger number of deposition passes. To study the role of bond coat on the resulting coatings, two kinds of substrates were prepared. One substrate was bare mild steel blasted with #54 alumina grids and with a roughness of about 3 µm. The other was steel substrate bond coated with NiCrAlY using HVOF process resulting in a roughness of 4 µm.

Three couples of samples with and without bond coat were coated under the same spray conditions with 50, 100 and 150 passes of alumina-YSZ composite resulting in 90, 220 and 350 μm thickness, respectively. The samples were XRD tested, and the coatings without bond coat were studied by DSC, as well. The feed in all sets was axially injected with a 1.8 kg/h flow rate from a 3/8" (9.5 mm) plasma nozzle size, and the spray distance for all samples was 50 mm.

To evaluate the role of each parameter, up to three couples from the above list of samples were compared. The amorphous phase was measured using both XRD method as in section 2.5.2.2 and DSC method according to section 2.5.2.1. The average values for crystallite or grain size were evaluated using XRD peaks as detailed in section 2.5.3.

5.1. Role of Parameters on Amorphous phase Formation

The results of the XRD pattern calculations for volume percentage of the amorphous phase and DSC crystallization peak measurement are summarized in the last two columns of Table **5-1**. Comparing these results in the samples introduced in Table 5-2 presents the role of the corresponding parameter that differs between the two samples of a couple.

Table 5-2 The importance of each parameter on the amorphous phase formation within the alumina-YSZ composite coating using SPS

Parameters	Larger powder feed size		Higher robot speed		Higher particle velocity		Higher particle temperature		Substrate preheating			Higher number of deposition passes	
Comparison samples	(1,2)	(3,4)	(1,3)	(2,4)	(2,5)	(4,6)	(8,10)	(10,12)	(7,8)	(9,10)	(11,12)	(13,14)	(13,15)
Change in DSC measures	6%	20%	2%	15%	-5%	-20%	-	-	28%	-	-	-19%	18%
Change in XRD measures	13%	56%	0%	42%	-5%	-3%	-27%	-33%	7%	10%	22%	-22%	13%

A. Feed Particle Size

The micrographs of the dried micron- and nano-powder suspensions were as in Figure 5-1(a) and (b). They illustrate the aggregates of the micron- and nano-powders in their suspensions, respectively. It is evident, in this figure, that the aggregates of nano-powder are larger than those of micron-powder. These aggregates mostly consist of particulates of the same material (either alumina or YSZ) rather than mixed alumina-YSZ.

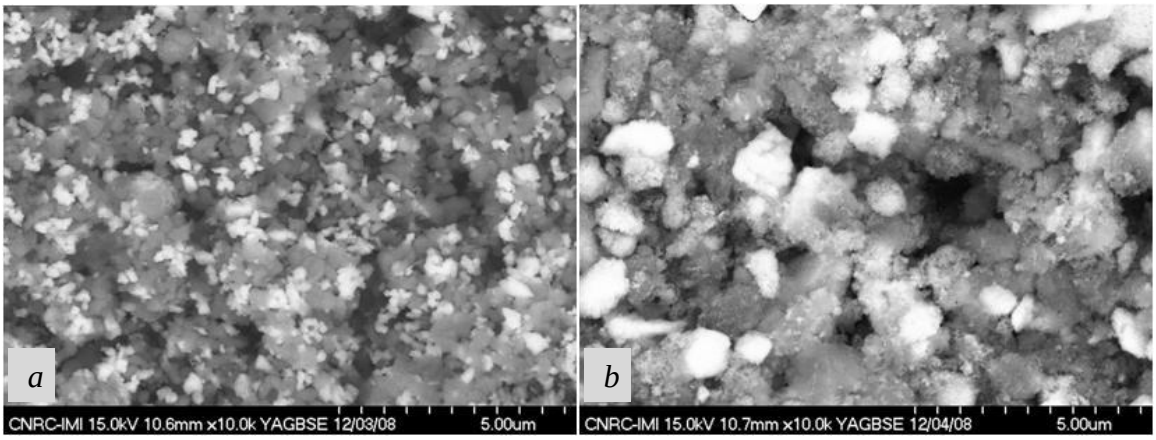

Figure 5-1 SEM micrographs of aggregates in the dried suspensions of a) micron-powders and b) nano-powders

The in-flight particles resulting from spraying the micron- and nano- powder suspensions and collected in the water are shown in Figure 5-2 (a) and (b), respectively.

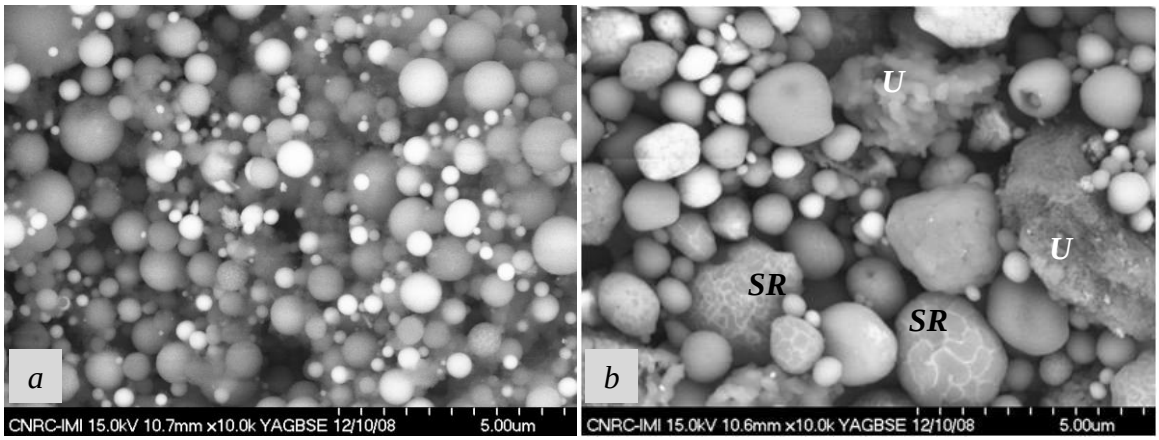

Figure 5-2 Collected in-flight particles sprayed into water: a) micron-powder presenting fully molten round particles and b) nano-powder that contains also semi-molten and resolidified (SR), as well as unmolten (U) particles

In this figure, it is clear that the in-flight particle size resulting from the smaller aggregates of micron-powder suspension is smaller than that of the nano- powder suspension. This means that the smaller aggregate size before spraying will end up with a smaller sprayed particle. In addition, the particles from micron-powder suspension in Figure 5-2(a) are completely round, which indicates their full melting within the plasma path. In contrast, the in-flight particles from nano-powder suspension, at the end of their route in plasma, contain plenty of unmolten or partly molten and resolidified particles, as shown in Figure 5-2(b). Since the suspensions in this case were sprayed under different conditions, it was found that the resulting particle temperature and velocity for nano-particles were (3140°C, 523 m/s), while those of micron-suspension were at (3050°C, 745 m/s). It was expected at this lower velocity (longer time) at higher temperature for the nano-powders to yield a substantial degree of melting. However, it seems that the lower density (high porosity) has resulted in escaping of many nano-powder aggregates to the cold periphery of the plasma flame and prevented them from melting.

The coatings resulting from these suspensions are shown in Figure 5-3. It can be seen that in the coating from nano-powder in Figure 5-3(b) the lamella are thicker and more distinct black (alumina) and white (YSZ) areas than in Figure 5-3(a). This is the result of the larger aggregates of nano-powders, many of which are of the same material instead of being a mixture of alumina and YSZ.

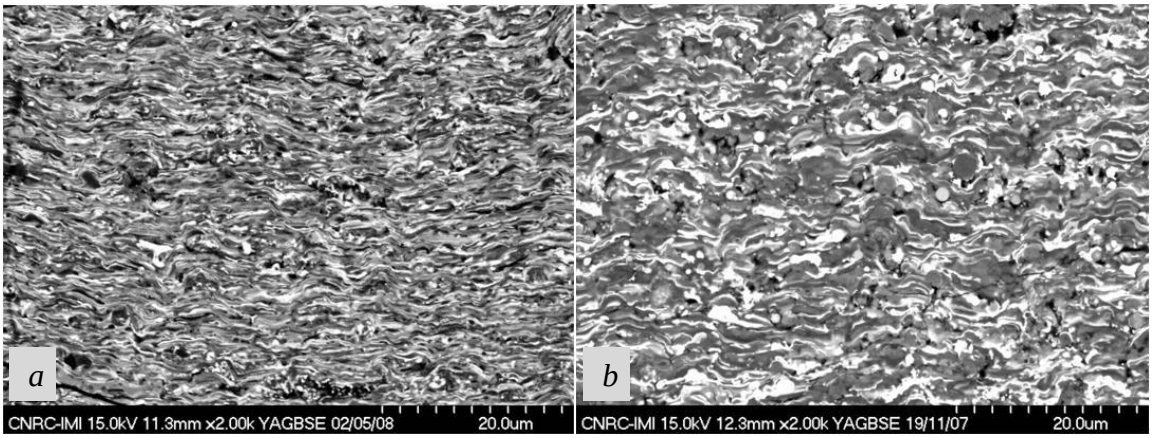

Figure 5-3 Microstructures resulting from a) micron- and b) nano-powder deposition showing more distinctive color and thicker lamella in nano-particle coating compared with the coating of micron particles with the same spray conditions

Based on the comparisons presented in Table 5-2 by changing the initial particle size from nano to a few microns (about two orders of magnitude larger), the crystallization peak area in the DSC graph has increased by 6 to 20%. This result is supported by XRD calculations as a 13% to 56% increase in the amorphous phase in the same couple (the larger increase has happened at higher robot speed). This suggests that nano-particles are more prone to maintaining crystallinity, probably due to incomplete melting in the plasma flame. In addition, the lower mixing proportion observed in the particles and transferred to the coating of the nano-particles reduces the chances of amorphous formation. The role of the in-flight alloying in this regard is discussed in more detail in section 5.3.

B. Robot Speed

While other parameters are constant and the resulting in-flight particle temperatures and velocities are closely comparable, Table 5-2 shows that decreasing the robot speed from a maximum of 2 m/s to 1 m/s results in some decrease in the amount of the amorphous phase. The change ranges between an negligible amount of 2% in the case of coatings using nano-powders to 15% for coatings from micron-powders, based on DSC analysis. This comparison by XRD pattern calculations for nano-powder deposition shows no change in amorphous content by robot speed, but 42% decrease in amorphous content at lower robot speed for micron-powder coatings. Considering the close distance of the torch to the substrate in SPS process compared with other common practices of plasma spray, a severe heat flux is expected to be impressed by plasma jet to the coating [48]. Therefore, lower amorphous content at slower robot speed can be attributed to crystallization of some of the solidified amorphous phase retained for a longer time under the heat of the plasma flame. The inconsiderable role of robot speed in the case of nano-particle coatings is somewhat unexpected and could not be explained in the course of this work.

C. Particle Velocity

To provide different particle velocities, the spray conditions were changed and two couples of samples – (2, 5) and (4, 6) – were produced using the micron-powder suspensions with constant robot speed. It can be seen in Table 5-2 that increasing in-flight particle velocities with similar or close particle temperatures reduces the amount of amorphous phase in the resulting coating. By an increase of about 48 m/s in particle velocity, from sample 2 to 5, the amorphous content is reduced by 5%, but at the higher

velocity change between sample 4 to sample 6 of about 78 m/s, the amorphous phase drops by 20%. The XRD results also support this decreasing trend of amorphous phase with increased in-flight particle velocity.

Higher in-flight particle velocity was found to increase the metastable phases such as γ-alumina and cubic zirconia due to accelerated cooling rate [118]. In a similar manner, it was expected also that the amorphous phase would increase at a higher particle velocity. Thus, this decrease in the amorphous phase at higher particle velocities seems unexpected. This is also contrary to the experiment with pure alumina showing the amorphous phase formation concurrent with γ-alumina at the substrate interface and extremely high cooling rates [104]. Nonetheless, in alumina-yttria eutectic system the amorphous phase is reported to appear along with α-alumina [119]. This apparent conflict will be cleared subsequently in this thesis after confirming this result with more investigation.

D. Particle Temperature

Using three different spray conditions the in-flight particle temperatures were varied while the particle velocities were still comparable and other parameters were constant. The results in Table 5-2 show that at very high particle temperatures (more than 3000°C) compared with melting point of the components coatings contain a lower amorphous percentage. This decrease between the two samples 8 (T_p=3064°C) and 12 (T_p=3430°C) has ended with a 27% decrease in the amount of the amorphous phase. The same comparison between samples 12 (T_p=3430°C) and 10 (T_p=2830°C) yields about 33% change.

Such a difference is visible in Figure 5-4, which shows the superimposed XRD patterns of samples 10 and 12. This figure indicates that not only the amorphous hump but also the crystalline phase is affected by greatly higher particle temperature. Despite the presence of the crystalline peaks in Figure 5-4, the high amorphous content of more than 50% (Table **5-1**) can be explained by very low intensity of the crystalline peaks (maximum 900 counts compared with intensity levels beyond 5000 counts in crystalline structures) that also can be noted in the same figure.

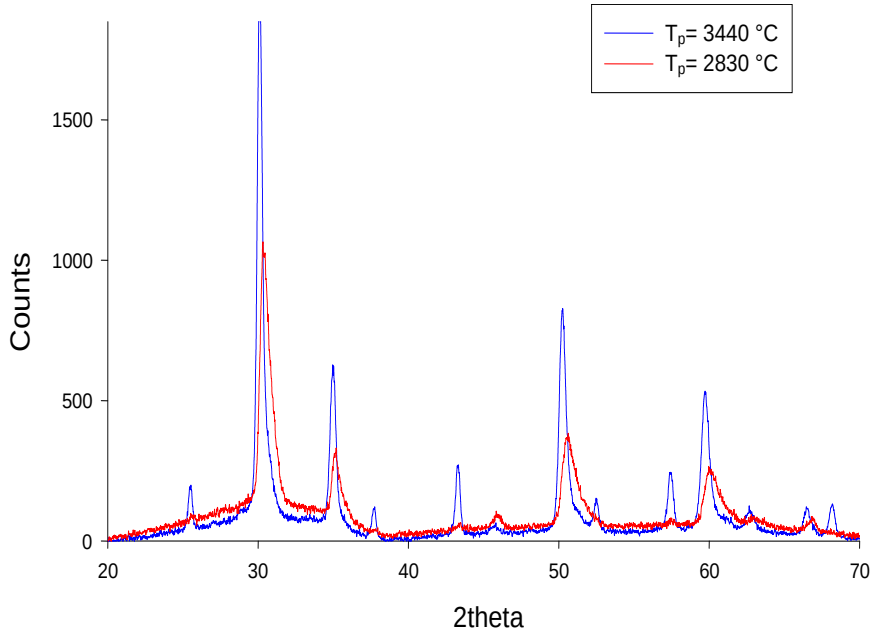

Figure 5-4 XRD pattern for the two coating samples resulting from different in-flight particle temperatures, showing smaller amorphous hump and higher crystallinity at higher T_p

Extremely high upcoming particle temperature (far beyond the melting point of the components, yet below their boiling point) upon impact should have reheated the substrate. The temperature raise of the solidified underlying splats to beyond crystallization temperature has caused diminishing of the amorphous phase by

crystallization process. In addition, the hot substrate promotes the formation of α-alumina at lower cooling rates [75].

In reporting the in-flight particle temperatures in SPS process using Accuraspray, it is noteworthy that the measurements may sometimes be interfered by the radiations from the plasma flame. In such condition, the measured temperatures can be somewhat higher than reality. However, since this is a systematic error the comparison is still possible.

E. Substrate Preheat

To study the role of preheating the substrate, comparison was first done between the samples (7, 8) by both DSC and XRD. Table 5-2 presents a 28% increase in DSC crystallization peak area for the coating on preheated substrate compared with the coating on non-preheated substrate. This increasing trend, based on the same table, was confirmed by the XRD results. Two additional couples were compared just by XRD calculations in samples (9, 10) and (11, 12) and confirmed the above results (that means higher amorphous content was found in the coating on heat-treated substrate). It was also observed that preheating the substrate to 350°C, while providing coatings of higher quality, with almost half the number of horizontal and vertical cracks, reduces the grain size of all present phases (i.e., α- and γ-alumina, t/t' zirconia). This comparison is presented in Figure **5-5**. Since in the preheated substrate there is normally a better interface bonding between the coating and the substrate by improved splat spreading and interface contact [30], lower contact resistance at the interface helps more rapid heat extraction from the coating, which results in smaller grain size in all the phases formed.

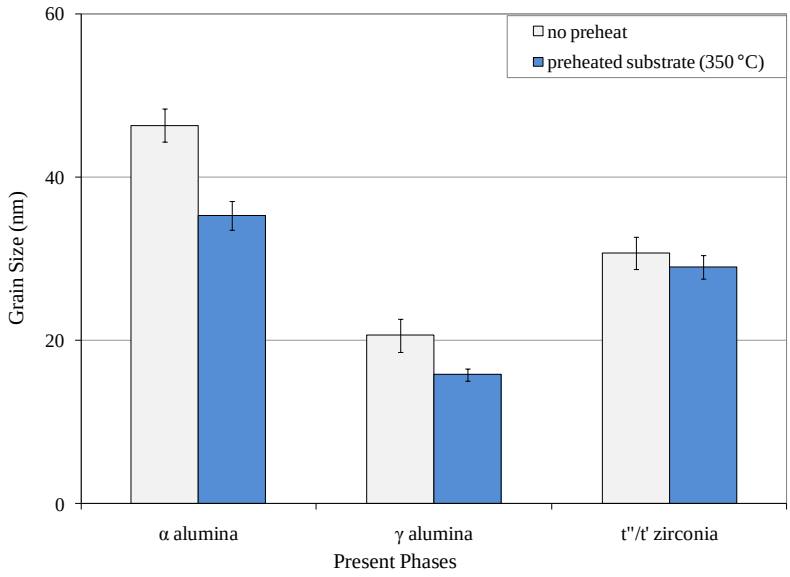

Figure 5-5 Substrate preheat effect on the grain size of as-deposited coating

It may also be noted in Figure **5-5** that the grain size of the γ-alumina is smaller than in α-alumina as well as zirconia phases. According to the classical theory of solidification, for heterogeneous nucleation in contact with another surface the critical free energy for formation of each phase is as per the formula in Equation 5-1 [115].

$$\Delta G_C = \frac{16\pi(\rho_l T_m)^2 \sigma^3 f_{(\beta)}}{3\Delta H_m^2 \Delta T^2} \qquad \textbf{Equation 5-1}$$

Where $\Delta T = T - T_m$ is the undercooling, σ is the solid-liquid interfacial energy, the heat of fusion, $f_{(\beta)}$ is a function of wetting angle β. Using T_m for γ-alumina as 2289°C and for α-alumina as 2327°C and other data from [75], and applying the wetting angle from [120] that is below 35° for γ phase and above 45° for α-alumina, the above formula suggests that for every solidification temperature, γ-phase has a much larger negative ΔG_c, resulting in higher nucleation rate and smaller grain sizes than α-phase.

It should be noticed that both samples (with and without preheating the substrate to 350ºC) in this comparison are deposited simultaneously and all other parameters are

exactly the same. Thus, the particles experience the same exact melting and mixing conditions.

F. Number of Deposition Passes

Increasing the coating thickness was done by increasing the number of deposition passes under the same spray conditions. The amount of amorphous phase in the samples with 100 passes of deposition (with 220 µm thickness) was higher than in the coating with 150 passes (330 µm). This should be the result of increased recurrence of heating the coating to crystallization temperatures. Another reason for lower amorphous content in the thicker coating (acting as insulation) can be attributed to the greatly reduced cooling rate. Nevertheless, this dependency was not observed in the coating with 50 deposition passes (90 µm). That means the amorphous content in the coating formed with 50 passes, in spite of the coating being of minimum thickness, was less than the two other coatings with higher thicknesses. Figure 5-6 shows this coating and its interface with the substrate. It can be seen that there is a clear disconnection between the coating and the substrate, shown by the arrow. The loose interface eliminates rapid heat withdrawal from the coating through the substrate. This observation suggests the importance of interface contact resistance on amorphous phase formation.

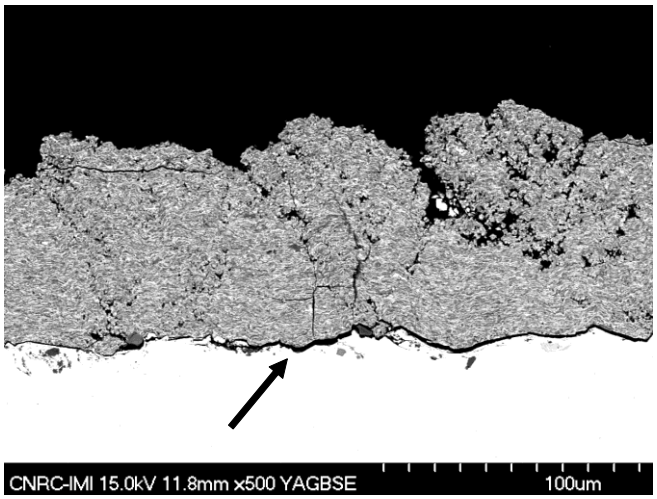

Figure 5-6 Loose interface contact between the coating and substrate, causing lower cooling rate of the upcoming splats

In addition, the discontinuous microstructure of this sample is due to the plasma arc instability during deposition of this coating that prevents appropriate intersplat bonding and heat transfer to the substrate. Therefore, the coating made with 50 passes is showing an unexpectedly lower amorphous content, despite lower thickness and number of passes than the two other coating samples.

G. Bond Coat

The coatings for studying the effect of the presence of bond coat were simultaneously deposited on mild steel bare substrates and bond coated mild steel substrates using nano-powder suspension. The XRD patterns of the bond coated and bare steel substrates were almost similar (except a slightly higher intensity in crystalline peaks at lower angles in the coatings on bare substrate), and the amorphous humps were overlapping in both types of sample. The reason for this is that the metallic bond coat has a thermal diffusivity close to that of the steel base material. The only difference might happen when the interface with the steel substrate is poorer than that of the bond coated substrate. As long as the substrate and coating contact qualities are the same, the role of the bond coat on cooling

rate, crystalline phases and even amorphous phase content has been found to be negligible, as observed in this experiment.

5.2. Coatings Amorphous Contents and Crystallite Sizes

The grain size of the solidifying crystal is directly dependent on the cooling rate, and the smaller grain size under the same nucleation conditions can be translated to higher cooling rates. Hence, to evaluate the importance of the cooling rate on the amorphous phase formation, the grain sizes of a large group of samples have been measured, regardless of the condition causing the change in the cooling rates.

The relation between the grain sizes measured for each crystalline phase and the amorphous content in each coating is illustrated in Figure 5-7. In this figure, it can be seen that the smaller grain size of different phases (as a sign of higher cooling rate) is not concurrent with higher amorphous content. This suggests that the role of cooling rate (within the range of plasma spray cooling rates) on the amorphous content is preceded by some other parameters with stronger role. Figure 5-7 also confirms that γ-alumina has usually the smallest grain size among the phases present, as explained above. In addition, in this figure it can be seen that in the case of zirconia by increasing the amorphous phase a slight increase in the grain size is observed.

As discussed in section 4.2, higher amorphous content is mostly coincident with formation of α-alumina. Meanwhile, the decrease of amorphous phase at lower particle velocities requires a more detailed investigation of the probable role of the in-flight particle velocity on the amorphous phase formation.

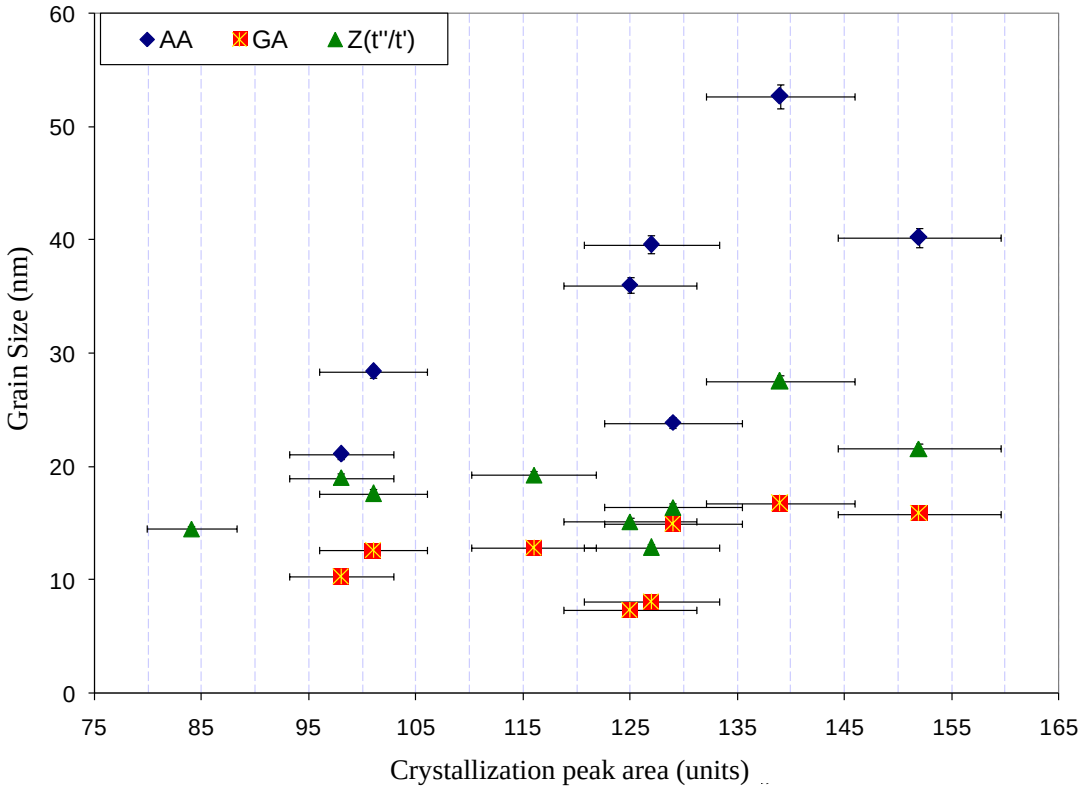

Figure 5-7 Grain size of different phases versus crystallization peak area (as comparison basis for amorphous phase) in each coating sample deposited under various conditions with SPS process

Figure 5-8 shows the relation between the amorphous phase and in-flight particle velocity in a group of samples deposited with different spray conditions. This figure suggests that in the presence of many other variations, the general tendency for a large group of samples is the reduced amorphous formation by increasing the in-flight particle velocity (that means the reduced time of exposure to high temperature for the particles). This observation has to be related to the in-flight mixing discussed in Chapter 3 and section 5.3 that in the case of alumina and zirconia can only happen in molten state, since, according to their equilibrium phase diagram, they are highly insoluble in solid state [121]. The slight grain size increase in α-alumina phase at higher amounts of amorphous phase (that is coincident with lower particle velocity) can be due to the reduced cooling rate at lower particle velocities as a result of less splat flattening [118].

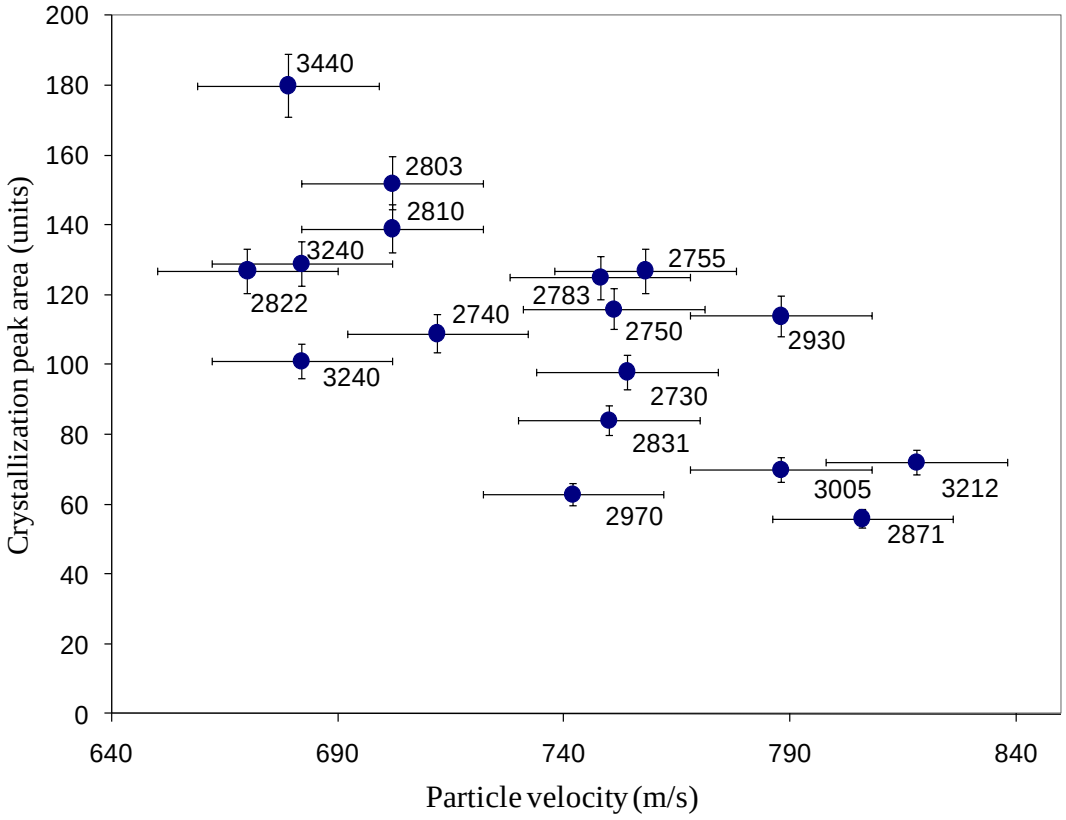

Figure 5-8 Crystallization peak area vs. in-flight particle velocity showing formation of smaller amount of amorphous phase at higher velocities (The in-flight particle temperatures in ºC are shown on the data points)

The variations in progression of melting and mixing phenomena may be recognised as a fundamental characteristic of thermal spray processes in deposition of composite materials that differentiates them from other processes involving rapid solidification. In such processes, fully molten and well mixed composite allows the comparison of the crystalline and non-crystalline phases simply according to the molten particle dimensions and/or the cooling rates [101]. This issue will be discussed further in section 5.3.

As a summary, in this part of the work, the roles of several parameters on the amount of amorphous phase formed within SPS coating of alumina-YSZ composite have been studied. It was revealed that larger powder feeds within the range of a few micron or submicron sizes are more prone to form amorphous phase than smaller particles with

nanometric size. Other ways to ensure amorphous phase within the coating include application of higher robot speed and deposition on preheated substrate. Selection of spray parameters resulting in lower in-flight particle velocities and lower temperatures (above the melting temperatures of the components) are in favour of larger amorphous contents also.

In contrast, extended number of deposition passes can result in elimination of this phase within the structure. Moreover, the application of bond coat has no role on the amorphous phase formation. However, any factor that can effectively reduce the coating-substrate bonding and efficient heat dissipation from the coating can strongly diminish the formation of amorphous phase.

In plasma spray deposition of the small composite powders using SPS process, the role of lower in-flight particle velocity precedes the importance of higher cooling rate in amorphous phase formation. The reason most probably is related to the importance of mixing process that is a prerequisite for amorphous formation and the fact that amorphous formation in the pure material is of quite low possibility. This fact is further investigated in section 5.3.

5.3. Sources of Amorphous and Crystalline Phases in SPS Coatings

The main focus of this part of the study is to find the sources of the amorphous phase in the SPS process. In addition, this section helps a comparison of SPS with APS (studied in Chapter 3). To generate the samples, SPS process was used for deposition of three different powders with pseudo-eutectic composition of alumina-8 wt% YSZ, and one 8 wt% YSZ powder as the reference point. Powder mixtures with a weight ratio of 60/40

for alumina/8 wt% YSZ were produced in three different groups in terms of size range or morphology. Table **5-3** summarizes the feed powders and the detail of the sprayed powder mixtures. Samples were produced by spraying the 30 wt% solid concentration suspension (as explained in section 4.1).

Table 5-3 Powder feed details

Powder #	Powder mixture type	Feed powder mixture detail
1	Agglomerates of nano-particulates	Al_2O_3/3YSZ 60/40 (Tosoh, Grove City, OH, USA, 45 µm)
2	Loose nano-powders mixture	(8 mol% YSZ+3 mol% YSZ) (both Inframat Advanced Materials, Farmington, USA; 30-60 nm) + Alumina (Nanoamor Advanced Ceramic Materials Inc., Houston, TX. USA; 23-47 nm)
3	Loose micron-powders mixture	8 mol% YSZ from (Unitec Norwal, CT, USA; average size 1.5 µm) + 3 mol% YSZ (Tosoh, Grove City, OH, USA; average size 2 µm) + Alumina95% pure (Malakoff, TX, USA; average size 1.4 µm)
4	Nano YSZ mix	(8 mol% YSZ+3 mol% YSZ) (both Inframat Advanced Materials, Farmington, USA; 30-60 nm)

The gas-assisted atomization was done with two different methods. First was by atomizing the suspension using a central tube passing through the liquid injection tube (in Figure **2-2**). This central tube was used for carrying the argon atomizing gas with a 6 slm flow rate. In addition, nitrogen shielding gas at 1 slm was transferred to the torch exit through the space between the injection tube and the nozzle. This system of injection and atomization using two gases is called “system 1” in this text. The second method was liquid injection without central gas carrying tube and just 14 slm nitrogen gas passing through the gap between the injection tube and the nozzle, called “system 2”.

System 1 was supposed to improve the deposition condition by reducing the clogging at the tip of the torch as well to enhance melting by atomizing the droplets into smaller fragments. In practice, even though the jet stability looked better and the clogging was largely reduced, the particle fragmentation and melting and the coating qualities (integrity) were clearly better when system 2 was used. Details of the coating qualities and particle melting in both cases will follow.

The spray condition and injection system for each mixture, as well as the resulting particle velocity and temperature (as V_p and T_p) are indicated in Table **5-4**. In addition, the amorphous phase contents and the crystallization peak area in the collected particles and the coatings are listed in the last two columns of Table **5-4**. The amorphous contents reported for the coatings are based on the XRD calculations (details as in section 2.5.2), and the results for the collected particles are either DSC or are converted from XRD measurements to DSC results (using the slope of the line in section 2.5.2.3 which related the XRD results to the DSC crystallization peak sizes) to enable the comparisons.

5.3.1. In-Flight Collected Powders

The measured crystallization peak area in Table **5-4**, when system 1 was used for spraying, was minimum for powder#2 (loose nano-particles), i.e., 10 units. This peak in the case of powder#1 (agglomerated nano-particulates) was slightly higher, equal to 12 units. The largest amount of amorphous phase was formed after spraying powder#3 (micron-size particles), with crystallization peak area as large as 28 units.

However, using system 2 resulted in larger crystallization peak areas in both powders. So that for sprayed powder#2 the peak area increased to 20 units and that of powder#3 was as large as 42 units. To investigate the reason for these differences, the micrographs of

the collected particles, shown in Figure 5-9, are used. In this figure, the different size and melting ratio of the porous aggregates of nano-powders in either loose or agglomerated conditions as compared with dense (non-porous) micron-particles is evident.

Table 5-4 Spray condition and the resulting amorphous contents

Powder #	Plasma gas composition	Total plasma gas (slm)	Current (Amps)	Plasma power (kW)	Robot speed (m/s)	Number of passes	Injection system	Feed rate (kg/hr)	Solid content (%)	T_p±30 (°C)	V_p±10 (m/s)	XRD calculated amorphous phase contents ±3% for coatings	Crystallization peak area of collected powders ±5% (units)
1	$Ar/N_2/He$ 75/10/15	245	200	61	80	35	1	1.8	30	2905	608	45%	12
2	$Ar/N_2/He$ 75/10/15	245	200	61	80	35	1	1.8	30	-	630	25%	10
3	$Ar/N_2/H_2$ 65/15/20	275	240	114	40	26	1	1.8	30	3082	740*	11%	28
2	$Ar/N_2/He$ 75/10/15	245	200	57	80	60	2	1.5	25	3080	612	36%	20**
3	$Ar/N_2/H_2$ 65/15/20	275	240	114	40	60	2	1.5	30	3080	612	48%	42**
4	$Ar/N_2/H_2$ 75/10/15	245	200	86	80	90	2	1.5	25	2950	640	-	-

*Particle velocity for the collected in-flight particles was different and equal to 698 m/s

**Converted to DSC results based on linear relation with XRD measures in section 2.5.2.3 (Data validation)

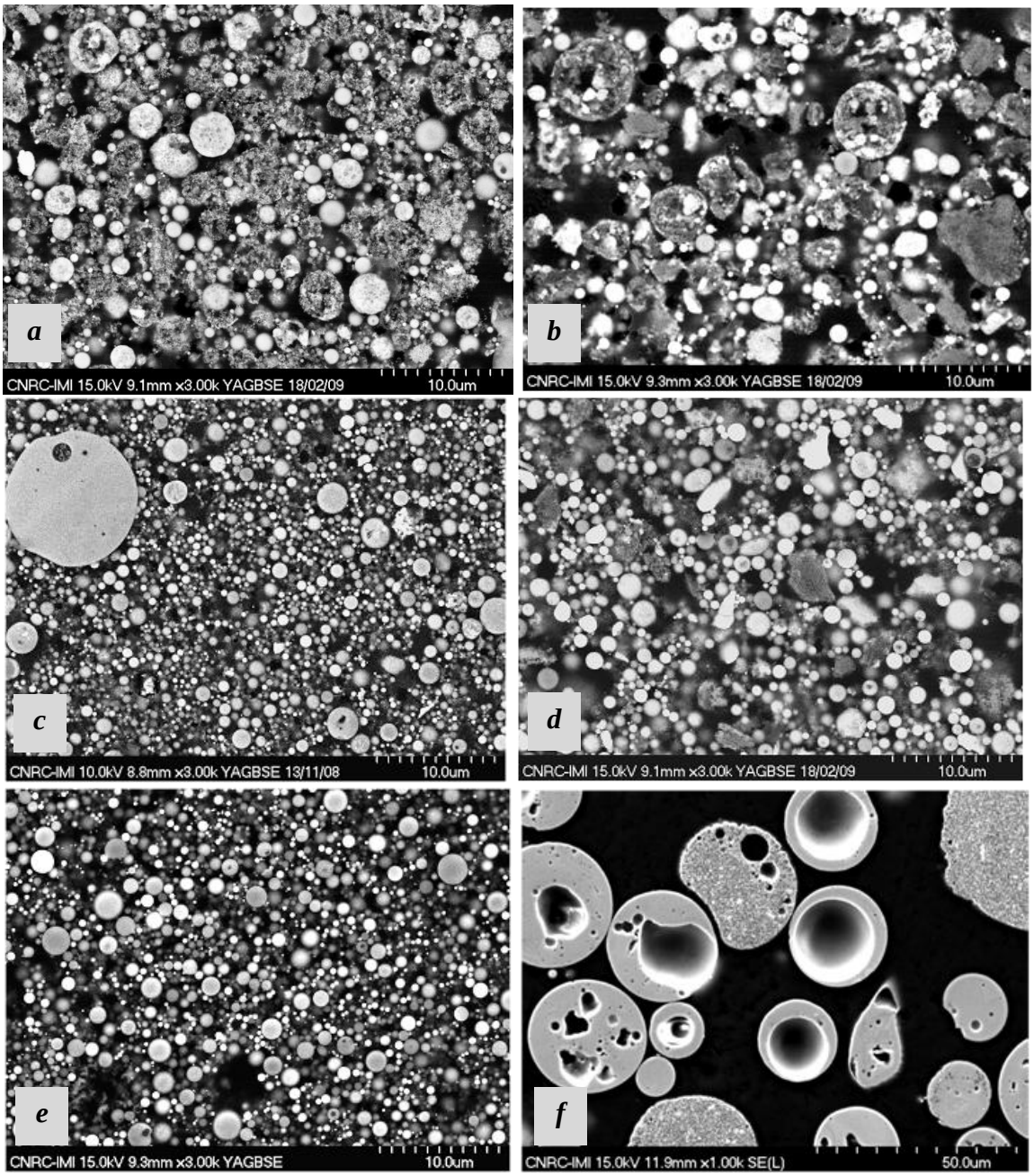

Figure 5-9 In-flight particles collected in water after spraying with SPS process at 3000X from a) powder #1 (large agglomerated nano-particulates) using system 1; b) powder #2 (loose nano-particles) sprayed using system 1; c) micron-particles by system 1; d) the same as b, sprayed using system 2; e) the same as c, sprayed using system 2; f) powder #1 sprayed with APS at 1000X

The reason for different behaviour of nano- and micron-particles against the atomization process, and also the function of the atomizing system and its interaction with the flame, are specialized subjects that require detailed studies. However, the differences in melting

and mixing behaviour in this investigation helped to find out the significance of these processes. The role of these phenomena on amorphous formation could explain why the particle velocity played such a considerable role, a role that could exceed the importance of the cooling rate.

On the other hand, collected particles of powder#3 (micron-powders) after spraying with systems 1 and 2, shown in Figure 5-9(c) and (e) respectively, are clearly smaller than those of nano-powders. This suggests their better treatment (in terms of heating, melting and shear forces on the molten droplet) by plasma flame resulting in extensive fragmentation. In addition, the totally round shape of almost all of these particles (micron-size) indicates their advanced melting. Better heat treatment and melting in the plasma flame has resulted in larger amorphous phase in this powder type, which initially consisted of comparatively large and dense particles. The effect of applying system 2 for powder#2, also, can be observed by comparing Figure 5-9(b) and (d) in which better fragmentation and more melted round particles can be distinguished when system 2 is used.

Figure 5-10 demonstrates two different steps of melting in typical particles of powder#2. Figure 5-10(a) is a particle in the initial stage of melting, with a large proportion of initial particles with distinct color of each component (white zirconia and black alumina). It is expected that such partly melted particles will preferably solidify in crystalline structure, because of the presence of unmolten crystalline solids that play the role of nucleation sites of crystalline structure. During heating and melting in the flame, the mixed region is readily extended and appears as the developed grey color in the particle observed in Figure 5-10(b). The main difference between using systems 1 and 2 in the particles

collected from powder#2 was that the number of well melted and mixed particles, as in Figure 5-10(b), was greater when system 2 was used. Likewise, the observed change in amorphous phase content in powder#3 sprayed by the two systems was found to be for the same reason, which is the different melting and mixing.

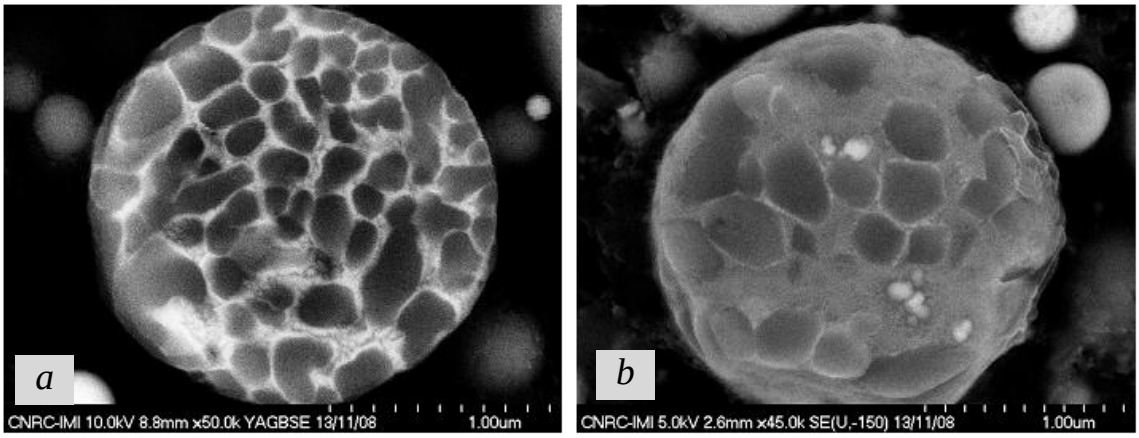

Figure 5-10 SPS-sprayed powder #2 (loose nano-powders mixture) showing different stages of melting and mixing in the plasma jet: a) partly melted with crystalline particles retained; b) largely melted with extended mixing (grey color)

5.3.2. Comparison of the Collected Powders in SPS and APS

As mentioned earlier, this part of the study is also looking for the similarities and differences between APS and SPS processes. Figure 5-9(f), at 1000X, shows the collected powders after APS spraying of powder#1 (from the experiment detailed in Chapter 3) and allows the comparison of the particle sizes resulting from the two processes. It is evident that particles from the SPS process, as in Figure 5-9(a), are much smaller than what was formed in APS (average size of 1.6 µm from SPS compared with 45 µm from APS spraying of the same powder). It is noteworthy that the micrograph in Figure 5-9(a) from SPS particles is at three times higher magnification than that of Figure 5-9(f) from the same powders sprayed by APS. Since the major difference between the two processes is the presence of a liquid carrier in SPS, the considerably smaller particle size can be

mainly related to the presence of the liquid carrier. This observation is compatible with the result of the experiment by Chen et al. [122], where in HVOF deposition of the powder by liquid carrier process (solution precursor high-velocity oxy-fuel spray) they observed ten times smaller splat size as compared with dry deposition with HVOF process (2-5 μm splat diameter when using the liquid precursor compared with 30-50 μm with dry deposition of powder using the same process). The reason is known to be the significant in-situ break-up of the liquid precursor and formation of small droplets in the high-velocity HVOF flame [122]. Such liquid break-up in dry deposition is not possible. This explanation can be applicable to SPS process, as well.

On the other hand, Figure 5-11(a) to (c) illustrates various types of particles formed during spraying the nano-powders into water, which are observed in both loose and agglomerated sprayed powders (powders#1 and 2), at high magnifications. In the comparison of the particles collected from SPS with those from APS process, discussed in section 3.1, there are some similarities, one of which is the presence of collected particles with dendritic solidification. Examples can be found in Figure 5-11(a) with fully dendritic structure and Figure 5-11(b) that shows a partly mixed particle in which the dendrites are formed. These particles can be more readily found among the particles sprayed with system 2 with higher melting proportions. Nevertheless, in case of SPS particles, dendrite sizes are much smaller (less than 100 nm size) than what was found in APS-sprayed micron-particles. In addition, particles with no sign of crystalline grains, as in Figure 5-11(c), were found among SPS-sprayed particles, as was previously observed in APS process. It is assumed here that these particles are the source of amorphous splats.

Conversely, particles with indications of eutectic or cellular crystallites, observed in APS-sprayed large particles, were absent when spraying the small particles using SPS. The reason can be the invisibly small grain sizes within the small particles, and limited magnification of the present SEMs to provide higher magnifications in observing them.

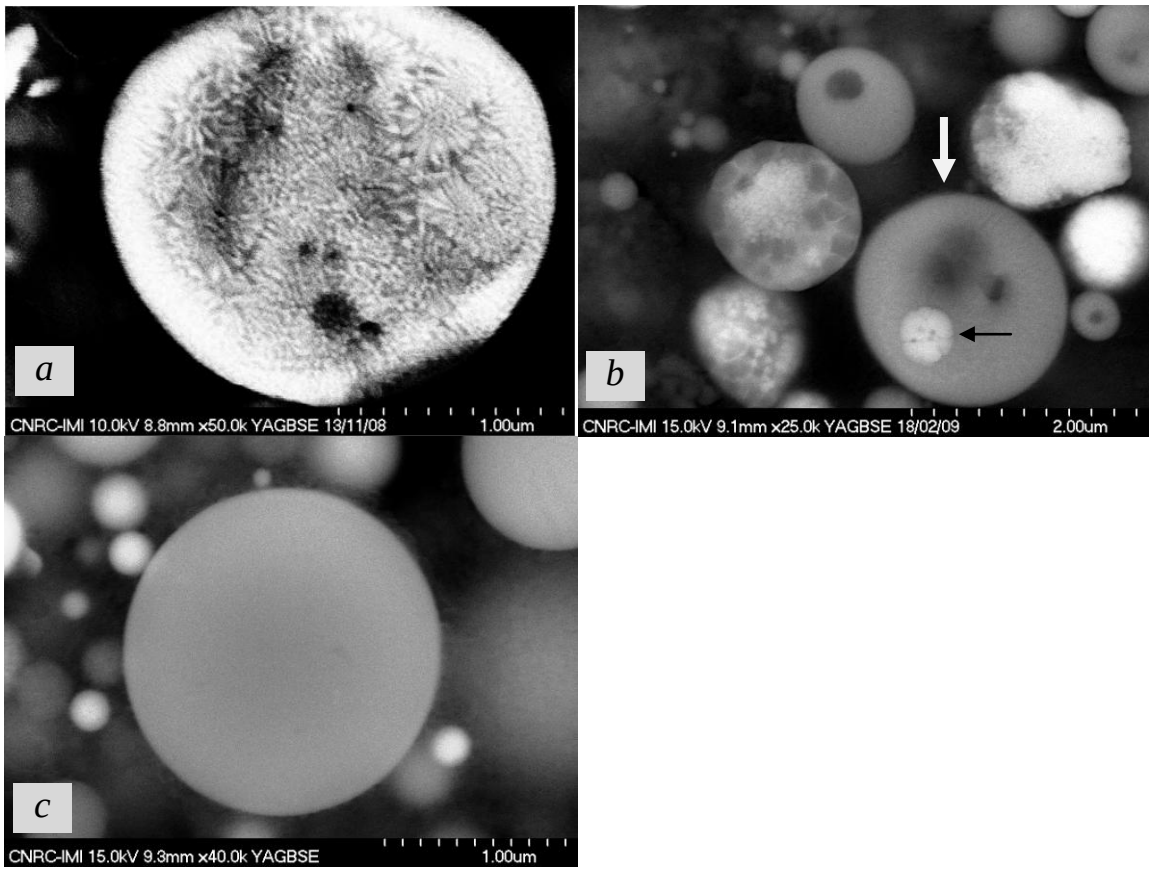

Figure 5-11 SPS-sprayed nano-particles collected in water: a) fully dendritic growth in unmixed particles; b) dendritic growth in partly mixed particle (arrowed); c) non-crystalline particle

The absence of eutectic or cellular structure in the small particles (of SPS process) can also be attributed to the extremely high cooling rates of small particles in SPS. Thus, if any mixing happens, the dense (no porosity) and extremely small particle (less than 2 μm) tends to form amorphous phases instead of the crystalline phases reported in the large and porous particles (Chapter 3). The reality about formation of the crystalline structures with high dissolution of solute atoms can be concluded from XRD patterns. In

these patterns peak shifting may happen by solid solution formation in, either zirconia or alumina crystals, and lattice parameters can show the solid solubility variation in the crystalline solid. Such evaluation will follow in the coming sections.

Another difference between the APS and SPS sprayed powders is the segregation of the zirconia solid component outward the large unmolten particles of agglomerated powders. In SPS process, sometimes the segregation of dissimilar powder particles was observed (to a very limited extent), as in Figure 5-12(a). However, most of the particles have not encountered this, because of the short traveling path and high speed in SPS process; and they have maintained the initial form of the unmolten aggregates, as in Figure 5-12(b).

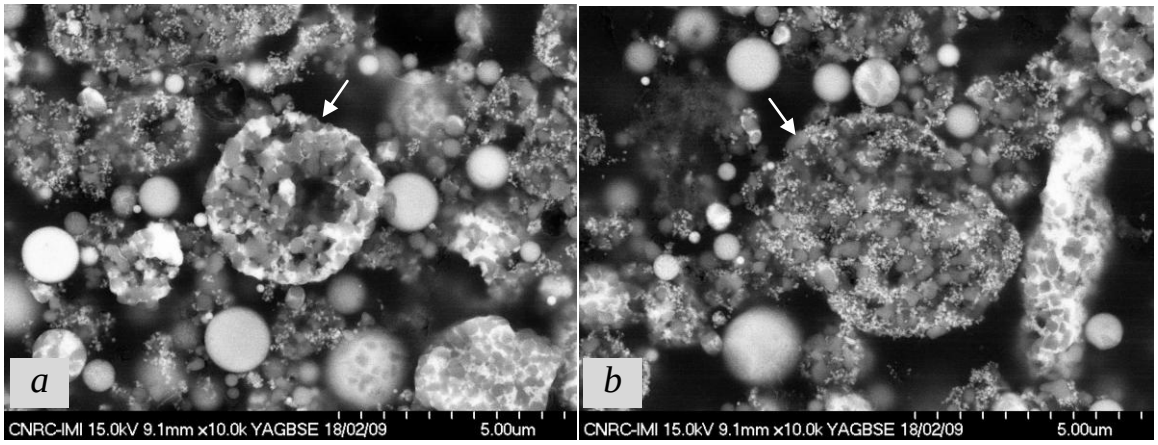

Figure 5-12 Unmolten particles collected in-flight from SPS process: a) partial segregation of components started; b) no segregation accomplished

It should be noticed that in the coating samples some different trends may be expected than in collected powders, as they will be influenced by other spray parameters such as number of deposition passes and spray robot speed.

5.3.3. SPS Coatings Using Different Powders

The resulting coatings from the powders detailed in Table **5-3** and sprayed under conditions as in Table **5-4** can be compared in Figure 5-13(a) to (e). In addition, Figure

5-13(f) shows an 8 wt% YSZ (powder#4) coating using system 2. This coating was produced for comparison of some of the properties of the material of interest with this material as the present TBC.

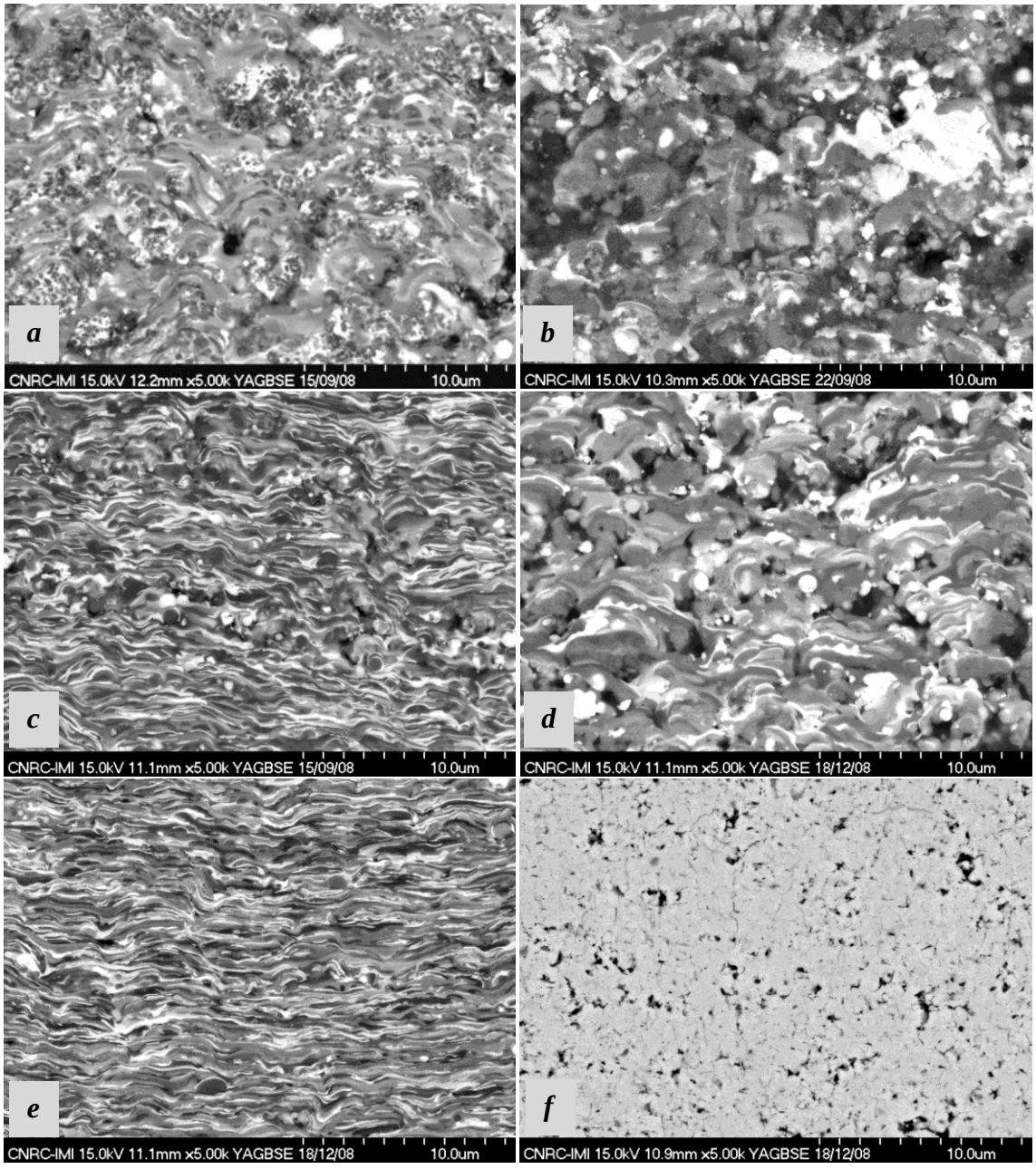

Figure 5-13 SPS coatings from: a) powder #1 sprayed with system 1; b) powder #2 sprayed with system 1; c) powder #3 sprayed with system 1; d) same as b, sprayed with system 2; e) same as c, sprayed with system 2; f) 8 wt% YSZ nano-powder coated with system 2

Figure 5-13(a) from powder#1 (agglomerated nano-particulates) deposited using system 1 presents a low melting fraction. In this figure the unmolten or partly molten particles are cemented in the fully molten splats forming a bi-modal structure (consisting of aggregates of unmolten nano-particles embedded in the molten and solidified structure), as found by Lima et al. in APS coating of 7 wt% YSZ [123]. This coating consists of uniformly distributed phases and integrated microstructure. The molten part has formed a homogeneous structure, as observed in the non-crystalline particles of the collected powders. However, this bi-modal structure consists of much smaller entities in terms of both splat size and unmolten particles than when APS is used [123].

Coatings from the powder#2 (loose nano-powders) injected using system 1 are shown in Figure 5-13(b). In spite of continuity, these coatings possess very loose intersplat connections of dissimilar splats with irregular boundaries and low mixing ratios. The coating in Figure 5-13(d), using the same powder applied with system 2, in spite of the better melting conditions still lacks well-bonded splats. This is mainly because of the large fraction of partly molten particles observed in the corresponding collected particles in Figure 5-10(a). The coatings from micron-powders in Figure 5-13(c) and (e) propose the improved melting and flattening when system 2 is used.

The calculated amorphous contents for the coatings as summarized in Table **5-4**, show that as a result of improved melting in powder#2 with system 2, this quantity has increased from 25% to 36%; and in the coatings of powder#3 a jump from 11% to 48% has occurred. It can, therefore, be expected that particles with full melting and mixing, and negligible or no retained unmolten solid, can show the best potential for amorphous formation within the coatings.

The monotonic structure of the 8 wt% YSZ deposited by SPS (Figure 5-13(f)) presents porosity sizes from nano to a few microns. In addition, in this figure, no clear intersplat boundary can be found. This is in contrast with alumina-YSZ coatings in Figure 5-13(a) to (e) with a large number of intersplat boundaries between the alumina and zirconia splats. This microstructural difference (apart from material dissimilarity) can result in differences in the properties especially at high temperature, as will be discussed in section 6.5.

5.3.4. Sources of Crystalline Phases and the Nature of Amorphous Phase

The XRD patterns of the resulting coatings, in Figure 5-14, propose similar crystalline structures for the four above coatings that consist of a combination of mainly cubic zirconia and ($\alpha + \gamma$) alumina as shown in Figure 5-14(a). The exception is the coating shown in Figure 5-14(b) that is powder#3 (micron-powders) produced with system 2. This coating with the highest amorphous content (48% based on Table **5-4**) presents only γ-alumina phase. This suggests the extensive melting and disappearance of the initial crystalline structure of the powder (α-alumina), and solidification at high cooling rates.

The structure of the nano-powder of 8 wt% YSZ (without alumina) deposited with SPS process in Figure 5-14(c) illustrates mainly cubic as well as some monoclinic zirconia in spite the comparatively high content of yttria stabilizing agent. This structure is different from that found in Chapter 3, where deposition of the same material using APS process results in mainly tetragonal structure. This difference can be explained with the high heat input from the torch to the substrate due to the short distance and much higher particle

velocity and temperature (found to be effective on phase formation as discussed in section 4.2) compared with APS, causing the formation of metastable phases.

The sources for the crystalline structures in the composite coatings, other than unmolten particles, can be the discrete splats of the unmixed material that tend to solidify in crystalline form rather than amorphous. Nevertheless, at extremely high cooling rates alumina splats on mild steel substrate interfaces have presented a very limited amorphous phase [124]. The other possibility reported in APS deposition of this composite, as detailed in Chapter 3, is the solid solution formation. To investigate the formation of such crystalline solid solutions, the lattice parameters of various phases were measured using the PowderCell program for structural refinement of the patterns, based on Rietveld method as detailed in section 2.5.4.

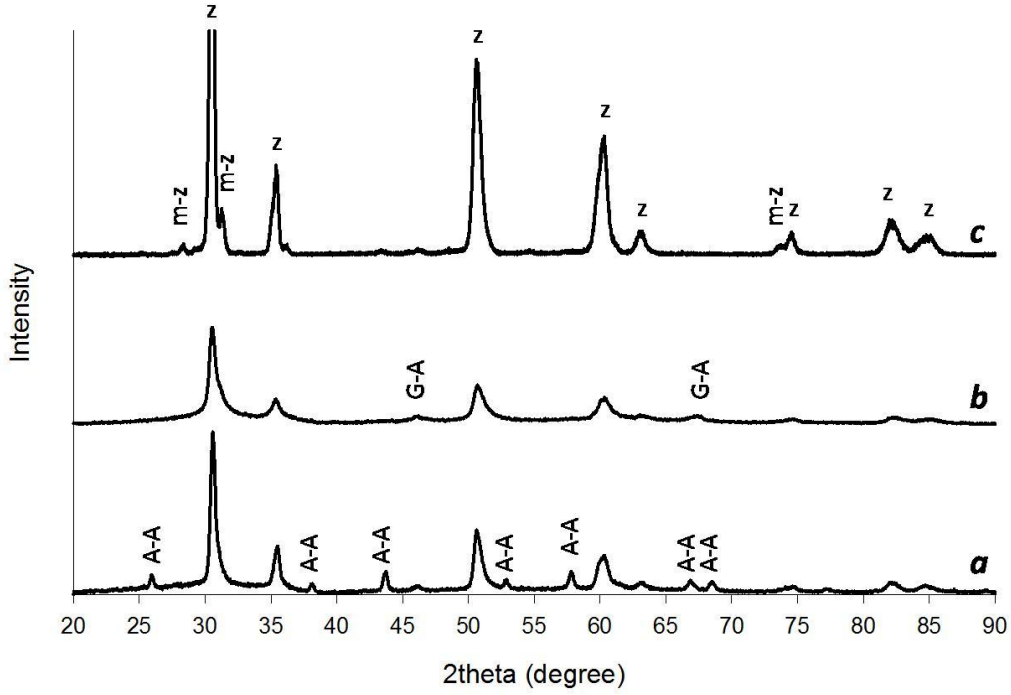

Figure 5-14 XRD pattern of: a) typical pattern of the coatings sprayed with system 1; b) coating of powder #3 deposited with system 2; c) coating of nano-powder of 8 wt% YSZ; where z represents the cubic (or t' zirconia), m-z is monoclinic zirconia, G-A shows γ alumina peaks and A-A is α-alumina.

The amorphous humps in these patterns are apparent in Figure 5-15, which shows the XRD pattern of the coating of nano-powder deposited with system 2. They are centered at angles of about 30° and 57° that are the locations of the maximum intensity peaks for zirconia and the second maximum (91% intensity) of α-alumina, respectively. It is known that the maxima of the amorphous humps of each material are located at diffraction angles where the peaks with maximum intensity of its crystalline structure occurs [125]. Therefore, these locations of amorphous hump peaks imply that the amorphous phase within the coating is parented by zirconia and/or alumina. It is noticeable that the first maximum of α-alumina (at 35°) is overlapping with the first zirconia hump.

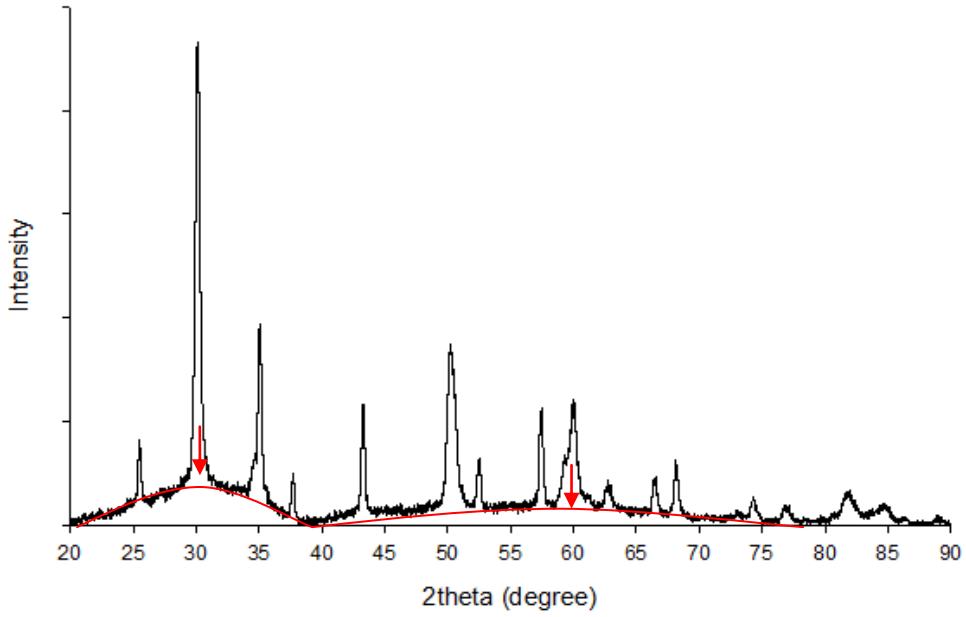

Figure 5-15 XRD pattern of the coating of nano-powder 60 alumina-40 (8 wt% YSZ) deposited without atomization showing the location of amorphous hump maximums

It is known that the variation in lattice parameter of solid solutions can represent the variation in concentration of the solute atoms [98]. On the other hand, as observed in this work on plasma spray processes, it can be presumed that the amount of amorphous phase

is directly related to the mixing proportion. Therefore, an assessment of the lattice parameters among the coatings with various amorphous contents was done. The assessment was undertaken to find out if the solubility, measured by lattice parameter, is related to the amorphous content resulting from extensive mixing. The relationships between the amorphous content and the lattice dimensions in the crystalline portion of the coatings are depicted in Figure 5-16.

Figure 5-16(a) demonstrates the variations of parameter *a* for the cubic lattice of zirconia with the amount of amorphous phase. It shows that by increasing the amorphous content as a result of improved mixing, the lattice parameter of cubic zirconia increases. This suggests the enhancement of dissolution of the solute atoms in the crystalline structure of stabilized zirconia. The horizontal line in this figure represents the lattice parameter (a = 5.1177 Å) of the stabilized zirconia with no alumina added deposited under the conditions set out in Table **5-4**. It can be seen that at lower amorphous content that can be translated to less dissolution, the lattice parameter is smaller than YSZ; but at high dissolution ratios it grows beyond the YSZ (with no dissolved alumina). This can be explained by changes in solute atom position in the lattice. Thus, when the aluminium takes the substitutional positions of the YSZ crystal, it causes the lattice to shrink. At higher amounts of dissolution, considering the much smaller radius of the aluminium (1.18 Å) atoms than zirconium (2.06 Å) and yttrium (2.12 Å), the zirconia structure may choose the interstitial positions for the solute to reduce the distortion and the related strain energy. Thus, allocation of the remaining aluminium atoms in the interstitial position results in expansion of the lattice.

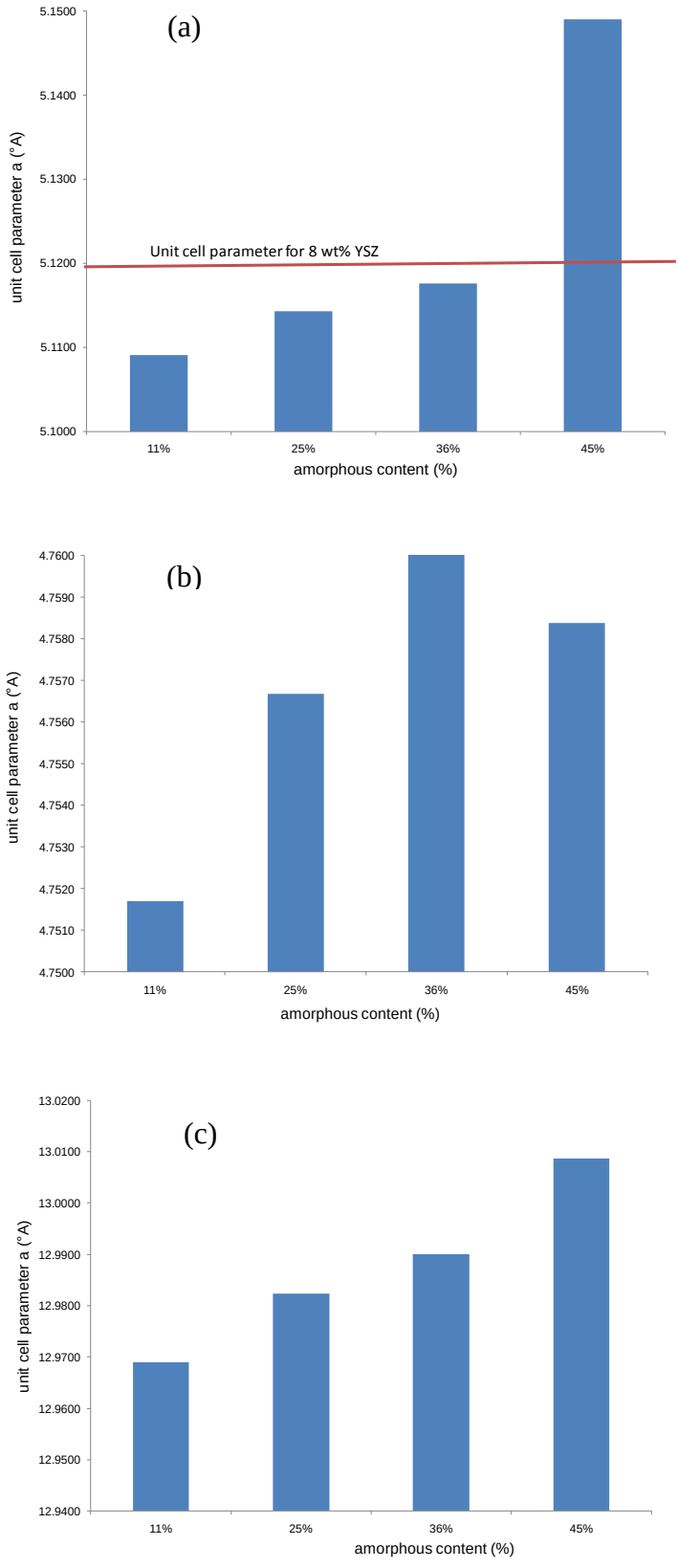

Figure 5-16 Lattice parameters of the crystalline portion of the coatings: a) parameter *a* for cubic zirconia; b) parameter *a* for α-alumina; c) parameter *c* for α-alumina

Assessment of the α-alumina structure with the two parameters *a* and *c* reveals that the same approximate increasing trend is followed, as is apparent in Figure 5-16(b) and (c). This means increased amorphous percentage is concurrent with the larger lattice parameter as a result of extended solubility. Zirconium atoms with a much larger atomic radius than aluminium cause the expansion of the alumina lattices by forming substitutional solid solution. This solubility sometimes is as high as supersaturation, as found in Chapter 3. Thus, the disappearance of the alumina component when sprayed with zirconia can be not only the result of amorphous phase formation; the extended solid solubility into zirconia during plasma spray deposition also plays a major role.

However, the large atomic number difference between aluminium and zirconium that can shadow the detection of small amounts of free crystalline alumina should not be ignored [98]. This happens when in a system of elements A and B, in two-phase region (e.g., α+β, where α and β are solid solutions of A with solute atom B and B with solute atom A, respectively) the atomic number of one type of atoms (e.g., A) is too small compared with the other element (e.g., B), the intensity of A remains undetected (a difference of more than 70 in atomic number can prevent detection of up to 50 wt% of α-phase) [98]. Accordingly, the oxides of these elements can show the same behaviour. This means that small amounts of crystalline alumina in the system may exist, but due to low intensity of the scattered beams of aluminium compared with heavy (large atomic number) zirconium and yttrium atoms, are not detected.

A summary of the results in this section includes the following. The in-flight collected particle studies suggest that there are major similarities between APS and SPS processes in terms of melting, mixing and phase formation as well as the effective parameters on

these phenomena. However, the fragmentation of the particles in APS is not considerable as compared with SPS. As a result, while this work has focused on the parameters in SPS, both methods can be used in production of high amorphous coatings using similar roles for the corresponding parameters. In this section it was revealed that in-flight melting followed by mixing are crucial processes in amorphous formation. The observed role of the lower particle velocity that results in higher amorphous content, in spite of the lower cooling rates, was justified. This means that the significance of the in-flight particle velocity is due to its effect on longer melting and mixing times.

The amorphous phase in the coating seems to be composed of two compositional ranges. One is with high alumina and the other with high zirconia. This was concluded from the amorphous humps maxima which matched the locations of the crystalline peaks with maximum intensity of alumina and zirconia. On the other hand, the crystalline structures present an exceptionally extended solubility of both the components, especially alumina into the zirconia lattice. The lattice parameter studies suggest that the aluminium atoms possibly take the substitutional sites at low ratios and interstitial sites when higher amounts of alumina are being dissolved in zirconia. In contrast, large zirconium atoms have no choice but substitutional positions during dissolution in alumina structure, resulting in ever increasing the lattice parameters of alumina by dissolution ratio. The components in the composite materials sprayed by plasma processes may form crystalline structure of alumina or YSZ with no additional solute atoms than what they already had, dissolve the solute atoms of the second or more components and form crystalline solid solutions (even to exceptionally high levels of solubility), and/or form amorphous phase.

5.4. Summary

It was observed in the SPS process that, for the development of the amorphous phase in the coatings, extremely small nano-particle feed is not necessary. Conversely, it is a powder size of a few microns that provides larger amounts of the amorphous phase. Other spray parameters that can enhance this phase are higher robot speed, fewer deposition passes and preheating the substrate. Particle velocity also plays an important role in the amorphous content of the coating, such that a lower velocity caused higher amorphous content. In contrast, particle temperature plays a negligible role in the amorphous phase formation (as long as it is above the melting point of the components). However, when the particle temperature is too high, it can reduce the amount of the amorphous phase.

The key to amorphous formation in plasma spray of multi-component systems such as alumina-YSZ composite, consisting of insoluble components in solid state, is their mixing in molten state. The amorphous phase can be parented by either alumina or zirconia, depending on the mixing ratios within the splat. When the well-mixed melt does not solidify in the amorphous phase, it can form crystalline solid solution within the saturation limit or in supersaturated condition.

Chapter 6 Thermal Evolution and High-Temperature Performance of the Mixed Amorphous/Crystalline Structure

This chapter involves evaluation of the thermal and mechanical behaviour of the composite coating of interest (pseudo-eutectic alumina- 8 wt% YSZ) in the presence of amorphous phase. It investigates the roles of the amorphous phase in as-deposited coating, as well as the properties of the coating after heat treatment.

6.1. Crystallization and Phase Transformation Temperatures versus Amorphous Content

One question that this research was to address is the role of the amorphous phase content on the crystallization and consequent transformation temperatures in the composite coating. Figure 6-1 represents the two main transformation temperatures versus crystallization peak area (representing amorphous content) extracted from DSC curves. The crystallization temperature in this diagram varies in the range of 951-956°C while the crystallization peak area ranges from 2 to 152 units. As can be seen, the variation of crystallization temperature is not affected by the amorphous phase content. This observation contradicts the proposition by Kim et al. [24] about the probable importance of the amorphous content on crystallization temperature in this composite, causing discrepancy in different reports. In these reports, the composites were produced with different processes and impurity contents. Therefore, the sources for the differences in the

crystallization temperatures may be referred to the production processes and/or the impurities.

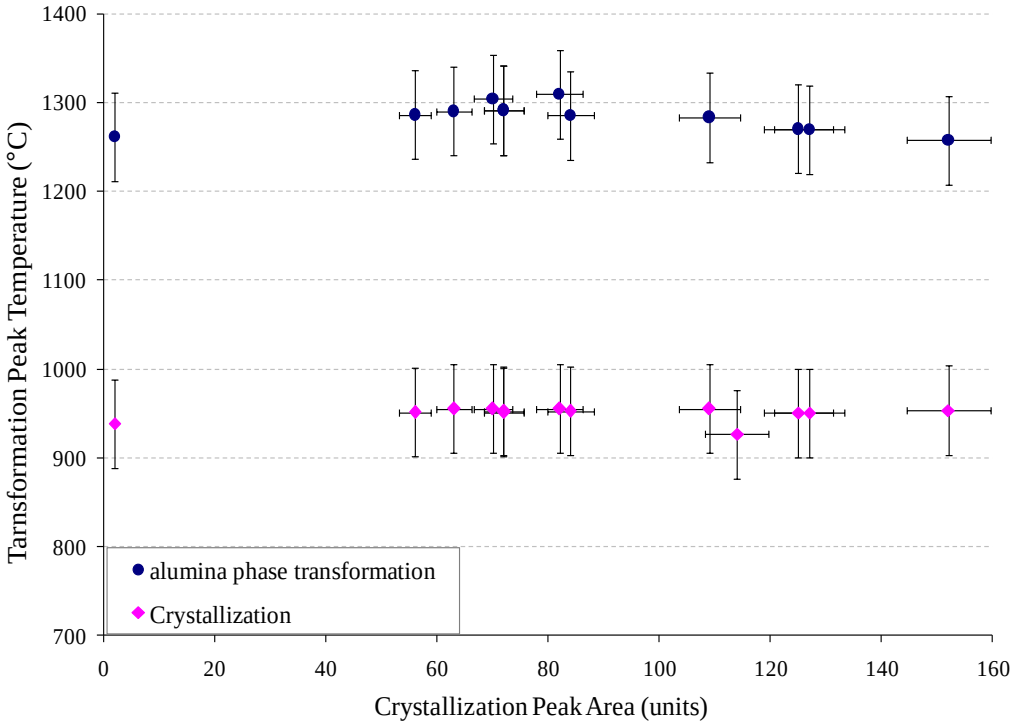

Figure 6-1 Transformation temperatures versus crystallization peak area, showing that neither crystallization temperature nor the γ- to α-alumina transformation temperatures are affected by the amorphous content

In the same range of amorphous content, the transformation temperature of γ- to α-alumina, changes between 1258 and 1310°C. Although this is not a negligible change, dependency between this transformation temperature and the amount of amorphous phase is not apparent.

6.2. Crystalline Structure Changes after Heat Treatments

The variation of the coatings' crystalline structure after 400°C/8 hr, 700°C/24 hr, 1000°C/10 hr, 1300°C/24 hr and1500°C/5 hr heat treatment were studied. Heat treatments at 400 ºC for 8 hours and 700 ºC for 24 hours were done to investigate if the

diffused peak in the DSC curve includes any residual stress energy relief. XRD pattern of the resulting coatings presented no peak shift; this suggests that the diffused peak in the DSC graph does not involve any considerable residual stress relief. However it was seen that in case of highly crystalline coating, after both heat treatments some peak sharpening happened due to grain growth, while the peaks in the high amorphous samples showed no visible change.

Crystallization heat treatment at 1000°C for 12 hours in the highly crystalline coatings caused almost no crystallographic changes. In amorphous containing coatings with 35% and 53% amorphous content some reduction in amorphous humps could be considered, but the humps did not fully disappear after 10 hours and the calculated amorphous content reduced to about 24% from 53% amorphous and to 21% from 35% amorphous content. This observation shows that the crystallization, as a diffusion-controlled process, is time dependant. Later results from thermal cyclic tested samples in section 6.8.2 confirm this observation by showing that the crystallization has been completed in the samples after many heating cycles at the same temperature, when the time is long enough for the completion of the crystallization process.

In the sample used for heat treatment at 1300°C for 24 hours, the initial crystalline structure in high amorphous sample (with about 64% amorphous) in Figure 6-2 (a) consists of α-alumina and cubic zirconia. The presence of some tetragonal pattern closely similar to cubic phase cannot be denied. The highly crystalline structure in Figure 6-2(c) (with about 11% amorphous) is composed of both α- and γ-alumina and cubic zirconia in as-coated condition. The comparison of this pattern with that of the coating heat-treated at 1300°C for 24, hours shown in Figure 6-2 (b) and (d), suggests that in both structures

α-alumina is the only alumina phase present in the coating. The difference is in the YSZ dominant phase, which in the case of the heat-treated highly amorphous structure in Figure 6-2(c) presents some tetragonal structure (revealed by peak splitting at angles between 34°-35° and 59°-60°). It suggests that the amorphous phase should have crystallized in the form of tetragonal mainly by releasing the dissolved alumina as the stabilizer of high-temperature cubic phase. In contrast, in the highly crystalline coating after the same heat treatment in Figure 6-2(d), the metastable cubic YSZ solid solution is still the dominant phase.

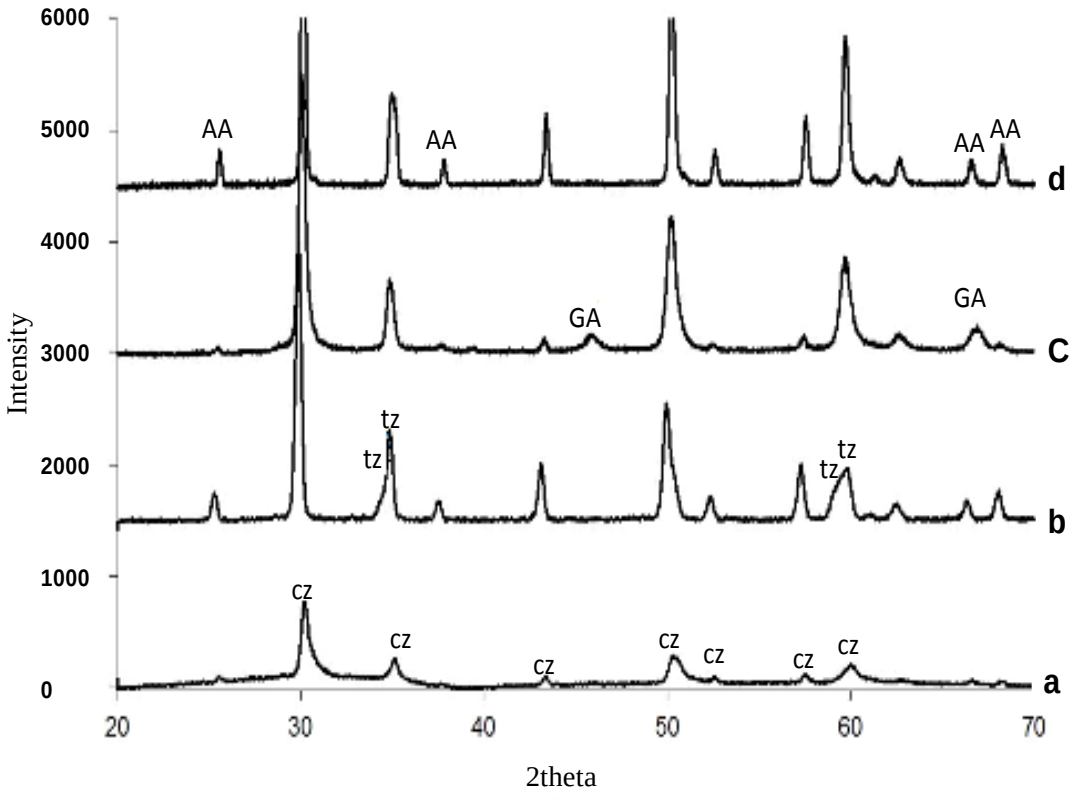

Figure 6-2 Comparison of crystalline structure of heat-treated coatings with fully crystalline and highly amorphous coating: a) coating with 64% amorphous; b) 64% amorphous coating heat-treated at 1300°C for 24 hrs; c) highly crystalline (11% amorphous) coating not heat-treated; d) same as c after heat treatment at 1300°C for 24 hrs

Further heat treatment at 1500°C for 5 hours to investigate the possibility of monoclinic zirconia phase formation showed that except for some grain growth, in any of the structures traces of this phase could not be found. Conversely, formation of monoclinic in 8YSZ (8 mol% equal to 13 wt% yttria stabilized zirconia) has been reported at 1400°C [117]. This proposes that the very high temperature stability of the composite against martensitic transformation of tetragonal to monoclinic zirconia is due to the added stabilizing effect of alumina to that of yttria.

In addition to the coatings with high amorphous content, the composite in the crystalline as-coated sample shows the high stability of the cubic solid solution of YSZ even at temperatures as high as 1500°C. These results support the role of alumina as a stabilizer through extended solubility in the zirconia.

6.3. Microstructural Changes after Heat Treatments

The microstructures of the coatings after heat treatments of 1000°C/10 hrs, 1300°C/24 hrs and 1500°C/5 hrs has been investigated. In Figure 6-3, the microstructures of the as-deposited coatings with high amorphous content (that has appeared as extensive grey areas in Figure 6-3(a)) and coatings with low amorphous content (with distinctive black and white regions in Figure 6-3(b)) are shown. The crystallization heat treatment for 10 hours at 1000°C did not end with any visible change in the coatings' microstructures. However, after heat treatment at 1300°C for 24 hours, the two coatings can be compared in Figure 6-3(c) and (d). It can be seen some spotty areas that are formed of precipitation of alumina and zirconia as a result of crystallization of the amorphous phase. Therefore, there are clearly more spots (precipitates) formed in the case of high amorphous structure.

These precipitates are typically of minimum 50 nm size. Heat treatment at higher temperatures of 1500°C for 5 hours, as visible in Figure 6-3(e) and (f), shows the growth of precipitates as well as commencement of some spheroidization of the splats in the form of round corners and thickened splats.

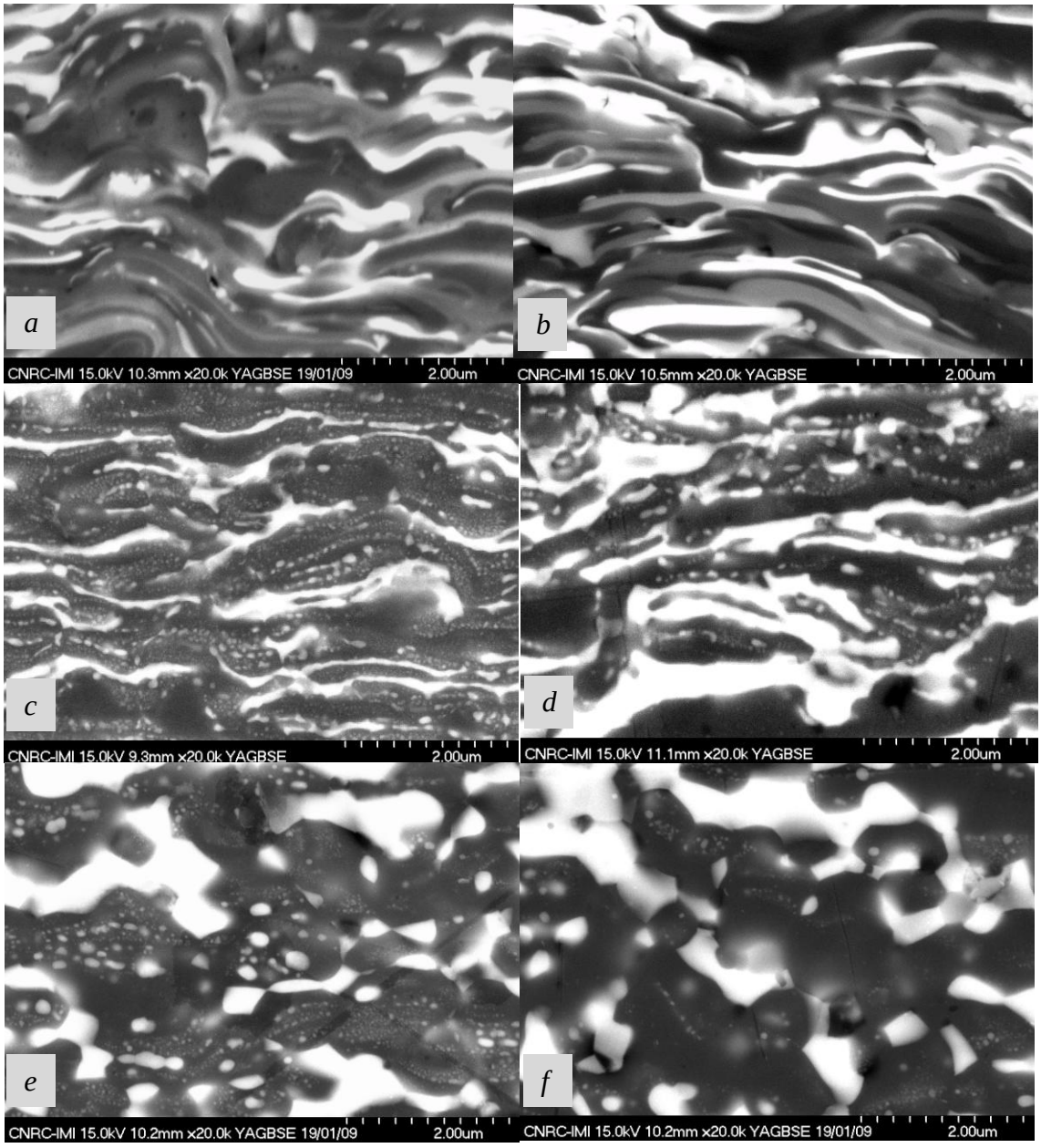

Figure 6-3 Microstructure of: a) as-deposited high amorphous coating; b) as-deposited low amorphous coating; c) high amorphous coating heat-treated at 1300°C/24 hrs; d) low amorphous coating heat-treated at 1300°C/24 hrs; e) high amorphous coating after 1500°C/5 hrs; f) low amorphous coating after 1500°C/5 hrs

6.4. Grain Sizes after Heat Treatment

The grain sizes of the crystalline phases have been measured after 1000°C/10 hrs, 1300°C/24 hrs and 1500°C/5 hrs and compared with the as-coated condition. Figure 6-4 shows the grain sizes of different phases present within the coating before and after crystallization heat treatment. In this figure, the coatings with high crystallinity (less than 11% amorphous phase), high amorphous (45% amorphous phase) and intermediate amorphous content coatings (with 23% amorphous) are compared with each other.

It can be seen that in high crystalline coating upon heat treatment the average grain size increases for all phases including α-alumina, γ-alumina and cubic or tetragonal zirconia. In contrast, upon crystallization heat treatment of high amorphous coating, the average grain sizes of α-alumina and zirconia decrease. The γ-alumina initially absent in this coating appears with the smallest grain size by crystallization from amorphous phase. In addition, the intermediate amorphous coating shows a slight grain-size reduction in all phases. Since the initial crystalline grains enlarge due to heat treatment, this reduced average grain size has to be due to crystallization of the amorphous structure. This means the crystallized grains from the amorphous phase form in much smaller sizes than what was formed during plasma spray deposition (rapid solidification). So that, despite grain growth in crystalline grains, the average grain size after crystallization is decreasing as compared with the as-deposited state; and this decrease is linked to the amorphous content.

It is known that the grain size of the crystalline structure grows upon heating and increased atomic mobility and diffusion. On the other hand, the crystallization of

amorphous phase as a solid state transformation provides a shorter free path and mobility for the atomic diffusion. This is expected to result in smaller grain sizes than crystalline grains formed out of liquid state during solidification. The observed smaller grain size of γ-alumina from crystallization process (in 45% amorphous coating) than that formed in as-deposited coatings (even though at very high cooling rates) supports this fact. The final grain size of crystalline/amorphous structure upon crystallization is a compromise between two phenomena: the growth in the crystalline grains and the formation of nano-sized grains crystallized from amorphous phase with smaller grain size than the as-coated grains. As a result, it can be seen that by increasing the amorphous proportion of the structure, crystallization heat treatment brings about smaller average grain sizes. It can thus be said that transformation from amorphous phase can be thought of as an effective way for nanostructure production.

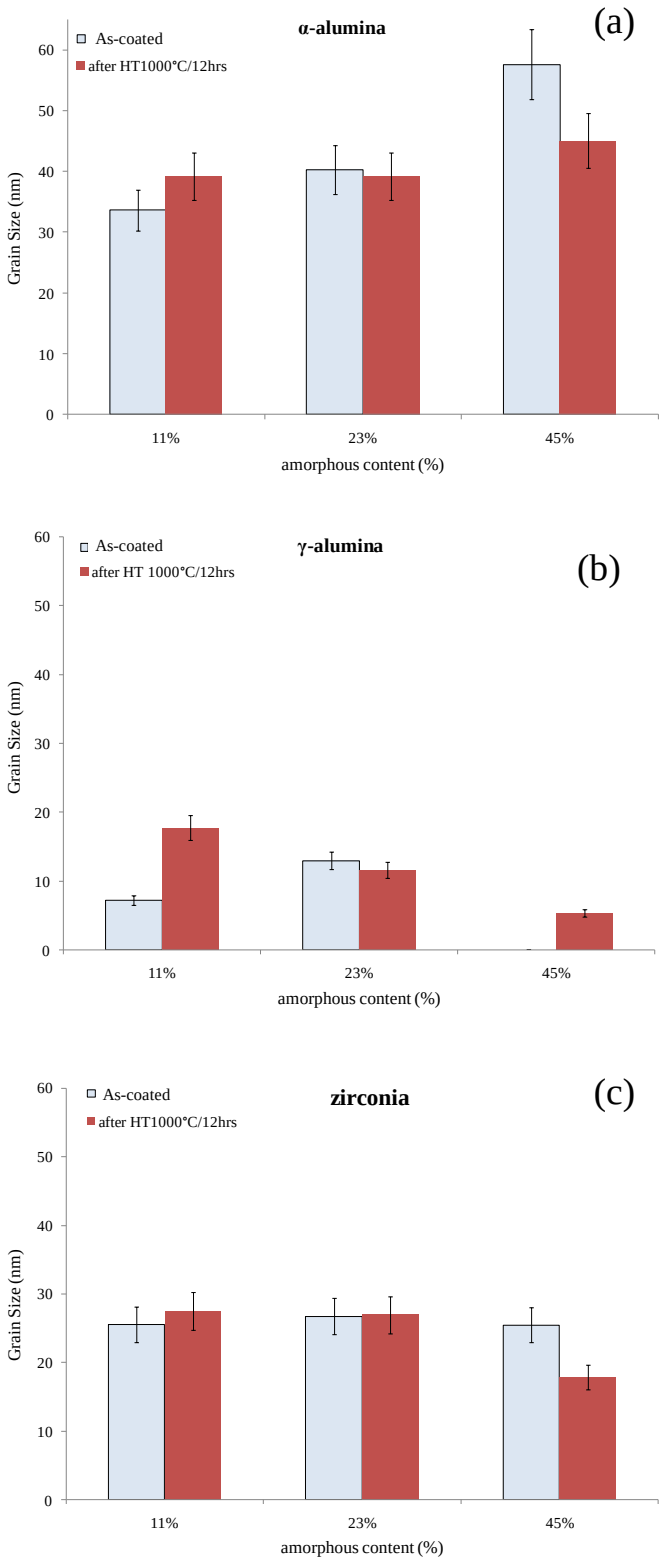

Figure 6-4 The role of amorphous content on grain size changes during crystallization heat treatment for a) α-alumina, b) γ-alumina, and c) zirconia

Further heat treatment at 1300 ºC for 24 hours resulted in grain growth of both crystalline and high amorphous coatings with a considerably higher rate in crystalline coating. The grain size of the as-coated and the heat-treated samples are summarized in Table **6-1**. It shows that in high crystalline coating the grain sizes of zirconia and α-alumina starting at 23 nm and 34 nm, respectively, grow to the extent that the XRD evaluation method (using the equations 2-4 and 2-5 in section 2.5.3) with limited accuracy to the maximum grain sizes of about 100 nm [98] cannot yield the grain size (results in square root of negative number, because of the peak width *b* being smaller than machine broadening *β*). These cases are marked as "> 100nm" in Table **6-1**. In addition γ-alumina, initially smaller than the two other phases, has entirely transformed into α-alumina. On the other hand, the grain growth in high amorphous structure is clearly less than high crystalline coating. As Table **6-1** presents, zirconia grew from 19 nm to 40 nm and γ-alumina transformed to α-alumina (initially absent in the coatings) that appears with 53 nm grain size.

Table 6-1 Role of amorphous content on grain growth during heat treatment

Amorphous content (%)	As-deposited coating			After heat treatment at 1300°C/24 hrs		
	Zirconia (nm)	γ-alumina (nm)	α- alumina (nm)	Zirconia (nm)	γ-alumina (nm)	α- alumina (nm)
11%	23	13	34	> 100nm	non	> 100nm
45%	19	9	non	40	non	53

After heat treatment at 1500 ºC for 5 hours, the method cannot determine the grain sizes of the present crystalline phases (i.e., zirconia and α- alumina) due to excessive enlargement that causes the width of the peak to be less than the machine broadening.

However, since the size limitation for this method of grain size measurement is 100 nm, it is clear that the grain sizes have been larger than this limit.

6.5. Mechanical Properties before and after 1000°C/10 hrs Heat Treatment

6.5.1. Hardness

The micro-hardness measurements on the coatings with different amounts of amorphous phase before and after heat treatment are summarized in Figure 6-5. It is evident that higher amorphous coatings are basically of lower hardness than the crystalline structures. Upon crystallization heat treatment the high crystalline structure shows some decrease in hardness due to observed grain growth while crystallization of the amorphous phase into even smaller grains has enhanced the hardness of the high amorphous coatings.

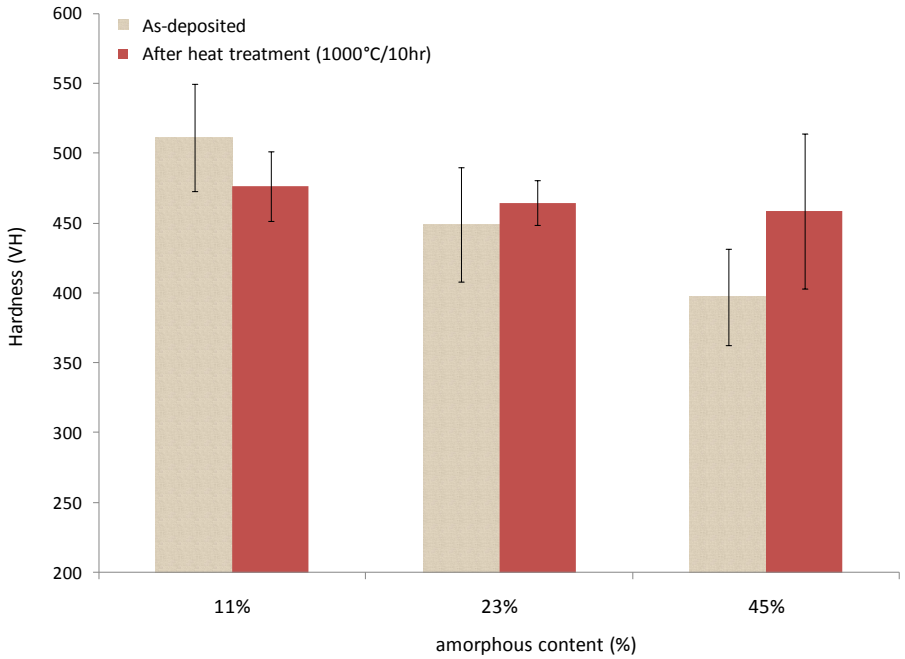

Figure 6-5 Hardness measures before and after crystallization heat treatment for different amorphous coatings

Comparison of the increase in the hardness of the samples with 23% and those with 45% amorphous phase shows that the increase in the hardness is larger at higher amorphous content. This should be again due to the larger decrease in the mean grain size at higher amorphous contents. Eventually, after crystallization heat treatment, the hardness for all coatings with any amorphous content approaches a similar limit, as shown in the same figure.

6.5.2. Fracture Toughness

Figure 6-6 shows the results of fracture toughness measurements based on the crack lengths initiated under specific load during indentation. The fracture toughness of the higher amorphous coating is initially lower due to brittle behaviour of the amorphous phase. The brittleness of the coating with high amorphous content is illustrated in Figure 6-7. This figure is the micrograph of an indent resulting from hardness testing. The area under the indenter shows a glass-like fracture with drastic crack propagation. Upon heat treatment at 1000°C for 12 hours when crystallization has been partly accomplished, both coatings present lower fracture toughness. This decrease can be explained according to the formula used in calculation of the fracture toughness (Equation 2-1 in section 2.3.2) where the higher hardness can yield smaller values of fracture toughness. In this case, the increased hardness values will be responsible for reduced fracture toughness results after heat treatment.

The fracture toughness of 8 wt% YSZ is considerably lower than that of alumina-8 wt% YSZ composite coating. Crack propagation in the monolithic structure of stabilized zirconia with very limited inter-splat boundaries, (as the micrograph in Figure 5-13(f) presents), is easier than crack propagation in composite with a large number of inter-splat

boundaries that act as crack arresters. Heat treatment of such a coating, as can be observed in Figure 6-6, results in more reduction in fracture toughness for more sintering and elimination of inter-splat boundaries [126].

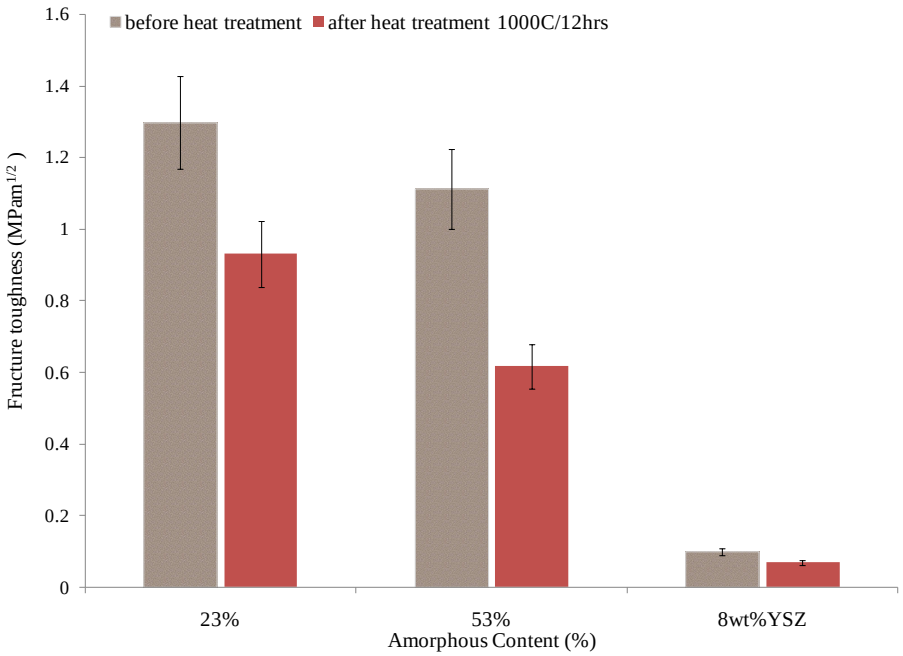

Figure 6-6 Fracture toughness in coatings with different amorphous content, before and after heat treatment at 1000°C/12 hrs

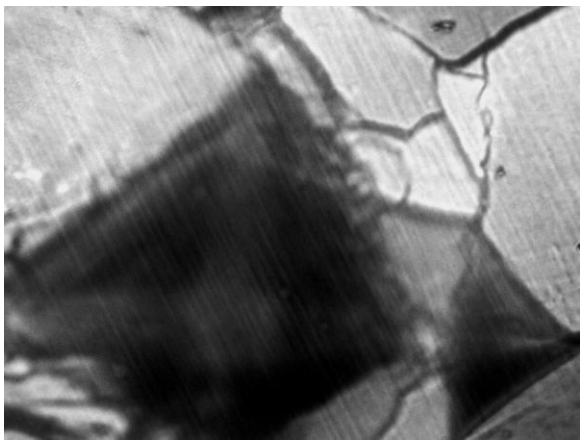

Figure 6-7 Brittle fracture of 55% amorphous coating under indentation

6.5.3. Erosion

Erosion rate of the two coatings with 36% and 53% amorphous are shown in Figure 5-8. It can be seen that the higher amorphous material illustrates a larger erosion loss. As the hardness tests prove, the higher amorphous coatings are softer. The studies on the erosion mechanisms suggest that at high obliquity of the impinging erodent particles, as here, the softer ceramic material behaves like metals where the material erodes more rapidly at lower hardness [127].

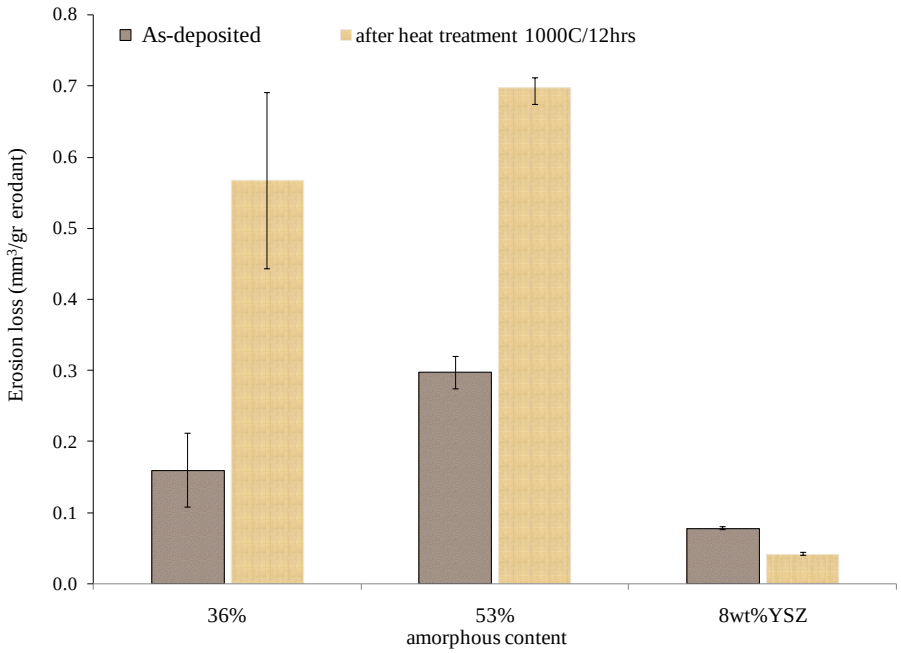

Figure 6-8 Erosion losses in two different amorphous coatings before and after heat treatment at 1000°C/12 hrs and comparison with YSZ coating with the same process

After heat treatment at 1000°C for 12 hours, the erosion rate of the coatings has increased. This can be attributed to the sintering of the columnar grains in this structure. Figure 6-9 (a) and (b) show the fracture surfaces of such a coating before and after an almost similar heat treatment i.e., 1000°C for 10 hours. In Figure 6-9(a), the columnar grains formed in the coating resulting from SPS deposition of the alumina-YSZ

composite can be seen. Figure 6-9(b) shows the same structure after heat treatment. In this figure, the annihilation of the columnar grains and the spaces between them is clear. Densification of the columnar grains in YSZ helps rapid growth of the lateral cracks and material removal during particle impingement in erosion test [127]. However, the importance of such densification in the composite coating with splats of different materials may need more detailed investigation.

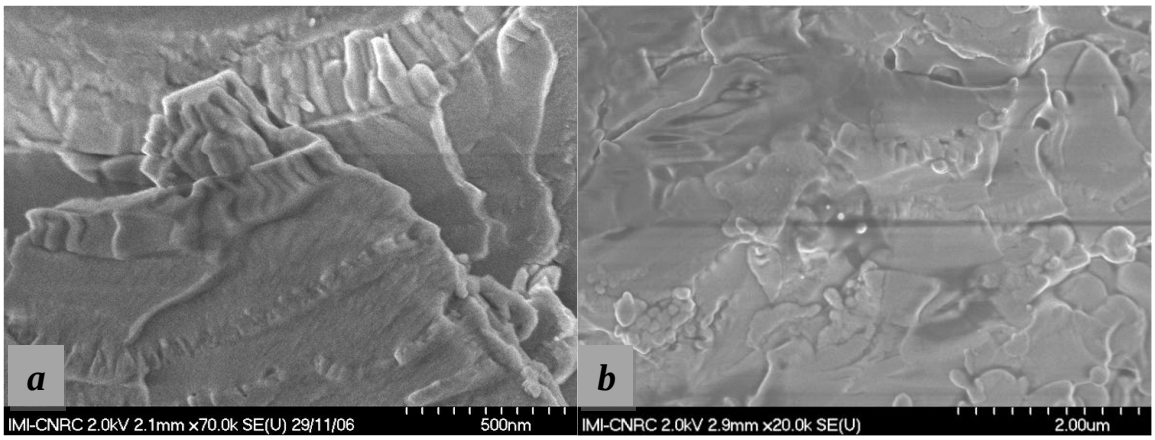

Figure 6-9 Fracture surface of alumina-YSZ coating deposited by SPS process: a) before; and b) after heat treatment at 1000°C for 10 hours showing annihilation of columns and sintering of the structure

The monolithic structure of 8 wt% YSZ, however, shows much higher erosion resistance compared with the composite coating of alumina-YSZ. The dense uniform structure of this coating, with considerably fewer structural defects found in the corresponding micrographs, predicts superiority in erosion behaviour. In contrast to the composite coating, in this sample more reduction in erosion loss was observed after 1000°C for 12 hours, and can be attributed to the ceramic densification by elimination of the porosities and inter-lamellar cracks due to sintering [128], as denser ceramics are known to be of higher erosion resistance [10].

6.6. Mechanical Properties before and after 1300°C/24 hrs, 1500°C/5 hrs Heat Treatment

6.6.1. Hardness

It is shown in Figure 6-10 that in highly crystalline structure the hardness is initially higher than in high amorphous structure. It remains almost unchanged in crystalline structure while in more amorphous coating it considerably increases by heat treatment at 1300°C for 24 hours due to the presence of precipitates that, as discussed in section 6.3, have enlarged during heat treatment to an effective size, improving mechanical properties.

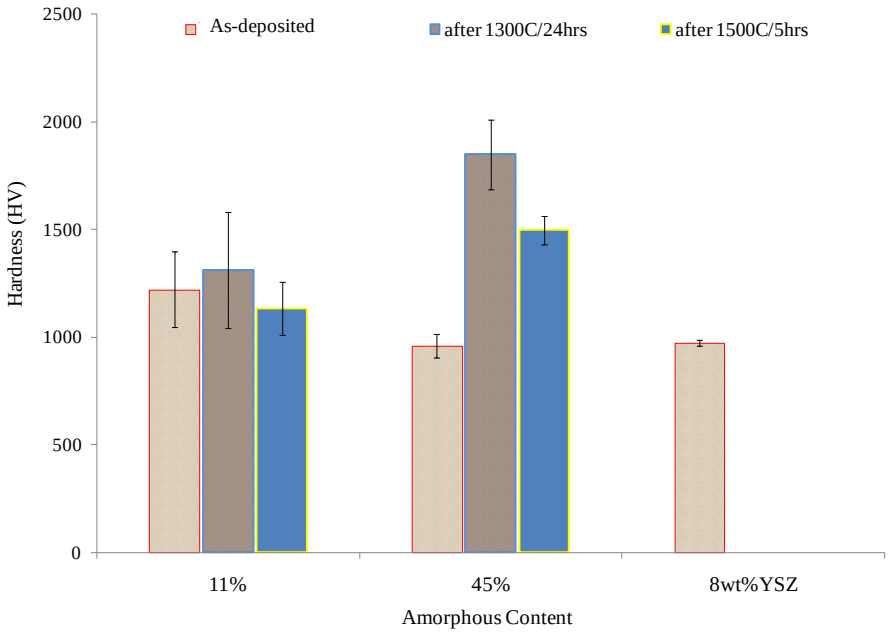

Figure 6-10 Comparison of the hardness variation with heat treatment between two samples with low and high amorphous content and their comparison with the 8 wt% YSZ

After heat treatment at 1500°C for 5 hours, the hardness decreases due to grain growth as well as over-aging by additional enlargement of the precipitate size. Yet, this hardness is higher than that of the crystalline as-deposited coating. Thus amorphous phase initially

lowers the hardness but upon heat treatment it increases the hardness due to smaller average grain size, as well as sintering and densification. The hardness of 8 wt% YSZ is shown to be lower than that of alumina-8 wt% YSZ composite. The difference, however, is lower than what the rule of mixtures for 60% alumina dictates. This is because of the structural defects frequently observed in the composite coating, such as the solid particles in the coating resulting in loose splat bonding. It can be said that these defects prevent the material from presenting its potential mechanical properties.

6.6.2. Fracture Toughness

Figure 6-11 summarizes the variation of fracture toughness as a measure of resistance to crack growth under specific load. In this figure, a coating composed mainly of crystalline structure (less than 11% amorphous) is compared with a high amorphous content coating (45% amorphous) in as-coated condition and after heat treatments.

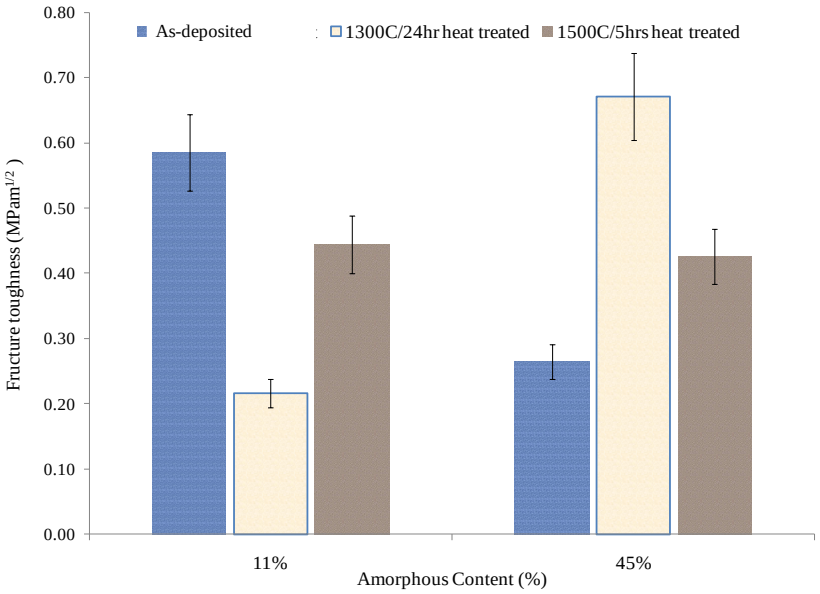

Figure 6-11 The role of amorphous content on fracture toughness before and after heat treatments at 1300°C/24 hrs and 1500°C/5 hrs

The high amorphous coating is initially of lower fracture toughness than the crystalline coating. Upon heat treatment at 1300°C for 24 hours, the crystalline coating experiences a considerable decrease in fracture toughness, while under the same conditions in the high amorphous coating fracture toughness drastically increases. The reason for this can be found in the observed microstructures in section 6.3, where the heat treatment at 1300°C for high amorphous coating results in a large amount of uniformly distributed precipitates. By contrast, according to section 6.4, the crystalline structure faces noticeable grain growth.

Finally, after heat treatment at 1500°C for 5 hours both structures behave similarly. This heat treatment, as discussed in section 6.3, leads to similar microstructures for both samples. In addition, over-aging the precipitates impairs the fracture toughness property [129]. It should be noticed, however, that the fracture toughness is calculated based on the *E* and *H* that are in turn functions of porosity [11], intersplat bond [90,130] and phase analysis. Hence, the fracture toughness will be a compromise of these variables.

6.7. Thermal Conductivity Changes before and after Heat Treatment

Figure 6-12 represents the relation between thermal conductivity of the coatings before and after heat treatment, and the amount of amorphous phases. It is seen that before heat treatment thermal conductivity decreases when the amount of amorphous phase increases. According to the literature [131], there are two methods of thermal conduction. One is the electron transfer related to metals, and the other is the phonon transfer in non-metallic crystalline solids like ceramics. This means that in the absence of readily moving electrons to transfer the thermal energy, this energy is transferred by crystallite vibration.

In the amorphous-containing ceramics the second mechanism for heat transfer is also impaired, due to reduced mean free path of the phonon in amorphous phase. It is thus predictable to observe decreased thermal conductivity by increasing the amorphous phase.

Upon heat treatment at 1000°C for 10 hours crystallization can re-activate the photon transfer mechanism and increase the thermal conductivity. As can be seen in Figure 6-12, the heat-treated samples (except one) present higher thermal conductivity than the initial coatings. In addition, in the heat-treated coatings with high amorphous contents (after the exceptional point), thermal conductivity is increasing by the amorphous content. This can be attributed to the formation of higher amounts of tetragonal structure in high amorphous coatings, as discussed in section 6.2, compared with the more crystalline coating that mainly consists of cubic zirconia with lower thermal conductivity [132].

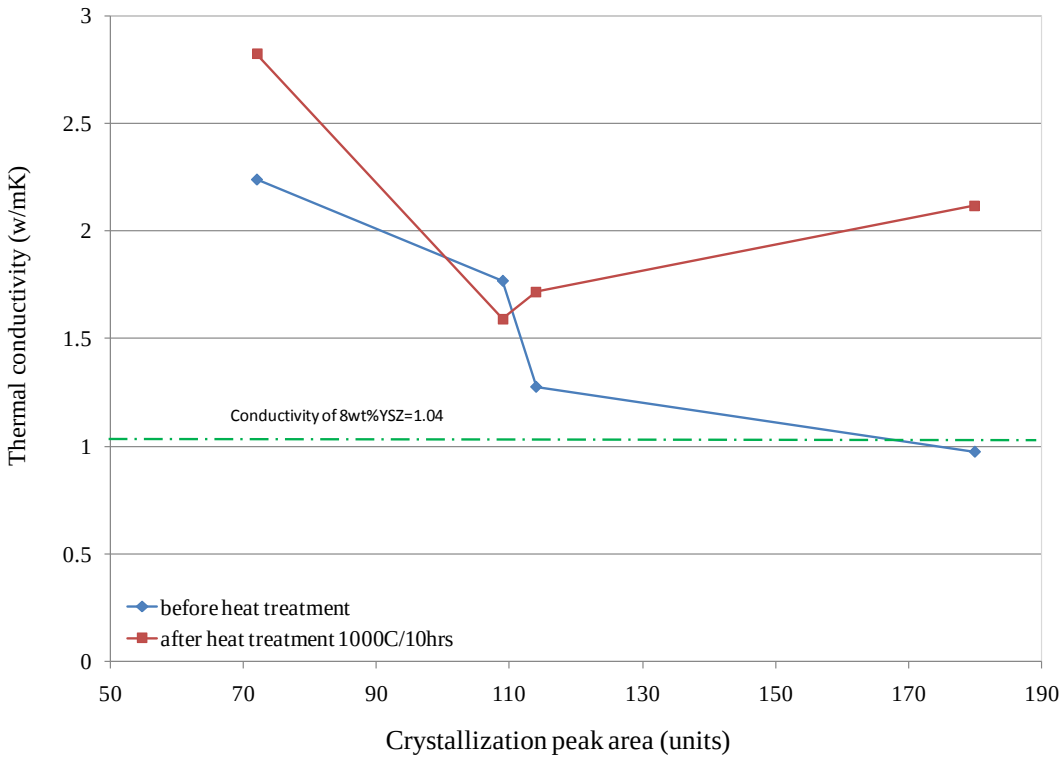

Figure 6-12 Thermal conductivity changes before and after heat treatment at 1000°C/10 hrs for coatings with various amorphous contents

The exceptional point, in a closer investigation of the microstructure, was related to the coating with a high number of tiny horizontal cracks, where the heat treatment caused their opening and reduced thermal conductivity. The decreasing role of amorphous phase in thermal conductivity is such that at higher amorphous contents (as in the last data point in Figure 6-12) the material yields thermal conductivity comparable to 8 wt% YSZ.

6.8. Thermal Cyclic Test

6.8.1. Thermal Cyclic Life

Figure 6-13 shows three coatings on Inconel 625 bound coated with NiCrAlY after thermal cyclic test, including two alumina-YSZ coatings with mixed amorphous/crystalline structure and one 8 wt% YSZ coating. The composite coatings differ from each other in their structure. The coating with 36% amorphous content (in Figure 6-13) is dense, with a microstructure similar to Figure 4-10(a), and the second composite coating containing 52% amorphous phase is porous, with a microstructure like in Figure 4-10(b).

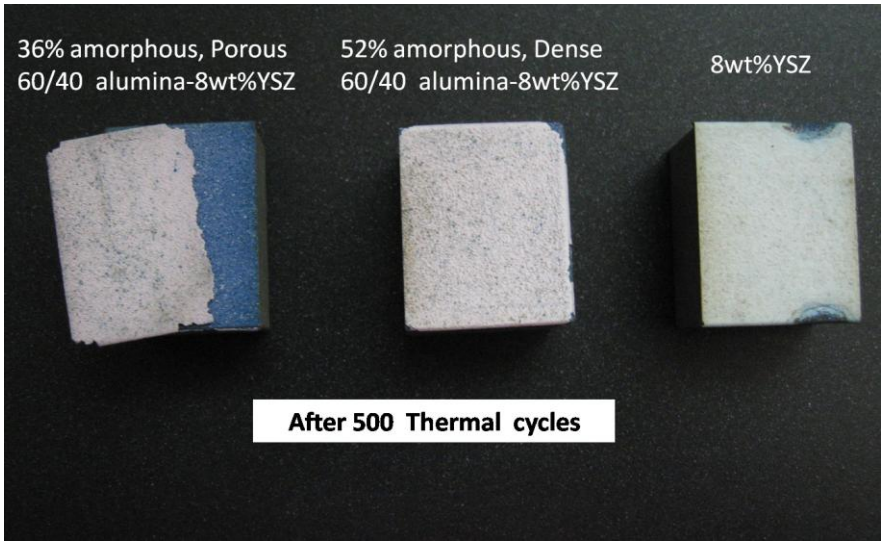

Figure 6-13 Thermal cyclic test samples after 500 cycles; left sample with 36% amorphous content, middle sample with 52% amorphous and right sample conventional YSZ coating

It was observed that during thermal cycling test, the high-porosity composite coating detached entirely in less than 20 cycles. By contrast, the dense coating of the same material was still attached after 500 cycles, which means it showed almost the same cyclic heat resistance as the conventional YSZ coating. Even though the higher amorphous content in this coating was expected to cause large volume change due to crystallization (as follows in the next section during heating cycles at 1080°C), it did not result in deterioration of the coating. This suggests that the material may have the potential for high performance in cyclic heat (performing at least as well as conventional YSZ), when it is dense with appropriate inter-splat bonding. However, the porous coating allows rapid oxidation of the substrate/coating interface and early detachment of the coatings in less than 20 cycles. The oxide layer rapidly thickened after 20 cycles can be seen in Figure 6-14.

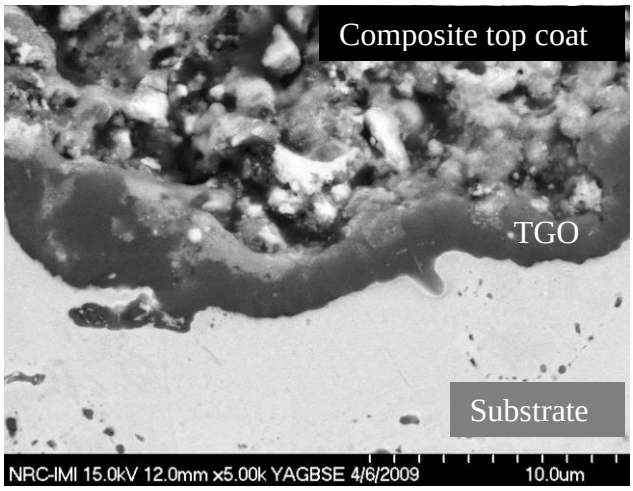

Figure 6-14 Sectioned view of the oxide layer in top/bond coat interface of a) the porous composite coating after 20 cycles

6.8.2. Structural Changes

Figure **6-15** illustrates the structural changes after 500 cycles of heating and cooling. Figure **6-15**(a) shows the XRD pattern of the high amorphous coating in the as-deposited condition. It consists of amorphous humps and the crystalline structure of cubic zirconia and γ-alumina. Long cumulative exposure time at cyclic heat has resulted in the crystalline pattern shown in Figure **6-15**(b). In this coating, the γ-alumina and the amorphous humps have disappeared and (α + δ)-alumina and (cubic + tetragonal) YSZ are the phases present in the coating after thermal cycling. This is somewhat different from the phases formed during heat treatment of the coatings at about the same temperatures in section 6.2. This shows that the phase transformations can be different in heat treatment than thermal cycling at the same approximate temperatures.

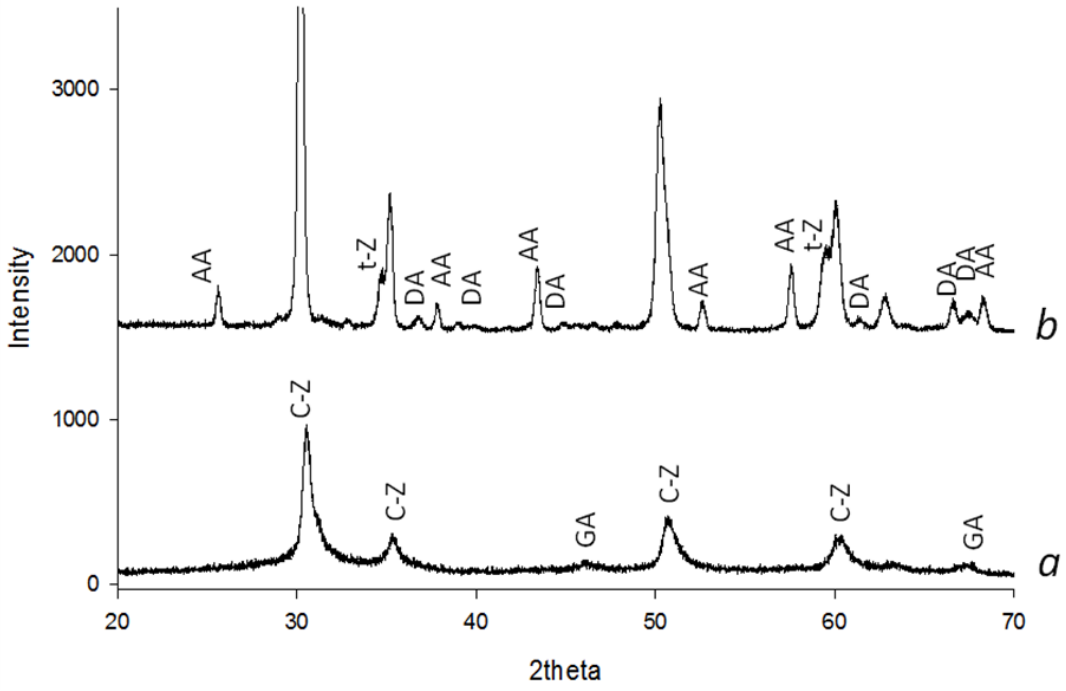

Figure 6-15 XRD pattern of high amorphous sample (48%): a) before and b) after 500 thermal cycles between room temperature and 1080°C, where C-Z denotes Cubic Zirconia; t-Z, tetragonal zirconia; AA, α-alumina; GA, γ-alumina and DA, δ-alumina

In addition, the appearance of α-alumina at such a low temperature is unexpected. It is in contrast with the results of heat treatment at 1000°C for 12 hours where no alumina transformation could happen and also contrary to the literature that predicts higher transformation temperatures. Thus, formation of α-alumina phases at such a low temperature can most probably be the result of crystallization of amorphous alumina.

Comparison of Figure **6-15**(a) and (b) shows the clear peak splitting at 59-60°, which means the tetragonal YSZ structure has become more dominant compared with the cubic phase after this cyclic heating at about crystallization temperature of this high amorphous coating. It is also notable that this composite did not show any formation of monoclinic zirconia even after 500 cycles, which suggests the high resistance of this material to

unfavourable phase transformation of zirconia phase in the pseudo-eutectic alumina-YSZ composite coating.

6.8.3. Microstructural Changes

Figure 6-16 presents the microstructural changes of the high amorphous coating after thermal cyclic procedure. Cyclic heating with high heating and cooling rates has changed the amorphous portion of the coating structure as in Figure 6-16(a) into the spotty morphology of Figure 6-16(b). The black spots in white background are the alumina precipitates in the zirconia background and the white precipitates in the black alumina surroundings are the zirconia released from the amorphous structure during its crystallization.

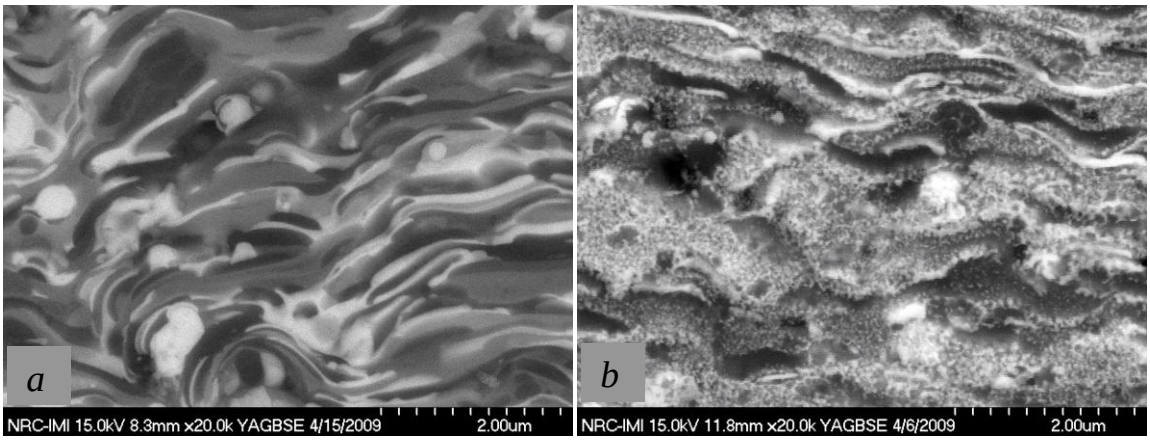

Figure 6-16 High amorphous (52 %) coating of alumina-YSZ composite a) as-deposited and b) after 500 thermal cycles up to 1080°C

This combined alumina structure with zirconia precipitates, so-called "zirconia toughened alumina" or ZTA, and the alumina precipitates in the zirconia structure known as "alumina hardened zirconia" or AHZ, is the interesting structure that was the last goal of this study. While ordinary heat treatment at about crystallization temperature proved unable to yield this kind of precipitate (at least within the time given for this process),

cyclic heat treatment could provide the goal of "multi-constituent" structure that may benefit both properties.

6.9. Summary

In this part of the study about the significance of amorphous phase, important findings were as follows.

The amount of amorphous phase did not show any effect on crystallization temperature and did not present any meaningful relation with the γ- to α-alumina transformation temperature.

Solid solution of cubic YSZ with alumina presents high temperature stability even at elevated temperatures as high as 1500°C.

Amorphous phase is an effective source of nano-crystalline structure with smaller and more stable grain sizes than what plasma spray can produce.

In terms of mechanical properties the pseudo-eutectic alumina-YSZ composite shows basically superior hardness and fracture toughness compared with the presently used 8 wt% YSZ TBC deposited with the same process. The material is, however, inferior in erosion resistance compared with 8 wt% YSZ.

In terms of the roles of amorphous phase on mechanical properties, it was found that:

a) Hardness of the amorphous-containing coatings is initially lower than that of crystalline coating. Crystallization results in similar hardness in both coatings. However, precipitation of zirconia in alumina matrix at 1300°C ends with an increase in hardness of the high amorphous coating, higher than in crystalline coating. However, after heat treatment at higher temperature (1500°C) the two materials show similar hardness.

b) Fracture toughness of the amorphous-containing coatings is initially lower than crystalline structure. Heat treatment at about crystallization temperature (1000 ºC) makes the situation worse for both crystalline and amorphous coatings. Fracture toughness in amorphous phase again experiences a great increase as a result of precipitation hardening after 1300°C heat treatment. Eventually both types of coating, after 1500°C, present similar behaviour.

c) Erosion loss in high amorphous coating is higher than in high crystalline coating.

Higher amorphous content reduces the thermal conductivity, and crystallization increases it. In addition, the coatings with larger amounts of amorphous phase upon crystallization heat treatment experience a greater increase in thermal conductivity due to crystallization of amorphous phase into tetragonal zirconia rather than cubic.

The composite coating under investigation shows a potential of thermal cyclic resistance at least equal to 8 wt% YSZ when the microstructure is integrated and with low number of defects. This composite also presents high thermal stability against formation of monoclinic zirconia.

The multi-constituent combination of ZTA with AHZ, as one goal of the project, was best achieved by cyclic heating at temperatures as low as 1080°C, where smaller grains can form. In addition, the phases formed during cyclic heating of the coatings may be different from what forms during heat treatments at constant temperatures at almost similar temperature.

Chapter 7 Conclusion, Main Contributions and Future Works

The major findings in this research are in three different areas: a) amorphous phase formation and its roles in the composite behaviour and properties; b) the SPS process and its comparison with APS; and c) the characteristics of the alumina-YSZ composite coatings as a TBC choice. Findings and contributions are summarized as follows.

7.1. Conclusions

- It was found that the amount of the amorphous phase does not change the crystallization temperature as according to literature it was suspected to. It does not affect the subsequent transformation temperatures (i.e., alumina phase transformation), either. However, the amorphous phase can decrease the thermal conductivity of the composite. In terms of mechanical properties, it reduces the hardness, fracture toughness and wear resistance in as-deposited coating. Nevertheless, upon heat treatment, the amorphous phase causes improved mechanical properties compared with crystalline coating.
- Two methods for amorphous formation were introduced. They include, first, the in-flight melting followed by mixing. This method is of major importance and involves the entire bulk of the molten particles. The second method which is of less significance happens upon impact of the molten particle. This method consists of remelting of the solidified splat of the low melting component

(alumina) by the upcoming molten splat of the high melting component (zirconia) followed by mixing the two melts.

- An important finding in this work is that within the ranges of cooling rates in plasma spray process, the importance of the melting and mixing time (particle velocity for fixed spray distance) is more important than the variation in the splat cooling rate (splat flattening and/or thickness).
- For producing coatings with the more amorphous phase, using the two feed size ranges – several tens of micrometer size and nano-particulates (agglomerated in larger particles) – sprayed by APS process, the nano-size powder is more successful. However, between the nano-size powders and a few micron-size feeds, deposited by SPS process, the powder of a few micron size produces larger amounts of the amorphous phase. In addition, high spray robot speed is a significant parameter in maintaining the produced amorphous phase at high values.
- It was shown that, in plasma spray coatings, the supersaturated solid solution of zirconia with aluminium solute atoms (and/or alumina with zirconium atoms) is possible. This kind of solid solution is a new source of crystalline structure, not addressed before in the literature. Furthermore, dissolution of alumina in this crystalline phase is another reason for the absence of alumina in XRD patterns, in addition to mixing in the amorphous phase.
- In the SPS process formation of a variety of microstructures is possible. Different splat morphologies with large or small intersplat interfaces and from nearly zero

to more than 8% porosity are producible. These coatings can present various mechanical or thermal properties.

- It was revealed that, in the SPS process, the particle velocity is a major parameter controlling the microstructure, crystalline structure and amorphous phase formation of the coatings. Therefore, the as-sprayed structure of SPS coatings can be controlled using the process parameters that control the particle velocity. In addition, it was found that in the combined crystalline/amorphous coatings, during heating, the phases crystallize into structures dictated by the as-sprayed structure. Therefore, the particle velocity may indirectly affect the coating structure even after crystallization heat treatment.
- During dry deposition of the feed powder in APS, almost no fragmentation happens and the sizes of the initial and collected powders after spraying are similar. In contrast, in the SPS process, as a wet deposition method using the same powder feed, extensive liquid atomization and fragmentation result in much smaller in-flight particles and splats than with APS. The average size of the collected particles from SPS was found to be more than one order of magnitude smaller than that of APS, using the same powder feed.
- The material of interest (pseudo-eutectic alumina-YSZ) presents thermal cyclic resistance and thermal conductivity similar to 8 wt% YSZ. It also presents higher hardness and fracture toughness, but lower erosion resistance than 8 wt% YSZ.

As a general outcome of the studies on different phases within the coating, several scenarios can be suggested for the as-coated solid that can be traced within the composite structures. The splats may be solidified from the melt in either unmixed crystalline solid

(here alumina or zirconia) or solid solution (parented by either alumina or zirconia). This solid solution can form within the solubility limit or supersaturated, depending on the solidification condition. The as-deposited splat may also be in an amorphous (non-crystalline) state. In addition, the as-sprayed coating can contain unmolten crystalline solid, which may be heat-treated during flight in a plasma flame. The unmolten solid might have been initially pure or as-solid solution (from powder production processes). On the other hand, the partly molten particles could have re-solidified on the unmolten crystalline seeds and reproduced the crystalline structure of the feed.

7.2. Major Contributions

- An effective method for production of nano-crystalline structure in ceramic composite coatings has been introduced. The method is based on the amorphous phase and its crystallization in solid state, which results in smaller nano-crystalline grains than what is formed by rapid solidification during SPS coating. This nano-structure also shows more stability at high temperatures. Production of nano-structured coating using this method does not require nano-sized feed, because in the SPS process the amorphous phase forms more extensively when using powders of a few microns in size. Thus the method circumvents the difficulties in application of smaller feed sizes in production of nano-structured coating.
- A new multi-constituent structure was fabricated, composed of alumina hardened zirconia (AHZ) and zirconia toughened alumina (ZTA). This coating may benefit the characteristics of both structures (either AHZ or ZTH). This structure is produced by cyclic heating of the largely amorphous coatings. Heating cycles were in a range

between room temperature and 1000 ºC, which is slightly above crystallization temperature.

- This study made it possible to predict the microstructure and approximate crystalline structure of the suspension plasma spray coatings through parametric studies.
- Cyclic heat study was performed on the SPS coating for the first time in this work.

7.3. Recommendations for Future Works

The findings in this research provide the background for further studies on the SPS production method and resulting structures of the material under study, as well as investigations on new material for TBC application as follows.

- **Microstructural Repeatability in SPS Coatings**

In spite of the systematic effort taken in this work for control of the SPS coating microstructure (which resulted in production of many high-quality coatings), there is still a way to go for the best repeatability in this innovative process. When repeatability is obtained, different types of microstructure as found in this work can be reproduced, including porous or dense, with high or low vertical crack density, and also, smoothly flattened or corrugated splats. The resulting coatings may be considered for various applications, such as TBCs which require porous coatings, or solid oxide fuel cell electrolytes that need highly dense structure.

- **Further Investigation on AHZ-ZTA**

The newly produced multi-constituent structure of alumina hardened zirconia-zirconia toughened alumina (AHZ-ZTA) is expected to show interesting capabilities not only as a TBC but also in other industrial applications. Investigation of the properties and

surveillance of the applications of the special structure formed in this composite merit further work.

- **Further Investigation on Solid Solutions**

The properties and possible applications for the newly found supersaturated solid solutions of alumina and zirconia with high thermal stability are other considerable areas for further investigation. Knowledge of the properties and the ways of manipulating the amount of this phase, as was done here for the amorphous phase, may open the way to the improvement of the properties of the present composite or other composite coatings containing such a phase.

- **Other Compositions of Alumina-YSZ Composite**

The pseudo-eutectic alumina-zirconia coating showed poor erosion resistance as well as brittleness that seem to be mainly due to high alumina content. Hence, an initial survey was taken on an off-eutectic composition with a lower amount of alumina, as explained in Appendix I. According to this investigation using the SPS process, even the off-eutectic composition can yield as high an amorphous content as in the case of the eutectic composition using appropriate spray conditions. Therefore, to produce larger amounts of amorphous phase within the coating and to benefit from the advantages of this phase as reported in this thesis, lower amounts of alumina are applicable.

References

1. J.R. Davis & Associates, "Handbook of Thermal Spray Technology," Materials Park, OH, ASM International (2004).

2. U. Schulz, C. Leyens, K. Fritscher, M. Peters, B. Saruhan-Brings, O. Lavigne, J. Dorvaux, Some Recent Trends in Research and Technology of Advanced Thermal Barrier Coatings, *Aerospace Science and Technology* (2003/1) 7, *1*, pp73-80.

3. Kurt H. Stern, "Metallurgical and Ceramic Protective Coatings," London, UK, Chapman & Hall (1996).

4. D. C. Amory and R. A. Hovan, Improving Gas Turbine Operating Efficiency using Optical Pyrometry, www.landinst.com/combustion/downloads/pdf/Article_Optical_Pyrometry.pdf , as on June 2006

5. R.C. Garvie and M.V. Swain, Thermodynamics of the Tetragonal to Monoclinic Phase Transformation in Constrained Zirconia Microcrystals. Part 1. in the Absence of an Applied Stress Field. *Journal of Materials Science* (1985) 20, *4*, pp193-200.

6. R.C. Garvie, Thermodynamic Analysis of the Tetragonal to Monoclinic Transformation in a Constrained Zirconia Microcrystal. Part 2. in the Presence of an Applied Stress. *Journal of Materials Science* (1985) 20, *10*, pp3479-86.

7. M. Yashima, T. Nagatome, T. Noma, N. Ishizawa, Y. Suzuki and M. Yoshimura, Effect of Dopant Species on Tetragonal (t')-to-Monoclinic Phase Transformation of Arc-Melted ZrO2-RO1.5 (R = Sm, Y, Er, and Sc) in Water at 200° C and 100 MPa Pressure. *Journal of the American Ceramic Society* (1995) 78, *8,* pp2229-2232.

8. J.F. Bisson, C. Moreau, M. Dorfman, C. Dambra and J. Mallon, Behavior and Characterization of Two 7-8 Wt% Yttria-Stabilized Zirconia Powders and Coatings Produced using Plasma Spray Deposition, *Thermal Spray 2003: Advancing the Science and Applying the Technology, Proceedings of the International Thermal Spray Conference*, May 5-8, 2003, Orlando, FL, United States, pp1583-1589.

9. F.Tarasi, M. Medraj, A. Dolatabadi, J. Oberste-Berghaus, C. Moreau, Effective Parameters in Axial Injection Suspension Plasma Spray Process of Alumina-Zirconia Ceramics, *Journal of Thermal Spray Technology* (December, 2008) 17, *5-6,* pp685-691.

10. J.G. Murphy, H.W. King and P. Mayer, Erosion -Corrosion Resistant Coatings for Coal-Fired Boiler Tubes. II: Performance Tests of Thermal Expansion Matched Coatings, *Canadian Ceramics Quarterly* (1987) 56, *4,* pp21-25.

11. W. Pabst, G. Ticha, E. Gregrova, E. Tynova, Effective Elastic Properties of Alumina-Zirconia Composite Ceramics part5. Tensile Modulus of Alumina-Zirconia Composite Ceramics, *Ceramics-Silikaty* (2005) 49, *2,* pp77-85.

12. U. Brossmann, G. Knoener, H.-. Schaefer and R. Wuerschum, Oxygen Diffusion in Nanocrystalline ZrO_2., *Reviews on Advanced Materials Science* (2004) 6, *1,* pp7-11.

13. W.J. Quadakkers, V. Shemet, D. Sebold, R. Anton, E. Wessel and L. Singheiser, Oxidation Characteristics of a Platinized MCrAlY Bond Coat for TBC Systems during Cyclic Oxidation at 1000°C, *Surface and Coatings Technology* (2005) 199, *1*, pp77-82.

14. W.R. Chen, X. Wu, D. Dudzinski and P.C. Patnaik, Modification of Oxide Layer in Plasma-Sprayed Thermal Barrier Coatings, *Surface and Coatings Technology* (2006) 200, *20-21*, pp5863-5868.

15. K.S. Ravichandran, K. An, R. Taylor, Assessment of Thermal Barrier Coatings by Plasma Deposition, *Thermal Spray: A United Forum for Scientific and Technological Advances*, pp291-298.

16. W.Y. Lee, D.P. Stinton, C.C. Berndt, F. Erdogan, Y. Lee and Z. Mutasim, Concept of Functionally Graded Materials for Advanced Thermal Barrier Coating Applications, *Journal of the American Ceramic Society* (1996) 79, *12*, pp3003-3012.

17. C.G. Levi, Emerging Materials and Processes for Thermal Barrier Systems, *Current Opinion in Solid State and Materials Science* (2004) 8, *1*, pp77-91.

18. B. Leclercq, R. Mevrel, V. Liedtke and W. Hohenauer, Thermal Conductivity of Zirconia-Based Ceramics for Thermal Barrier Coating, *Materialwissenschaft Und Werkstofftechnik* (2003) 34, *4*, pp406-409.

19. M.A. Golozar, J. Mostaghimi, T.W. Coyle and R. Soltani, Wear Behavior of Nanostructured and Conventional Y-PSZ Coatings. *Materials Degradation: Innovation, Inspection, Control and Rehabilitation, Proceedings of the International Symposium on*

Materials Degradation: Innovation, Inspection, Control and Rehabilitation, Aug. 21-24, 2005, Calgary, AB, Canada, pp273-285.

20. H. Chen, X. Zhou, C. Ding, Investigation of the Thermomechanical Properties of a Plasma-Sprayed Nanostructured Zirconia Coating, *Journal of the European Ceramic Society* (August 2003) 23, *9*, pp1449-1455.

21. M. Suzuki, S. Sodeoka and T. Inoue, Alumina-Based Nanocomposite Coating Prepared by Plasma Spray, *Transactions of the Materials Research Society of Japan* (2004) 29, *2*, pp405-408.

22. M. Suzuki, T. Inoue and S. Sodeoka, Fabrication of Plasma Sprayed Al_2O_3/YAG Composite Coating and its Structure, *10th International Ceramics Congress*, 2002, Part C, (Faenza, Italy), pp381-388.

23. H.J. Kim, K.M. Lim, B.G. Seong and C.G. Park, Amorphous Phase Formation of Zr-Based Alloy Coating by HVOF Spraying Process. *Journal of Materials Science* (2001) 36, *1*, pp49-54.

24. H.-J. Kim and Y. J. Kim, Amorphous Phase Formation of the Pseudo-Binary Al_2O_3-ZrO_2 Alloy during Plasma Spray Processing. *Journal of Materials Science* (1999) 34, *1*, pp29-33.

25. G. Montavon, Recent Developments in Thermal Spraying for Improved Coating Characteristics and New applications/process Controls and Spray Processes, *High Temperature Material Processes* (2004) 8, *1*, pp45-93.

26. M. Gell, L. Xie, X. Ma, E.H. Jordan, N. P. Padture, Highly Durable Thermal Barrier Coatings made by the Solution Precursor Plasma Spray Process, *Surface and Coatings Technology* (2004) 177-178, pp97-102.

27. A.G. Evans, D.R. Mumm, J.W. Hutchinson, G.H. Meier and F.S. Pettit, Mechanisma Controlling the Durability of Thermal Barrier Coatings, *Progress in Materials Science* (2001) 46, pp505-553.

28. S. Deshpande, A. Kulkarni, S. Sampath and H. Herman, Application of Image Analysis for Characterization of Porosity in Thermal Spray Coatings and Correlation with Small Angle Neutron Scattering, *Surface and Coatings Technology* (2004) 187, *1*, pp6-16.

29. H. Xu, H. Guo, F. Liu and S. Gong, Development of Gradient Thermal Barrier Coatings and their Hot-Fatigue Behavior, *Surface and Coatings Technology* (2000) 130, *1*, pp133-139.

30. J. Fazilleau, C. Delbos, M. Violier, J-F. Coudert, P. Fauchais, L. Bianchi, K.Wittmann-Teneze, Influence of Substrate Temperature on Formation of Micrometric Splats obtained by Plasma Spraying Liquid Suspension. *Thermal Spray 2003-Advancing the Science & Applying the Technology,* C. Moreau and B. Marple, pp889-893.

31. B. Liang, H. Liao, C. Ding and C. Coddet, Nanostructured Zirconia–30 Vol.% Alumina Composite Coatings Deposited by Atmospheric Plasma Spraying, *Thin Solid Films* (2005) 484, *1-2*, pp225-231.

32. Y. Zeng, C. Ding and S. Lee, Plasma Sprayed Coatings using Different Nanosize Alumina Powders. *Thermal Spray 2003: Advancing the Science and Applying the Technology, Proceedings of the International Thermal Spray Conference*, May 2003, Orlando, FL, United States, pp671-674.

33. S. Sodeoka, M. Suzuki and T. Inoue, Thermal Stability and Mechanical Properties of Plasma Sprayed Al_2O_3/ZrO_2 Nano-Composite Coating, *Key Engineering Materials* (2006) 317-318, pp513-516.

34. A. J. Skoog, J. A. Murphy, and T. John, Method for Applying a Plasma Sprayed Coating using Liquid Injection. Patent# 20060222777

35. C. Monterrubio-Badillo, H. Ageorges, T. hartier, J.F. Codert and P. Fauchais, Plasma Spraying of a Perovskite Suspension for SOFC Cathodes, *Thermal Spray 2003: Advancing the Science & Applying the Technology*, pp687-692.

36. N.P. Padture, K.W. Schlichting, T. Bhatia, A. Ozturk, B. Cetegen, E.H. Jordan, M. Gell, Towards Durable Thermal Barrier Coatings with Novel Microstructures Deposited by Solution-Precursor Plasma Spray, *Acta Materialia* (2001) 49, *12*, pp2251-2257.

37. L. Xie, X. Ma, E.H. Jordan, N.P. Padture, D.T. Xiao and M. Gell, Deposition of Thermal Barrier Coatings using the Solution Precursor Plasma Spray Process, *Journal of Materials Science* (2004) 39, pp1639-1646.

38. L. Xie, X. Ma, E.H. Jordan, N.P. Padture, D.T. Xiao and M. Gell, Identification of Coating Deposition Mechanisms in the Solution-Precursor Plasma-Spray Process using

Model Spray Experiments, *Materials Science and Engineering A* (2003) 362, *1-2*, pp204-212.

39. X. Ma, F. Wu, J. Roth, M. Gell and E.H. Jordan, Low Thermal Conductivity Thermal Barrier Coating Deposited by the Solution Plasma Spray Process, *Surface and Coatings Technology* (2006) 201, *7*, pp4447-4452.

40. C. Delbos, J. Fazilleau, V. Rat, J.F. Coudert, P. Fauchais and B. Pateyron, Phenomena Involved in Suspension Plasma Spraying Part 2: Zirconia Particle Treatment and Coating Formation. *Plasma Chemistry and Plasma Processing*, pp393-414.

41. R. Siegert, J. Doering, J. Marques, R. Vassen, D. Sebold and D. Stoever, Denser Ceramic Coatings obtained by the Optimization of the Suspension Plasma Spraying Technique. *Thermal Spray 2004: Advances in Technology and Application, Proceedings of the International Thermal Spray Conference*, May 10-12, 2004, Osaka, Japan, pp568-573.

42. C. Delbos, J. Fazilleau, J.F. Coudert, P. Fauchais, L. Bianchi and K. Wittmann-Teneze, Plasma Spray Elaboration of Finely Structured YSZ Thin Coating by Liquid Suspension Injection., *Advancing the Science and Applying the Technology, Proceedings of the International Thermal Spray Conference*, May 2003, Orlando, FL, United States, pp661-669.

43. P. Fauchais, G. Montavon, M. Vardelle and J. Cedelle, Developments in Direct Current Plasma Spraying, *Surface and Coatings Technology* (2006) 201, *5*, pp1908-1921.

44. R.J. Damani and P. Makroczy, Heat Treatment Induced Phase and Microstructural Development in Bulk Plasma Sprayed Alumina, *Journal of the European Ceramic Society* (2000) 20, *7*, pp867-888.

45. P. Fauchais, Understanding Plasma Spraying, *Journal of Physics D: Applied Physics* (2004) 37, ppR86-R108.

46. E.H. Jordan, L. Xie, M. Gell, N. P. Padture, B. Cetegen, A. Uzturk, Superior Thermal Barrier Coatings using Suspension Plasma Spraying, *Journal of Thermal Spray Technology* (2004) 13, pp57-65.

47. K. Wittmann, F. Blein, J.F. Coudert, P. Fauchais, Control of the Injection of an Alumina Suspension Containing Nano-Grains in DC Plasma, *New Surfaces for a New Millennium,* K. A. K. C.C. Berndt E. F. Lugscheider, pp375-382.

48. P. Fauchais, V. Rat, C. Delbos, J.F. Coudert, T. Chartier and L. Bianchi, Understanding of Suspension DC Plasma Spraying of Finely Structured Coatings for SOFC, *IEEE Transactions on Plasma Science* (2005) 33, *2, Part 3*, pp920-930.

49. C. Delbos, C. Rat, C. Bonhomme, J. Fazilleau, J.F. Coudert and P. Fauchais, Influence of Powder Size Distributions on Microstructural Features of Finely Structured Plasma Sprayed Coatings, *High Temperature Material Processes* (2004) 8, pp397-406.

50. H. Zhang, H.B. Xiong, A. Vaydia, L. Li, Partially Melted Particle and its Splat Morphology, *Thermal Spray 2003: Advancing the Science and Applying the Technology,*

Proceedings of the International Thermal Spray Conference, 5-8 May, Orlando, FL, United States, pp905-911.

51. J.F. Bisson, B. Gauthier, C. Moreau, Effect of Direct-Current plasma Fluctuations on in-Flight Particle Parameters, *Journal of Thermal Spray Technology*, (2003) 12, *2*, pp258-264.

52. E. Bouyer, F. Gitzhofer, M.I. Boulos, Powder Processing by Suspension Plasma Spraying, *Thermal Spray- United Forum for Scientific and Technological Advances*, 1997, C. C. Berndt, Materials Park, Ohio, USA, pp353-359.

53. M. J. Stiger, N.M.Yanar, R. W. Jackson, C.G. Levi, Development of Intermixed Zones of Alumina/Zirconia in Thermal Barrier Coating Systems, *Metallurgical and Materials Transactions A* (2007) 38A, pp848-857.

54. T. Strangman, E.Raybould, Durable Thermal Barrier Coatings, Patent #.20060115660.

55. D.J. Green, R.H.J. Hannin, and M.V. Swain, Transformation Toughening of Ceramics, Boca Raton, Florida, USA,:CRC Press Inc. (1989).

56. E. Djurado, P. Bouvier and G. Lucazeau, Crystallite Size Effect on the Tetragonal-Monoclinic Transition of Undoped Nanocrystalline Zirconia Studied by XRD and Raman Spectrometry, *Journal of Solid State Chemistry* (2000) 149, *2*, pp399-407.

57. M. Andritschky, I. Cunha and P. Alpuim, Thermal Stability of Zirconia/Alumina Thin Coatings Produced by Magnetron Sputtering, *Surface and Coatings Technology* (1997) 94-95, *1-3*, pp144-148.

58. M. Yashima, M. Kakihana and M. Yoshimura, Metastable-Stable Phase Diagrams in the Zirconia-Containing Systems Utilized in Solid-Oxide Fuel Cell Application. *Solid State Ionics* (1996) pp1131-1149.

59. M. Yashima, S. Sasaki, M. Kakihana, Y. Yamaguchi, H. Arashi, M. Yoshimura, Oxygen-Induced Structural Change of the Tetragonal Phase Around the Tetragonal-Cubic Phase Boundary in ZrO_2-$YO_{1.5}$ Solid Solutions, *Acta Crystallographica Section B* (1994) 50, Part 6, pp663-672.

60. C.R. Aita, M.D. Wiggins, R. Whig, C.M. Scanlan and M. Gajdardziska-Josifovska, Thermodynamics of Tetragonal Zirconia Formation in a Nanolaminate Film, *Journal of Applied Physics* (1996) 79, pp1176.

61. A. Portinha, V. Teixeira, A. Monteiro, M.F. Costa, N. Lima, J. Martins and D. Martinez, Surface Analysis of Nanocomposite Ceramic Coatings, *Surface and Interface Analysis* (2003) 35, *9*, pp723-728.

62. K.W. Schlichting, N.P. Padture, E.H. Jordan and M. Gell, Failure Modes in Plasma-Sprayed Thermal Barrier Coatings, *Materials Science and Engineering A* (2003) 342, *1-2*, pp120-130.

63. R. Darolia and B. A. Nagaraj, Forming of Thermal-Barrier Coating Resistant to Deposits in Gas-Turbine Service., Patent #.EP 1 335 040 A2.

64. C. Mercer, S. Faulhaber, A.G. Evans and R. Darolia, A Delamination Mechanism for Thermal Barrier Coatings Subject to Calcium–Magnesium–Alumino-Silicate (CMAS) Infiltration, *Acta Materialia* (2005) 53, *4*, pp1029-1039.

65. L. Xie, D. Chen, E.H. Jordan, A. Ozturk, F. Wu, X. Ma, B.M. Cetegen, Formation of Vertical Cracks in Solution-Precursor Plasma-Sprayed Thermal Barrier Coatings, *Surface and Coatings Technology* (2006) 201, *3-4*, pp1058-1064.

66. X. Bi, H. Xu, S. Gong, Investigation of the Failure Mechanism of Thermal Barrier Coatings Prepared by Electron Beam Physical Vapor Deposition, *Surface and Coatings Technology* (2000) 130, pp122-127.

67. P. Ramaswamy, S. Seetharamu, K.B.R. Varma and K.J. Rao, Al_2O_3-ZrO_2 Composite Coatings for Thermal-Barrier Applications, *Composites Science and Technology* (1997) 57, *1*, pp81-89.

68. K.S. Ravichandran, K. An, R.E. Dutton and S.L. Semiatin, Thermal Conductivity of Plasma-Sprayed Monolithic and Multilayer Coatings of Alumina and Yttria-Stabilized Zirconia, *American Ceramic Society* (1999) 82, *3*, pp673-682.

69. S. Widjaja, A.M. Limarga and T.H. Yip, Modeling of Residual Stresses in a Plasma-Sprayed zirconia/alumina Functionally Graded-Thermal Barrier Coating, *Thin Solid Films* (2003) 434, *1-2*, pp216-227.

70. A.M. Limarga, S. Widjaja and T.H. Yip, Mechanical Properties and Oxidation Resistance of Plasma-Sprayed Multilayered Al_2O_3/ZrO_2 Thermal Barrier Coatings, *Surface and Coatings Technology* (2005) 197, *1*, pp93-102.

71. A. Portinha, V. Teixeira, J. Carneiro, S.N. Dub and R. Shmegera, Mechanical Properties of ZrO_2-Al_2O_3 Nanostructured PVD Coatings Evaluated by Nanoindentation., *Reviews on Advanced Materials Science* (2003) 5, *4*, pp311-318.

72. A.L. Vasiliev and N.P. Padture, Coatings of Metastable Ceramics Deposited by Solution-Precursor Plasma Spray: II. Ternary ZrO_2–Y_2O_3–Al_2O_3 System, *Acta Materialia* (2006) 54, *18*, pp4921-4928.

73. A.L. Vasiliev, N.P. Padture and X. Ma, Coatings of Metastable Ceramics Deposited by Solution-Precursor Plasma Spray: I. Binary ZrO_2–Al_2O_3 System, *Acta Materialia* (2006) 54, *18*, pp4913-4920.

74. M. Kurumada, C. Koike, C. Kaito, Laboratory Production of δ and θ alumina Grains and their Characteristic Infrared Spectra, *Monthly Notices of the Royal Astronomical Society* (2005) 359, *2*, pp643-648.

75. A. Vardelle, C. Robert, G.X. Wang, S. Sampath, Analysis of Nucleation, Phase Selection and Rapid Solidification of an Alumina Splat, *Thermal Spray: A United Forum for Science and Technological Advances*, 1997, C.C. Berndt, pp635-643.

76. I. Levin, D. Brandon, Metastable Alumina Polymorphs: Crystal Structures and Transition Sequences, *Journal of the American Ceramic Society* (1998) 81, *8,* pp1995-2012.

77. M.I.F. Macedo, C.A. Bertran, C.C. Osawa, Kitetics of the γ to α-Alumina Phase Transformation by Quantitative X-Ray Diffraction, *Journal of Materials Science* (2007) 42, pp2830-2836.

78. Zun Chen, R.W. Trice, M. Besser, Xiaoyun Yang and D. Sordelet, Air-Plasma Spraying Colloidal Solutions of Nano-Sized Ceramic Powders, *Journal of Materials Science* (2004) 39, *1,* pp4171-4178.

79. X. Zhao, Y. An, J. Chen, H. Zhou and B. Yin, Properties of Al_2O_3–40 Wt.% ZrO_2 Composite Coatings from Ultra-Fine Feedstocks by Atmospheric Plasma Spraying, *Wear* (2008) 265, *11-12,* pp1642-1648.

80. S. Dosta, I.G. Cano, J.R. Miguel, and J.M. Guilemany, Production and Characterization of Metastable ZrO_2-Al_2O_3 Coatings obtained by APS+Quench, *Journal of Thermal Spray Technology* (2008) 17, *3,* pp360-364.

81. J. Obeste Berghaus, J.G. Legoux, C. Moreau, F. Tarasi and T. Chraska, Mechanical and Thermal Transport Properties of Suspension Thermal Sprayed Alumina-Zirconia Composite Coatings, *Journal of Thermal Spray Technology* (2008) 17, *1,* pp91-104.

82. T. Chraska, K. Neufussa, J. Dubskya, P. Ctibora, P. Rohan, Fabrication of Bulk Nanocrystalline Alumina-Zirconia Materials, *Ceramics International* (2008) 34, *5*, pp1229-1236.

83. P. Fauchais, M. Vardelle, A.Vardelle, L. Bianchi, A.C. Leger, Parameters Controlling the Generation and Properties of Plasma Spray Zirconia Coatings, *Plasma Chemistry and Plasma Processing* (1996) 16, *1*, pp99S-125S.

84. L. Xie, E.H. Jordan, N.P. Padture and M. Gell, Phase and Microstructural Stability of Solution Precursor Plasma Sprayed Thermal Barrier Coatings, *Materials Science and Engineering A* (2004) 381, *1-2*, pp189-195.

85. G. Shanmugavelayutham, S. Yano and A. Kobayashi, Microstructural Characterization and Properties of ZrO_2/Al_2O_3 Thermal Barrier Coatings by Gas Tunnel-Type Plasma Spraying, *Vacuum* (2006/9/7) 80, *11-12*, pp1336-1340.

86. A. Nazeri and S.B. Qadri, Alumina-Stabilized Zirconia Coatings for High-Temperature Protection of Turbine Blades, *Surface and Coatings Technology* (1996) 1-3, pp166-169.

87. B.L. Kirsch, A.E. Riley, A.F. Gross and S.H. Tolbert, Probing the Effects of Interfacial Chemistry on the Kinetics of Phase Transitions in Amorphous and Tetragonal Zirconia Nanocrystals, *Langmuir* (2004) 20, *25*, pp11247-11254.

88. C. Moreau, J. F. Bisson, R. S. Lima, B. R. Marple, Diagnostics for Advanced Materials Processing by Plasma Spraying, *Pure and Applied Chemistry* (2005) 77, *2,* pp443-462.

89. F.W. Gartner, Thermal Spray, Flame Spray, Metallization and Hard Facing, Product and Services, QA/QC Accuraspray, http://www.fwgts.com/fwgts_prodserv_qa_accura.htm as on May 2006.

90. J.M.S. F. Tang, Evolution of Young's Modulus of Air Plasma Sprayed Yttria-Stabilized Zirconia in Thermally Cycled Thermal Barrier Coatings, *Scripta Materialia* (2006) 54, pp1587-1592.

91. O.Kovarik, J. Nohava, P. Chraska, Young's Modulus and Fatigue Behavior of Plasma-Sprayed Alumina Coatings, *Journal of Thermal Spray Technology* (2005) 14, *2,* pp31-238.

92. ASTM Designition: G76-83 (Reapproved on March 1989) "*Standard Practice for Conducting Erosion Tests by Solid Particle Impingement using Gas Jets."*

93. A.S. Houlbert, P. Cielo, C. Moreau and M. Lamontagne, Measurement of Thermal Diffusivity and Anisotropy of Plasma-Sprayed Coatings. *International Journal of Thermophysics* (1994) 15, *3,* pp525-546.

94. A. Lopez-Rubio, B. M. Flangan, E. P. Gilbert, M. J. Gidley, A Novel Approach for Calculating Starch Crystallinity and its Correlation with Double Helix Content: A Combined XRD and NMR Study, *Biopolymers* (2008) 89 #9, *9,* pp761-768.

95. Thermo-Scientific Co., Thermo-Galactic software package, GRAMS/AI Software; (2002) Version 7.01.

96. P. Keblinski, S.R. Phillpot, D. Wolf and H. Gleiter, Relationship between Nanocrystalline and Amorphous Microstructures by Molecular Dynamics Simulation, *Nanostructured Materials* (1997) 9, *1-8*, pp651-660.

97. A. Gombas, P. Szabo-Revesz, M.Kata, G. Regdon Jr., I. Eros, Quantitave Determination of Crystallinity of α-Lactose Monohydrate, *Journal of Thermal Analysis and Calorimetry* (2002) 68, pp503-510.

98. Cullity, B.D, Structure of Polycrystalline Aggregates. In *Elements of X-Ray Diffraction*. USA, California:Addison-Wesley Publishing Company Inc. (1978).

99. G.N. Werner Kraus, Powdercell Software for Windows (2000) version 2.4.

100. P. Villars, L.D.C. *Pearson's Handbook of Crystallographic Data*, Materials Park, OH, ASM International (1991).

101. Y.S. T. Ando, Meta-Stable Alumina Structures in Melt-extractedAlumina-25wt% Zirconia and Alumina-42wt% Zirconia Ceramics, *Journal of the American Ceramic Society* (1991) 74, pp410-417.

102. M.Y. J.M. Calderon-Moreno, Stabilization of Zirconia Lamella in Rapidly Solidified Alumina-Zirconia Eutectic Composites, *Journal of the European Ceramic Society* (2005) 25, pp1369-1372.

103. Charls E. Mortimer. *Chemistry*, Belmont, CA, USA: Wadsworth Pub Co (1986).

104. C. Bartuli, L.Bertamini, S. Matera, S. Sturlese, Investigation of the Formation of an Amorphous Film at the ZrO_2-Y_2O_3/NiCoCrAlY Interface of Thermal Barrier Coatings Produecd by Plasma Spraying, *Materials Science and Engineering A* (1995) 199, pp229-237.

105. K.A.H. Chraska T., Transmission Electron Microscopy Study of Rapid Solidification of Plasma Sprayed Zirconia-Part II. Interfaces and Subsequent Splat Solidification, *Thin Solid Films* (2001) 397, pp40-48.

106. O. Yamaguchi, M. Shirai, M. Yoshinaka, Formation and Transformation of Cubic ZrO_2 Solid Solution in the System ZrO_2-Al_2O_3, *Communications of the American Ceramic Society* (1988) 71, *12,* ppC510-C512.

107. G. Box, W. Hunter and J. Hunter. *Statistics for Experimenters an Introduction to Design, Data Analysis, and Model Buildings*. Canada: John Willey & Sons Inc. (1978).

108. C.-. Li and A. Ohmori, Relationship between the Microstructure and Properties of Thermally Sprayed Deposits, *Journal of Thermal Spray Technology* (2002) 11, *3,* pp365-374.

109. F. Cernuschi, P. Bianchi, M. Leoni and P. Scardi, Reviewed Papers - Thermal Diffusivity/Microstructure Relationship in Y-PSZ Thermal Barrier Coatings, *Journal of Thermal Spray Technology* (1999) 8, *1*, pp102-109.

110. R. Vassen, F. Traeger and D. Stover, Correlation between Spraying Conditions and Microcrack Density and their Influence on Thermal Cycling Life of Thermal Barrier Coatings, *Jornal of Thermal Spray Technology* (2004) 13, *3,* pp396-404.

111. R. Soltani, T.W. Coyle, J. Mostaghimi, R.S. Lima and C. Moreau, Thermo-Physical Properties of Plasma Sprayed Yttria Stabilized Zirconia Coatings, *Surface and Coatings Technology* (2008) 202, *16,* pp3954-3959.

112. H.Zhang, X.Y.Wang, L.L.Zheng, S.Sampath, Numerical Simulation of Nucleation, Solidification, and Microstructure Formation in Thermal Spraying, *International Journal of Heat and Mass Transfer* (2004) 47, pp2191-2203.

113. A. Haddadi, F. Nardou, P. Fauchais, A. Grinaud and A.C. Leger, Influence of Substrate and Coating Temperature on Columnar Growth within Plasma Sprayed Zirconia and Alumina Coatings, *United Forum for Scientific and Technological Advances,* C. C. Berndt, pp671-680.

114. J. Oberste Berghaus, S. Bouaricha, J.-G. Legoux, C. Moreau, Injection Conditions and in-Flight Particle States in Suspension Plasma Spraying of Alumina and Zirconia Nano-Ceramics, *Proceedings of the 2005 International Thermal Spray Conference, Thermal Spray: Building on 100 Years of Success*, May 2-5, 2005, Basel, Switzerland, pp512-518.

115. J.W. Christian. The Theory of Transformations in Metals and Alloys. Oxford, UK: Pergamon, Elsevier Science Ltd. (2002).

116. X.-L. Wu, Q. Ren, X.-M. He, Preparation of Nanoscale High-Purity α-Alumina Powders, *Key Engineering Materials* (2007) 336-338, pp2051-2053.

117. J.K.s. J. Ilavsky, J. Wallace, Thermal Spray Yittria-Stabilized Zirconia Phase Changes During Annealing, *Journal of Thermal Spray Technology* (2001) 10, *3*, pp497-501.

118. F. Tarasi, M. Medraj, A. Dolatabadi, J. Oberste-Berghaus, C. Moreau, Phase Formation and Transformation 60/40 alumina/YSZ Nano Composite Coatings Deposited by Suspension Plasma Spray, *Journal of Materials Science A* (2009 (in press)).

119. M. Suzuki, S. Sodeoka, T. Inoue, Study of Alumina-Based Nano Composite Coating Prepared by Plasma Spray, *Thermal Spray 2003: Advancing the Science and Applying the Technology* (2003), B. M. C. Moreau, pp701-705.

120. C. Robert, A. Denoirjean, A. Vardelle, G.-X. Wang, S. Sampath, Nucleation and Phase Selection in Plasma Sprayed Alumina: Modeling and Experiment, 25-29 May, Niece, France, pp407-412.

121. V. Jayarama, C.G. Levia, T. Whitneya, R. Mehrabiana, Characterization of Al_2O_3-ZrO_2 Powders Produced by Electrohydrodynamic Atomization, *Materials Science and Engineering: A* (1990) 124, *1*, pp65-81.

122. D. Chen, E. H. Jordan, M. Gella, Solution Precursor High-Velocity Oxy-Fuel Spray Ceramic Coatings, *Journal of the European Ceramic Society* (2009) 29, *16*, pp3349-3353.

123. R. S. Lima, B. R. Marple, Toward Highly Sintering-Resistant Nanostructured ZrO_2-7wt.%Y_2O_3 Coatings for TBC Applications by Employing Differential Sintering, *Journal of Thermal Spray Technology* (2008) 17, *5-6,* pp846-852.

124. H.C. Chen, E. Pfender, B. Dzur, G. Nutsch, Microstructural Characterization of Radio Frequency and Direct Current Plasma-Sprayed Al_2O_3 Coatings, *Journal of Thermal Spray Technology* (June 2000) 9, *2,* pp264-273.

125. A. Guinier. X-Ray Crystallographic Technology, London, Hilger & Watts LTD. (1952).

126. R. Dutton, R. Wheeler, K. S. Ravichandran, K. An, Effect Of Heat Treatment on Thermal Conductivity of Plasma-Sprayed Thermal Barrier Coatings, *Journal of Thermal Spray Technology* (2000) 9, *2,* pp204-209.

127. A.G. Evans, N.A. Fleck, S. Faulhaber, N. Vermaak, M. Maloney, R. Darolia, Scaling Laws Governing the Erosion and Impact Resistance of Thermal Barrier Coatings, *Wear* (2006) 260, pp886-894.

128. J. Ilavsky, G.G. Long, A.J. Allen, Evolution of the Plasma-Sprayed Deposits during Heating, *15th International Thermal Spray Conference,* 25-29 May 1998, Nice, France, pp1641-1644.

129. S. Rao-Bala, D. Tromans, Effect of Overaging on Mechanical Properties and Stress Corrosion Cracking of HY-180M Steel, *Metallurgical and Materials Transactions A* (1980) 11, *7,* pp1187-1196.

130. C-J Li, W-Z Wang, Y. He, Dependency of Fracture Toughness of Plasma Sprayed Al_2O_3 coatings on Lamellar Structure, *Journal of Thermal Spray Technology* (2004) 13, *3*, pp425-431.

131. J.P. Holman. Thermal Conductivity, in *Heat Transfer*. Boston, USA: McGraw Hill (2002).

132. R. K. Williams, J. B. Bates, R. S. Graves, D. L. McElroy, F. J. Weaver, Comparison of Thermal Conductivity Data for Partially Stabilized Zirconia with Values Derived from Thermal Diffusivity Results, *International Journal of Therrnophysics* (1988) 9, *4*, pp588-598.

Appendix

This work was done to investigate the capability of other compositions of the alumina-YSZ composites, with lower alumina content than eutectic (hypo-eutectic composition), to produce large amounts of amorphous contents using SPS coating. For this, the 57.5/42.5 wt% alumina/YSZ and an off-eutectic composition with 35/65 wt% of alumina/YSZ were sprayed under three different spray conditions as per Table A-**7-1**.

Table A-7-1 SPS spray conditions for the two compositions of alumina-YSZ composite

Condition #	Nozzle size	Current (A)	Gas Flow (slm)	Plasma gas composition ($Ar/N_2/H_2$) (slm)	Feed rate (kg/hr)	T_p±50 (°C)	V_p±20 (m/s)
1	7/16”(11 mm)	180	180	45/45/10	1.6	2850	436
2	3/8”(9.5 mm)	180	180	45/45/10	1.6	2900	570
3	3/8”(9.5 mm)	200	245	75/10/15	1.1	2720	690

The crystallinity index (defined as CI%= 1‒amorphous%) was determined and the results are illustrated in Figure A-1. This figure shows that in all three spray conditions, both the pseudo-eutectic (57.5 wt% alumina-YSZ) and the hypo-eutectic (35 wt% alumina-YSZ) compositions present a comparable crystallinity index. This means that under the same spray conditions, various compositions can produce almost similar amorphous content.

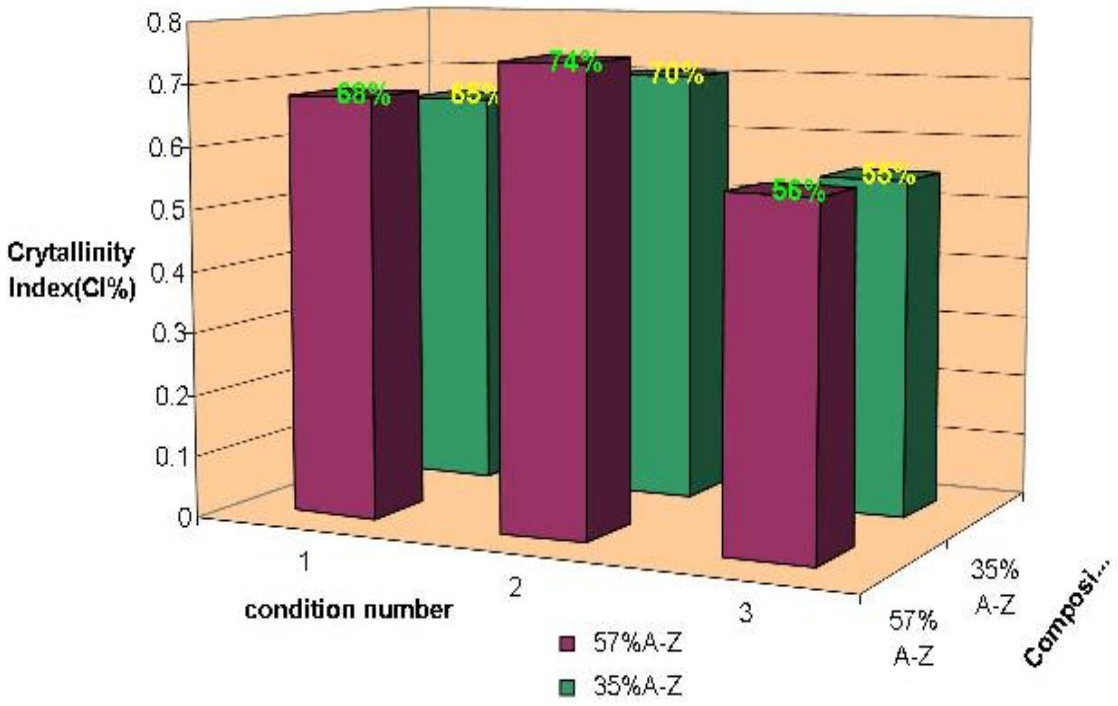

Figure A-1 Crystallinity index as a function of either spray condition or composition in alumina-zirconia composite coating

On the other hand, the spray condition has changed the CI% from about 68% when coating is generated with condition 1, up to about 74% using condition 2; 56% amorphous resulting from condition 3. It can be seen that the three spray conditions show evidently more differences in the crystallinity index than in composition. This means that for high amorphous coatings other compositions with lower alumina content can also be used and the amorphous phase can be increased by suitable choice of spray parameters.